Dissertation

On

FINITE ELEMENT APPROACH FOR SIMULATION OF POWDER MIXED ELECTRIC DISCHARGE MACHINING (PMEDM) PROCESS AND EXPERIMENTAL VALIDATION

Submitted in partial fulfillment of the requirement for

the award of degree of

MASTER OF ENGINEERING

IN

CAD/CAM & ROBOTICS

Submitted By

KULWINDER SINGH

Roll No. 800981015

Under the Guidance of

ANIRBAN BHATTACHARYA
Assistant Professor,
Department of Mechanical Engineering,
Thapar University,
Patiala - 147004

SANDEEP K. SHARMA
Assistant Professor,
Department of Mechanical Engineering,
Thapar University,
Patiala - 147004

DEPARTMENT OF MECHANICAL ENGINEERING

THAPAR UNIVERSITY

PATIALA-147004, INDIA

This Thesis is dedicated to my parents and my teachers Anirban Bhattacharya and Sandeep K. Sharma

ACKNOWLEDGEMENT

Words are often less to revels one's deep regards. With an understanding that work like this can never be the outcome of a single person, I take this opportunity to express my profound sense of gratitude and respect to all those who directly or indirectly helped me through the duration of this work.

I take the opportunity to express my heartfelt adulation and gratitude to my supervisors, ***Anirban Bhattacharya*** *and* ***Sandeep K. Sharma*** *for their unreserved guidance, constructive suggestions, thought provoking discussions and unabashed inspiration in the nurturing work. It has been a benediction for me to spend many opportune moments under the guidance of the perfectionist at the acme of professionalism. The present work is testimony to their activity, inspiration and ardent personal interest, taken by them during the course of this work in its present form. I am grateful to* ***Dr. Ajay Batish****, Prof. & Head, MED for providing the facilities for the completion of the work.*

The non teaching staff Mr. Sukhbir Singh, Mr. Narender Kumar, Mr. Pardeep Kumar, Mr. Kuldeep, Mr. Lalit Kumar, Mr. Sohan Lal deserves special thanks for their help during the period of this work. No words acknowledge the support I received from my friends for their valorous help and co-operation.

I take pride of myself being son of ideal parents for their everlasting desire, sacrifice, affectionate blessings, and help, without which it would not have been possible for me to complete my studies.

I would like to thank to all the members and employees of Mechanical Engineering Department, Thapar University Patiala for their everlasting support. Above all, I express my indebtedness to the "ALMIGHTY" for all His blessing and kindness.

Kulwinder Singh

Registration No.: 800981015

DECLARATION

I hereby declare that the thesis entitled **"FINITE ELEMENT APPROACH FOR SIMULATION OF POWDER MIXED ELECTRIC DISCHARGE MACHINING (PMEDM) PROCESS AND EXPERIMENTAL VALIDATION"** is an authentic record of my study carried out as requirement for the award of degree of **Master of Engineering (CAD/CAM & Robotics)** at **Thapar University, Patiala** under the guidance of **ANIRBAN BHATTACHARYA**, Assistant Professor and **SANDEEP K. SHARMA**, Assistant Professor, Department of Mechanical Engineering, Thapar University, Patiala during **July 2010 to June 2011.** The matter embodied in this report has not been submitted in part or full to any other university or institute for the award of any other degree.

Kulwinder

(Kulwinder Singh)
Reg. No. 800981015

This is to certify that above declaration made by the student concerned is correct to the best of my knowledge and belief.

Anirban Bhattacharya

(ANIRBAN BHATTACHARYA)
Assistant Professor,
Department of Mechanical Engineering,
Thapar University,
Patiala - 147004

(SANDEEP K. SHARMA)
Assistant Professor,
Department of Mechanical Engineering,
Thapar University,
Patiala - 147004

Countersigned by:

Dr. AJAY BATISH
Professor and Head,
Department of Mechanical Engineering,
Thapar University,
Patiala -147004

Dr. S.K. MOHAPATRA
Dean of Academic Affairs,
Thapar University,
Patiala -147004

ABSTRACT

Electrical Discharge Machining (EDM) is one of the most extensively used non-traditional material removal process capable of machining tough, high strength, corrosion resistant electrically conductive materials. Mixing of suitable material in powder form into the dielectric fluid is a recent advancement in EDM process to improve its process capabilities and is known as powder mixed EDM (PMEDM) process. Present work aimed at studying the thermal aspects of Powder Mixed EDM process using ANSYS Workbench 12.0 (Transient Thermal Analysis module and Static Structural Analysis module) to simulate temperature distribution, volume removed, cooling rate and stresses developed into the workpiece. Study is related to temperature distribution due to a single spark for one cycle varying different process parameters employing the Gaussian type of heat distribution inside the spark channel. Temperature distribution simulated using Transient Thermal analysis module is used to estimate volume removed and temperature variation in radial and depth direction using a code developed with Visual C++ 6.0. Development of different temperature zones (unaffected, heat affected, melting and evaporating zone), shape and size of the craters have been studied. Temperature distribution during simulation is found to be maximum at centre of spark region and decrease in radial direction following Gaussian distribution. Cooling rate of the workpiece material have been estimated using different discharge current, fraction of heat incident, pulse on and pulse off duration for a one complete cycle. Coupled Thermal-Structural analysis has been done to find stresses that develop into work material during PMEDM process. For validation experiments have been conducted on the H11 (hot die steel) workpiece using different set of process parameters. Experimental validation confirmed that 20 to 25% heat is transferring to the workpiece as predicted volume using C_w ranging from 0.2 to 0.25 during simulation is found to match with experimental volume removed for different pulse on and discharge current settings. Observing microstructure cracks appearing on the machined surface validates higher cooling rate and equivalent stresses predicted during simulation. Detailed study of the craters using microscope was completed to confirm the shapes and sizes of the craters that formed during the experimentation.

LIST OF FIGURES

LIST OF TABLES

ABBREVIATIONS

AHP	Analytic hierarchy process
ANOVA	Analysis of variance
C	Carbon
CLSM	Confocal laser scanning microscopy
CNC	Computer numerical control
Co	Cobalt
Cr	Chromium
CTE	Coefficient of thermal expansion
Cu	Copper
C_w	Fraction of total supplied heat going into workpiece
DC	Direct current
EDA	Electro-discharge alloying
EDM	Electric discharge machining
FE	Finite element
Fe	Iron
FEM	Finite element method
h	Coefficient of convection heat transfer
HSFC	High speed framing camera
HSS	High Speed Steel
I_d	Discharge current
K	Thermal conductivity
K_n	Powder particle size and concentration factor
Mn	Manganese
Mo	Molybdenum
MRR	Material removal rate
Ni	Nickel
OOP	Object oriented programming
P	Phosphorous
PFE	Plasma flushing efficiency
PMEDM	Powder mixed electric discharge machining
R	Spark radius
R_a	Surface roughness

RC	Resistance capacitance
S	Sulphur
SEM	Scanning electron microscopy
Si	Silicon
SP	Scanning profile-meter
SR	Surface roughness
T_0	Ambient temperature
T_B	Boiling temperature
Ti	Titanium
T_m	Melting temperature
T_{off}	Pulse off time
T_{on}	Pulse on time
T_{RC}	Recystalization temperature
T_U	Unaffected zone temperature
TWR	Tool wear rate
V	Vanadium
V_d	Discharge voltage
V_g	Gap voltage
XRD	X-Ray diffraction
I	Current
R	Spark radius
T	Temperature
U	Electric potential
V	Voltage
a	Crater radius
n	Number of load step
$q(r)$	Heat flux incident at radius r
$q(t)$	Equivalent heat input at time t
r	Distance along spark radius
t	Time
t	Time
σ	Standard deviation
h_c	Crater depth

C_{ev}	Specific heat for evaporation
C_m	Specific heat for melting
F_c	Fraction of total EDM spark going into cathode
I_n	Discharge current
K_p	Powder particle and size concentration factor
L_{ev}	Latent heat of evaporation
L_m	Latent heat of melting
$Q_w(r)$	Heat flux incident at radius r
R_{max}	Maximum surface roughness
R_n	Heat source radius
R_{pc}	Spark radius
R_w	Fraction of total supplied heat transferred to workpiece
S_0	Section of initial plasma channel
T_{ev}	Evaporation temperature
T_m	Melting temperature
V_b	Breakdown voltage
V_c	Crater Volume
V_n	Discharge voltage
q_0	Maximum heat incident at spark centre
q_n	Heat Flux
t_d	Discharge duration
t_{on}	Pulse on time
ΔT	Change in temperature

CONTENTS

CHAPTER 1
INTRODUCTION

1.1 INTRODUCTION TO NON-TRADITIONAL MANUFACTURING PROCESSES

Industries in the field of aeronautics, nuclear reactors, automobiles, missiles, turbines etc. work with the materials like high strength temperature resistant alloys which have higher strength, corrosion resistance, toughness, and other diverse properties. With rapid development in the field of materials it has become essential to develop cutting tool materials and processes which can safely and conveniently machine such new materials. Besides this industries face problems in manufacturing of components because of several reasons such as the complexity of the job profile or may be due to surface requirements with higher accuracy and surface finish. Consequently, non-traditional techniques of machining are providing effective solutions for the problem raised by the increasing demand for high strength temperature resistant alloys, parts with intricate and compacted shapes and materials so hard which are difficult to machine by conventional methods. The processes are non-conventional in the sense as no conventional tool is employed for the material removal. Non conventional or advance machining processes can be classified into three basic categories, i.e. mechanical, thermoelectric, and electrochemical machining processes. Some of them can be used only for electrically conductive materials while others can be used for both electrically conductive and electrically non-conductive materials. The range of applications of newly developed machining process is determined by work piece properties like electrical and thermal conductivity, melting temperature, electrochemical equivalent etc. In mechanical advanced machining methods, (abrasive jet machining, ultrasonic machining, and water jet machining) kinetic energy of either abrasive particles or water jet is utilized to remove material from the work piece. In electro-thermal method (plasma arc machining, laser beam machining, and electron beam machining) the energy is supplied in form of heat, light, and electron bombardment which results melting, or vaporization and melting both of work material. . In electrochemical & chemical methods (electrochemical machining, chemical machining), is an etching process which has very narrow range of applications mainly because of very low MRR and difficult in finding a suitable etchant for given work material. The selection of a

process is depend upon various factors like- process capabilities, physical parameters, shape to be machined, properties of work piece material to be cut, and economics of process. As there is no direct contact between the tool and the work piece in the non conventional machining; hence the tool need not be harder than the job. Today after the huge technical advancements, the conventional machining processes can't produce complex geometrical shapes in the hard and temperature resistant alloys and die steels effectively. So for these requirements, a number of non-conventional methods have been developed.

1.2 ELECTRIC DISCHARGE MACHINING

Electrical discharge machining (EDM) is one of the most extensively used non-conventional material removal processes. In EDM there is no contact between tool (electrode) and part. During process, a series of discrete electrical discharges occur between electrode and work piece in a dielectric medium. During the application of each discharge, local temperature rises at several thousand degrees. As a consequence, part material melts and vaporizes generating craters on the surface of the work piece, and it is removed in the form of debris by dielectric flushing [1]. Its unique feature of using thermal energy to machine electrically conductive parts regardless of hardness has been its distinctive advantage. The electrical discharge machining process is widely used in the aerospace, automobile, die manufacturing and moulds industries to machine hard metals and its alloy.

1.3 HISTORY OF ELECTRIC DISCHARGE MACHINING

In dates back to 1770, English chemist Joseph Priestly discovered the erosive effect of electrical discharges on metal. More than hundred years were elapse before some practical use made of effect. In 1943 at the Moscow University B.R. and N.I. Lazarenko, while investigating the wear of switch contacts, found that spark discharge could be used to machine high strength materials which were difficult to machine by established methods [2]. They developed a controlled process of machining to machine metals by vaporizing material from the surface of work piece. The first British patent was granted to Rudorff in 1950. USA, Japan and Switzerland developed their machining around 1950. In 1950s The RC (resistance–capacitance) relaxation circuit was introduced, in which first consistent dependable control of pulse times and a simple servo control circuit to automatically find and hold a given gap between the electrode (tool) and the work piece was developed. A

machine for spark machining by 'method x' was patented in USA in 1952. After the investigation of Lazarenko, the EDM process has attracted worldwide attention as a technique for metal machining [3]. In the 1980s, CNC EDM was introduced which improved the efficiency of the machining operation.

1.4 WORKING PRINCIPLE OF EDM

The basic principle in EDM is the conversion of electrical energy into thermal energy through a series of electrical discharges occurring between the electrode and work piece. Workpiece and electrode are immersed in the dielectric fluid, which gives the insulating effect to avoid the electrolysis of electrode while in process. There is a small gap between the electrode and the workpiece. A spark is produced at the point of smallest inter-electrode gap by a high voltage, overcoming the dielectric strength. Dielectric breakdown and temperature attained in range of 8000 to 12,000 °C. Due to elevated temperature erosion of metal from both electrodes takes place. Duration of each spark is very short and the entire cycle time is usually of few micro-seconds (μs).The frequency of pulsating direct current supply is about 20,000–30,000 Hz. A sudden reduction in the temperature occurs after turning off the DC supply and the circulating dielectric fluid flush the molten material from the workpiece in the form of microscopic debris. After each discharge, the capacitor is recharged from DC source through a resistor, and another spark is generated at next narrowest gap (Figure 1.1). Due to the succession of sparks spread over the entire work piece surface erosion take place and the shape generated is inverse of the electrode or tool.

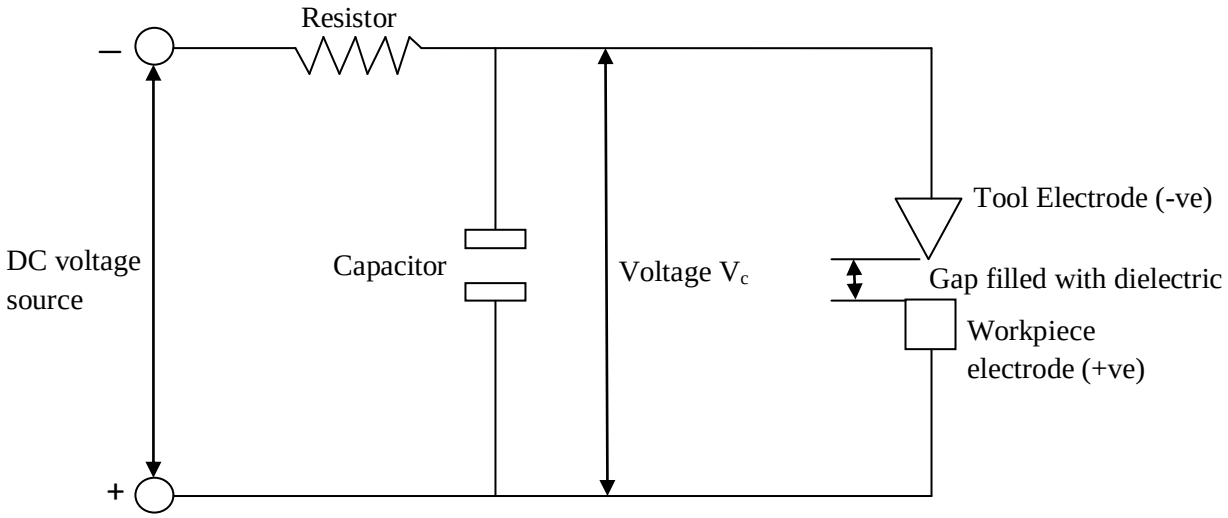

Fig 1.1 Relaxation circuit [2]

A servo system, which compares the gap voltage with a reference value, is employed to ensure that the electrode moves at a proper rate to maintain the right spark gap, and to retract the electrode if short-circuiting occurs. For supplying the intermittent supply pulse generator is used. A typical wave form is shown in Figure 1.2.

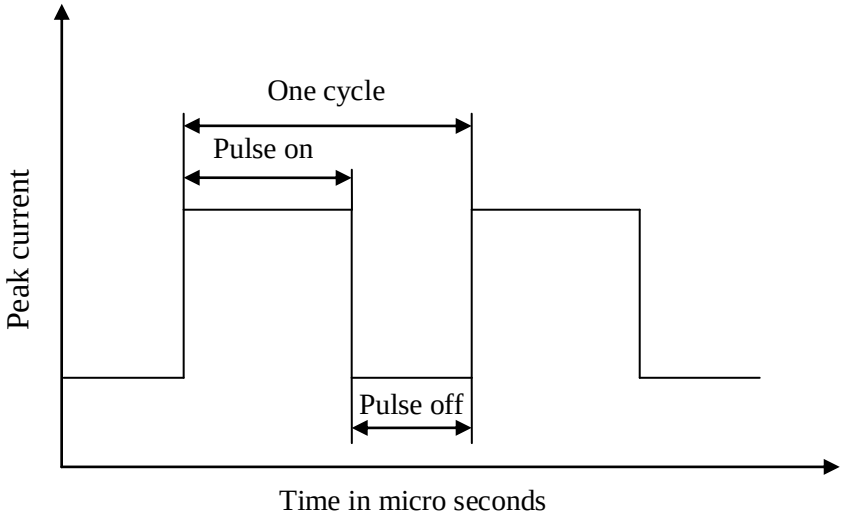

Figure 1.2 Pulse waveform of controlled pulse generator [4]

1.5 EDM DISCHARGE PHENOMINA

The discharge process during EDM separated into three main phases which are: preparation phase, discharge phase, interval phase.

1.5.1 Preparation Phase

When the generator switches on voltage, the electrical field reaches highest strength in the between the electrode. In the presence of electrically conductive particles in the gap, thin particle bridges are formed. When the strength of the electric field exceeds the dielectric strength of the medium, electric breakdown of the medium takes place. Ionization of the particle bridges takes place and a plasma channel is formed in the gap between the electrodes. A minimum 3A current is needed to start the discharge. The steps in this phase are shown in the Fig 1.3 (a)

1.5.2 Discharge Phase

In this phase plasma channel develop in the shortest time against front of dielectric and a very high pressure inside the channel creating shock wave distribution setup within liquid. High temperature is generated on both electrodes due to current passing through, resulting in material evaporation. The momentum with which positive ions strike the cathode surface

is much less than the momentum with which the electron stream impinges on the anode surface. So material removal rate of cathode is less compared to anode. Current density and temperature decrease quickly with continuous growth of plasma channel. More energy is distributed to cathode where material at plasma spots become molten. Steps, during the discharge phase, are shown in Fig 1.3 (b).

1.5.3 Interval Phase

When the discharge is ended by switch off the generator, the plasma channel is de-ionize. The gas bubble collapse and material is ejected out from the surface of electrodes in the form of vapors. The evaporated material solidifies quickly when it comes in contact with cold dielectric and debris particles are flushed away from the discharge gap.

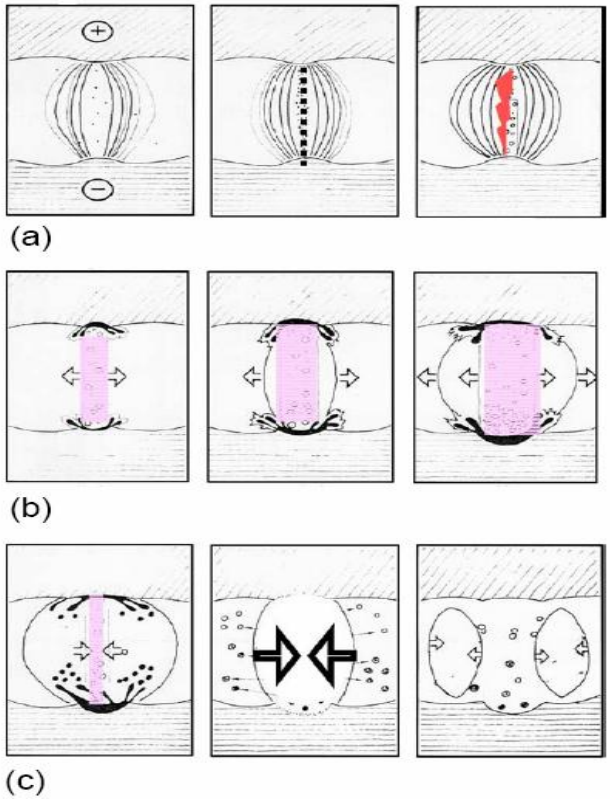

Fig. 1.3 Phases of electrical discharges [5]

1.6 SINKER EDM

Sinker EDM sometimes is also referred to as cavity type EDM or volume EDM. It consists of an electrode and workpiece that are submerged in an insulating liquid called dielectric fluid like kerosene oil. The power supply connected to electrode and workpiece generates an electrical potential between the two parts. As the electrode approaches the workpiece, dielectric breakdown occurs in the fluid forming an ionization channel, and a

small spark is generated in the gap. Due to heat generated work material vaporizes and electrode also evaporates to some extent. These sparks strike one at a time in huge numbers at different locations between the electrode and the workpiece. The spark gap increases after the erosion of the workpiece. Then electrode is lowered down by servo system to maintain the gap voltage. Several hundred thousand sparks occur per second in this process.

The numerical control monitors the gap conditions (voltage and current) and synchronously controls the different axes and the pulse generator. The dielectric liquid is filtrated to remove debris particles and decomposition products.

1.7 EDM PROCESS PARAMETERS

1.7.1 Polarity

Polarity, in EDM process determines the direction of current flow relative to electrode. Polarity of electrode can be either positive or negative depending on applications. In positive polarity workpiece is positive and tool electrode is negative. In negative polarity workpiece is negative and tool is positive. Polarity is also termed as normal and reverse polarity.

With the discharge taking place between workpiece and electrode, electriferrous particles and electrons from the cathode in the dielectric arouse the ionization which produced ionized channel. The particles with positive charge bombard the cathode while electrons bombard the anode in ionized channel. In this process, electrons, which are smaller and lighter, thus accelerate faster and reach higher speed, whereas the particles with positive charge accelerate more slowly and do not reach high speeds. As a result, electrons transfer more energy to anode than positive charged particles to transfer to the cathode. This difference leads to material removal in anode that is greater than material removal in the cathode. Polarity is determined by tool material, work material, current density and pulse length.

1.7.2 Pulse on Time

Pulse on-time is the time period during which machining takes place. MRR is directly proportional to amount of energy applied during pulse on-time. The energy of spark is controlled by the peak amperage and the length of the on-time. Long pulse on time will increase the material removal rate and broader and deep crater than short pulse duration will be produced. These large craters will create a rougher surface finish. Extended on times

gives more heat to workpiece, which means the recast layer will be larger and the heat affected zone will be deeper. Excessive on times exceeding the optimum on time for each electrode-work material combination can reduce the material removal rate.

1.7.3 Pulse off Time

Pulse off-time is the time during which re-ionization of dielectric takes place and no energy is applied on the workpiece surface. The discharge between the electrodes leads to ionization of the spark gap. Before another spark can take place, the medium must de-ionize and regain its dielectric strength. This takes some finite time and power must be switched off during this time. Too low values of pulse off time will increase the top surface temperature of the workpiece and may lead to short circuit. A large value on the other hand will decrease the material removal rate. Each cycle has an on-time and off-time that is expressed in units of microseconds.

1.7.4 Peak Current

This is the amount of power used in discharge machining, measured in units of amperage. Current is a function of heat energy transferred to workpiece. In each on-time pulse, the current increases until it reaches a preset level, which is expressed as the peak current. Higher value of peak current leads to rough surface finish operations and wider craters on work materials. Its higher value improves MRR, but at the cost of surface finish and tool wear. Hence it is more important in EDM because the machined cavity is a replica of tool electrode and excessive wear will hamper the accuracy of machining.

1.7.5 Discharge Current

The discharge current (I_d) is a measure of the power supplied to the discharge gap. A higher current leads to a higher pulse energy and formation of deeper discharge craters. This increases the material removal rate (MRR) and the surface roughness (R_a) value. Similar effect on MRR and Ra is produced when the gap voltage (V_g) is increased. Once the current starts to flow, voltage drops and stabilizes at the working gap level. The preset voltage determines the width of the spark gap between the leading edge of the electrode and workpiece. Higher voltage settings increase the gap, which improves the flushing conditions and helps to stabilize the cut.

1.7.6 Pulse Wave Form

Different wave forms are supplied by different generators. In case of rotating impulse generators the rectified sinusoidal voltage wave form is give across the spark gap to produce the spark. Due to inductive circuitry there is a spark oscillation even after the pulse is withdrawn give rise to extremely high tool wear and arcing become frequent if the second pulse comes before complete damping of oscillation. In relaxation generator, the spark oscillation is reduced. TWR will be less and charging time is equal to ignition delay, so the ionization process is slower and depends on changing time. Pulse wave form, generated by the square pulse generators, is such more defined and easily controllable. Using a generator, which can produce trapezoidal pulses, one can reduce relative tool wear to very low values.

1.7.7 Type of Dielectric Medium Mineral oils exhibiting high dielectric strength and a low viscosity is preferred because of their higher performance. For safety reasons oils with a high flash point are usually used. The fluids used as dielectric are generally hydrocarbon oils. The kerosene oil, paraffin oil, lubricating oil are very common. Water based dielectric are extensively used in Wire EDM because water has high specific heat capacity which leads to better cooling effect required for Wire EDM. In comparison to mineral oils and water, air has lowest dielectric strength, viscosity, thermal conductivity. Air provides high accuracy and better surface finish due to its low viscosity. Whereas MRR using air as dielectric is low and low thermal conductivity and thermal capacity cause higher damage to the workpiece. A good dielectric fluid should have following properties:

(a) It should have dielectric strength (i.e. behave as insulator until the required breakdown voltage between the electrodes is attained).
(b) It should provide effective cooling during operation.
(c) When the breakdown voltage is attained it should take minimum possible time to breakdown, once the break down voltage is attained.
(d) It should able to deionise the gap immediately after the spark has occurred.
(e) It should remain electrically non-conductive until the required breakdown voltage has been reached.
(f) It should have high degree of fluidity.

1.7.8 Type of Flushing

Flushing is the circulation of the dielectric fluid between tool electrode and workpiece during operation. In EDM when discharge occurs the debris are produced in the gap

reducing dielectric strength, which results in unwanted discharges which can damage to both tool and workpiece. To remove unwanted debris from the gap effective flushing is required. TWR and MRR are affected by the type of dielectric and the method of its flushing. Flushing plays a very important role when deep and complex shapes are machined. Flushing can be achieved by following methods:

1.7.8.1 Suction flushing

In this, dielectric may be sucked through either the workpiece or the electrode. To avoid any tapering effect due to sparking between machining debris and the side walls of the electrodes, this technique is well suited. Suction flushing through the tool rather than through the workpiece is more effective.

1.7.8.2 Injection flushing

In this technique, dielectric is fed through either the workpiece or the tool which are pre-drilled to accommodate the flow. With the injection method, tapering of components arises due to the lateral discharge action occurring as a result of particles being flushed up the sides of electrodes.

1.7.8.3 Flushing by dielectric pumping

This method is particularly suitable in deep hole drilling. Electrode pulsation movement is used for flushing. When the electrode is raised, clean dielectric is sucked into mix with contaminated fluid, and as the electrode is lowered the particles are flushed out.

1.7.8.4 Side flushing

Side flushing is employed when the flushing holes cannot be drilled either in the workpiece or the tool.

1.7.9 Electrode Gap

The servo feed system is used to control the working gap at a proper width. Electro-mechanical and electro-hydraulic systems are used to respond to average gap voltage. Larger gap widths cause longer ignition delays, resulting in a higher average gap voltage. The feed control must maintain a movement of electrode towards the workpiece at such speed that working gap does not change which results in changing the average gap voltage. Values of gap size range between 0.005 to 0.05 mm.

1.7.10 Electrode Material

The shape of electrode will be basically same as that of the product is desired. The electrode materials are classified as metallic material (copper, brass, tungsten, aluminium), non-metallic material (graphite), combined metallic and non-metallic (copper-graphite), and metallic coating as insulators (copper on moulded plastic, copper on ceramic) etc. Materials having high melting-point, good electrically conductivity, low wear rate and easily machinability are usually chosen as tool materials for EDM. High density graphite is used in pulsed EDM equipment as it gives low wear due to its high melting temperature. Brass as a tool material has high wear. Copper has the qualities for high stock metal removal. Copper-boron and silver tungsten both exhibit extremely low wear.

1.7.11 Material Removal Rate

The material removal rate is defined as volume of metal is removed per unit time. This depends on large range of properties of the workpiece material, melting point and latent heat. It also influenced by the properties of the tool electrode and geometric factors such as the shape and dimensions of the tool and workpiece.

1.8 POWDER MIXED EDM

Mixing of suitable material in powder form into the dielectric fluid is new advancement in EDM process to improve the process capabilities. This process is known as powder mixed EDM (PMEDM). In this process, the electrically conductive particles are mixed in the dielectric fluid, which reduces its insulating strength and increases the spark gap distance between the tool and workpiece. This leads to spread the electric discharge uniformly in all directions. As a result; the process becomes more stable thereby improving material removal rate (MRR) and surface finish.

Fig 1.4 shows that in PMEDM there is a separate tank for the dielectric fluid. Reason of using separate tank is because every time when new experiment is conducted, concentration of powder and its type may be different. So in this case tank need to be cleaned and again refilled with new dielectric medium and powder particle type and concentration. A motorized stirrer is used to circulate the powder mixed dielectric.

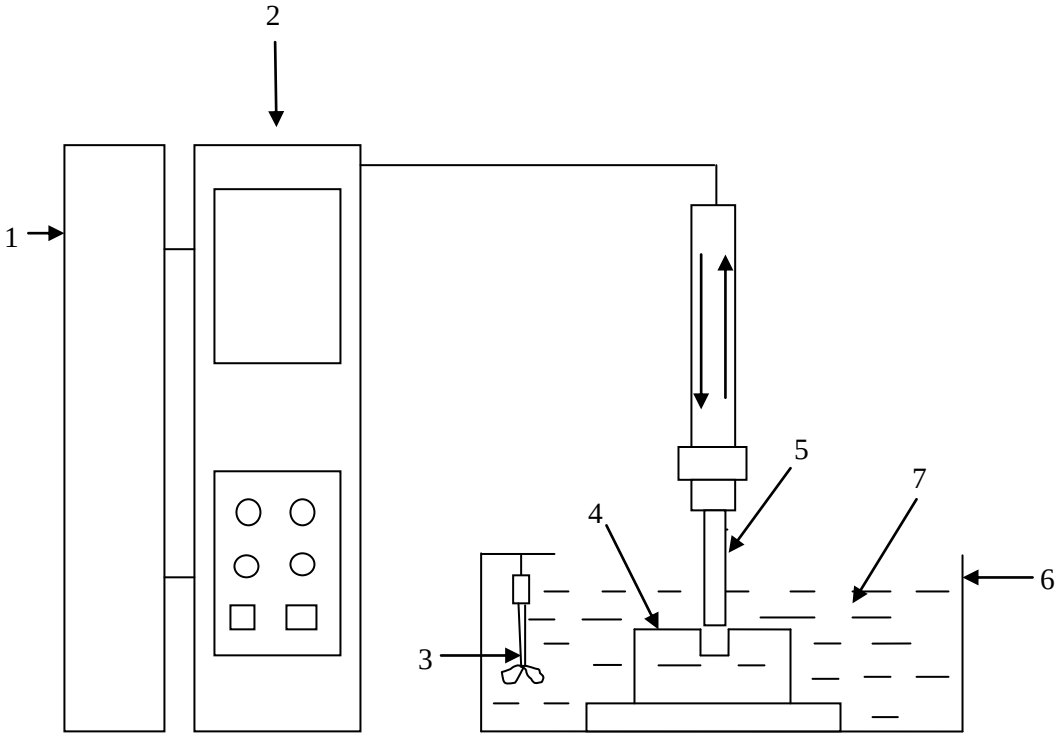

Fig 1.4 schematic diagram of powder mixed EDM

1. Power supply
2. ZNC generator
3. Stirrer
4. Workpiece
5. Electrode
6. Tank
7. Dielectric

1.9 ORGANIZATION OF SEMINAR

Chapter1 covers brief introduction to non-conventional machining, principle of electric discharge machining, mechanism of material removal and process parameters of EDM and powder mixed EDM.

Chapter 2 presents the extensive literature review of research work which has been done by different researchers in the past .This literature is divided into two categories: FEM of powder mixed EDM, FE Modelling of EDM and experimental validation

Chapter 3 covers problem formulation for the thesis work. It presents the simulation methodology and experimental methodology to be adopted.

CHAPTER 2
LITERATURE REVIEW

2.1 INTRODUCTION

A large work has been done on different aspects of EDM. This chapter covers the literature on thermal modelling of EDM, PMEDM, its process parameters and crater formation.

2.2 CATEGORIZATION OF LITERATURE

Literature is divided into following three main categories:

1. FEM of powder mixed EDM
2. FE Modelling of EDM and experimental validation

2.2.1 FEM of Powder Mixed EDM

Kansal et al. [6] developed an axis-symmetric two-dimensional model for powder mixed electric discharge machining (PMEDM) using the finite element method (FEM). The model utilized the several important aspects such as temperature sensitive material properties, shape and size of heat source (Gaussian heat distribution), percentage distribution of heat among tool, workpiece and dielectric fluid, pulse on/off time, material ejection efficiency and phase change (enthalpy) etc. to predict the thermal behavior and material removal mechanism in PMEDM process. The developed model first calculates the temperature distribution in the workpiece material using ANSYS (version 5.4) software and then material removal rate (MRR) was estimated from the temperature profiles. The effect of various process parameters on temperature distributions along the radius and depth of the workpiece were reported. Further validation of the model was done by comparing the theoretical MRR with the experimental one obtained from a newly designed experimental setup developed in the laboratory. The model was developed for a single spark. Material flushing efficiency is assumed to be 20%. It was investigated that powder particles suspended into the dielectric fluid increase the electrical conductivity of the dielectric fluid and help to spread the discharge uniformly in all directions resulting in increased energy transfer to workpiece compared to EDM. 9% of the total heat lost to the workpiece was assumed. Specific heat of melting and evaporation was considered. It was found that the craters are shallow and smaller in size compared to EDM. A new parameter

K_n was introduced into the heat flux equation to take into account the effect of powder on spark frequency and breakdown voltage. Equation used for heat flux was given by

$$Q_w(r) = \frac{4.57 K_n V_b I R_w}{\pi R^2} e^{-4.5\left(\frac{r}{R}\right)^2} \tag{2.1}$$

The modeling and simulation of results for PMEDM were performed using ANSYS software. Meshing of the workpiece domain was done using mapped meshing technique. AISID2 die steel was considered as the workpiece material and copper as a tool material. It was observed that top surface temperature goes on increasing with increase in current and with increase in pulse duration, the surface temperature also increases. The effect of pulse off time was studied by keeping the pulse duration constant. It was clear from the curves that the top surface temperature of the workpiece increases as the pulse off time decreases.

2.2.2 FE Modeling of EDM and Experimental Validation

Marafona and Chousal [7] developed a thermal–electrical model for sparks generated by electrical discharge in a liquid media. Shape used was cylindrical for the discharge channel created between the electrodes. It was clarified that discharge channel being an electrical conductor will dissipate heat, which can be explained by the Joule heating effect. Joule heating arises when the energy dissipated by an electrical current flowing through a conductor is converted into thermal energy. The amount of heat dissipated varied with the thermal–physical properties of the conductor; as a result, the maximum temperature reached was different. In this model, the radii value of the conductor is a function of the current intensity and pulse duration. The thermal–physical values used in the model were the average of both the ambient and melting value. Copper and iron were used for anode and cathode, respectively. The Finite Element Analysis results were compared with the experimental values of the table of AGIE SIT used by other researchers. The Tool Wear Ratio (TWR) and Material Removal Rate (MRR) as well as surface roughness results agree reasonably well with the researcher's values. Joule heating effect was considered in the EDM electrodes and discharge channel. Heat source for both electrodes was given by the current intensity flux transformed into thermal energy due to Joule heating effect, which reached 50% of the pulse power. In this equivalent heat input radius, dependent of the current intensity (I) and pulse duration (t), was used

$$R = 2.04 \times 10^{-3} I^{0.43} t^{0.44} \quad (2.2)$$

This is a virtual radius (constant) for each current intensity case used to get a static thermal electrical model. The supply of the heat to the parts of the model was variable with the thermal–electrical properties of the vaporized dielectric and both electrodes. The heat flux fractions used in the modeling of EDM varies from the different approaches. This model used a Joule heating factor of 50%

Das et al. [8] developed a finite element-based model for the sinking-EDM which uses process parameters such as power input, pulse duration, etc., to predict the transient temperature distribution, liquid- and solid-state material transformation, and residual stresses induced in the workpiece as a result of a single-pulse discharge. This model was able to predict the shape of the crater that is formed as a result of the material removal. The model was validated using experimental data at the possible points. To simulate the effects of a single spark model used finite element method in "DEFORM" software. It was found that close to the spark location, a single spark discharge can provide residual stress of the order of the tensile strength producing micro cracks in white layer. Stress vs. depth plots indicate that the residual stress levels may reach very high values close to the surface but they disappear very quickly in the sub-surface region.

The Gaussian heat input model is used to approximate the heat from the plasma. Model has two factors, the fraction of heat applied to the workpiece and the radius of the area heated by the plasma. On the basis of previous researcher's data Shuvra das and others concluded that the fraction of the total heat that goes into the cathode is about 18% (can be assumed constant), the amount of heat absorbed by the anode is about 8–9%, and the rest of the heat goes into the dielectric. It was investigated that Shape of the crater is a depression in the middle with edges that are raised above the surface. To simulate the protruding edges a pressure boundary condition is applied on the molten pool and the pressure is kept on until the pulse-on time.

Joshi and Pande [9] carried out numerical analysis of the single spark operation of EDM process considering the two-dimensional axis-symmetric continuum. The analysis was based on Gaussian distribution of heat flux, spark radius equation based on discharge current and discharge duration, latent heat of melting to predict the shape of crater cavity and the material removal rate (MRR). Using the developed model, parametric studies were carried out to study the effect of EDM process parameters such as discharge current,

discharge duration, discharge voltage and duty cycle on the process performance. Experimental studies were carried out to study the MRR and crater shapes produced during actual machining. When compared with the reported analytical models, it predicted results closer to the experimental results.

The heat equation entering the workpiece due to EDM spark was taken as

$$q(r) = q_0 \exp\left\{-4.5\left(\frac{r}{R_{pc}}\right)^2\right\} \tag{2.3}$$

Further maximum heat flux q_0 was calculated as

$$q_0 = \frac{4.57F_cVI}{\pi R_{pc}^2} \tag{2.4}$$

where F_c was fraction of total EDM spark power going to the cathode, R_{pc} spark radius at the work surface. Equivalent heat input was taken as

$$R_{pc} = (2.04e-3)I^{0.43}T_{on}^{0.44} \text{ (µm)} \tag{2.5}$$

Equivalent heat input at cathode was given by

$$q(t) = \frac{3.4878\times10^5 F_cVI^{0.14}}{T_{on}^{0.88}} \exp\left\{-4.5\left(\frac{t}{T_{on}}\right)^{0.88}\right\} \tag{2.6}$$

ANSYS^{TM} 10.0 was used. A two-dimensional continuum of size ten times the spark radius was considered for the analysis. The nodes showing temperature more than melting point were selected and eliminated from the complete mesh of the work domain for further analysis. It was found that the MRR values predicted by model were closer to the experimental results when compared with all the earlier reported analytical models. Similarly, the crater cavity shapes predicted were found to be more realistic.

Ghosh and Singh [10] proposed thermo-electric model which gives a general method of calculating the electrostatic force on the surface of the cathode and the stress distribution inside the metal during a discharge. The model suggests that the electrostatic forces are the major cause of metal removal for short pulses and melting becomes the dominant phenomenon for long pulses. The model also predicts that for, short pulses the crater depth is proportional to $I^{1/2}$ which is confirmed by the experiments. It was investigated

that electrostatic force acting on the surface is a very important factor in the removal of metal for short pulses. For long pulses (discharge duration > 100 ms), electrostatic force becomes very small and does not play a significant role. The electrostatic force acting on the metal surface and the stress distribution, variation of the yield strength with depth and crater depth inside the metal due to electrostatic force was estimated. It was found that for short pulses the effect of the temperature is not visible. However, for medium pulses (discharge duration between 5 and 100 ms), temperature plays an important role in decreasing the yield strength of the metal and hence, increasing the depth of the crater formed. For long pulses, the spark radius becomes very large and as a result, the stress acting on the surface becomes very small. So, the temperature becomes the key factor and the electrostatic force does not play a significant role. Therefore, as the spark radius increases, the stress in the inner region remains unchanged as long as the spark radius is small compared to the crater depth, *z*. This happens in the case of short pulses where the spark radius always remains small compared to the crater depth. However, for long pulses, the spark radius becomes large after sometime and the stress in the region where yield takes place, is not independent of the spark radius. Yielding occurs when the Von-Mises stress is more than the yield strength. Relation for the crater depth was given as:

$$Z = \left(\frac{3I\sqrt{2m_i\left(\frac{-\Phi_w}{e}\right)}}{\pi S_y(0, z, t_d)} \right)^{\frac{1}{2}} \tag{2.7}$$

The variation of the crater depth with the discharge duration using stainless steel cathode and kerosene as the dielectric was estimated. For small values of t_d, the spark channel radius is very small and the stress distribution on the surface acts as a point force. It was concluded that the stress distribution due to the electrostatic force is independent of the spark channel radius and hence, the discharge duration t_d.

Ekmekci et al. [11] proposed procedures and results for experimental work to measure residual stresses and hardness depth in electric discharge machined surfaces. Layer removal method was used to express the residual stress profile as a function of depth caused by a die sinking type EDM. Thin stressed layers were removed from machined samples by electrochemical machining. Corresponding deformations due to stress relaxation were recorded for each removal to determine the stress profile from elasticity

theory. The relational dependence of the machining parameters with residual stresses was obtained and a semi-empirical model was proposed for plastic mold steel for de-ionized water as dielectric liquid. Stresses were found to be increasing rapidly with respect to depth, attaining to its maximum value, around the yield strength, and then fall rapidly to compressive residual stresses in the core of the material since the stresses within plastically deformed layers were equilibrated with elastic stresses.

Yadav et al. [12] developed a finite element model to estimate the temperature field and thermal stresses due to Gaussian distributed heat flux of a spark. Developed code calculated the temperature in the workpiece and then the thermal stress field was estimated using this temperature field. The effects of various process variables (current and duty cycle) on temperature distribution and thermal stress distribution had been reported. To validate the code results on temperature distribution were compared with numerical results of other author. Gaussian heat flux distribution with energy partition (R_w) value of 0.42 was used for the calculation of temperature distribution. Kerosene was used as dielectric having convective heat transfer coefficient as 10,000 W/m^2 K. Numerical simulations were performed to predict thermal stress fields in HSS workpiece by developing a finite element based code. It was observed that, after one spark, substantial compressive and tensile stresses develop in a thin layer around the spark location. It was also found that the thermal stresses exceed the yield strength of the workpiece mostly in an extremely thin zone near the spark.

Schulze et al. [13] proposed that comparison of measured crater geometry with simulated ones is a very important method to determine the connections of the physical processes and the parameters of the process energy source. An analytical relation between pulse parameters and roughness was achieved and differences between a single discharge and a sequence of discharges were described. Simulations of thermal-affected zones were identified for a single discharge and a sequence of discharges. The characteristics describing the changed gap conditions of the discharge types in the simulation model were shown. For the tests the confocal laser scanning microscopy (CLSM) was used. Specific crater geometry analyses of the electrode arrangements were accomplished with the scanning electron microscopy (SEM). The CLSM is faster and the accuracy of ±0.5µm. 3D patterns of the crater configurations were drawn up. High speed framing camera (HSFC) permitted temporal resolutions of the discharge from 5 to 200 ns. Results of the different research methods (CLSM, HSFC and ANSYS) were combined in order to extend

the real physical conditions for the discharging process and surface heating. The change of the pulse parameters also lead to purposeful changes in the plasma channel parameters which could be determined partly from the HSFC images. The physical effects such as Pinch effect, temperature and pressure dependence of the enthalpy, specific heat capacity, heat conductivity, and the distribution of the energy parts in the plasma channel and on the electrode faces were considered.

Panda and Bhoi [14] used a transient thermal model for a very large solid cylinder to predict the size of the crater obtained under a single spark by determining the melting isotherm in both the axial and radial directions. An analytical study of the effect of plasma channel radius, heat flux, and pulse duration on the size of the crater was made. Experiments were conducted using a commercial electro-discharge machine. Measurement of craters was done under microscope and a comparison with theoretical results was presented. Variation of crater diameter, crater depth and volume of material removed with respect to different machining parameters such as 'ON' time, 'OFF' time, and current had been explained by the theoretical results and it was concluded that the plasma channel grows with respect to pulse duration such that at the end of the pulse the plasma channel radius becomes equal to the crater radius. It was investigated that the pulse duration, power, and size of plasma channel radius including its growth are the prime factors that decide the size of the crater under a single spark.

Ekmekci et al. [15] used layer removal method to measure the residual stress profile as a function of depth beneath the surface caused by die sinking type EDM. Cracking and its consequences on residual stresses were also studied on samples machined at long pulse durations. A modified empirical equation was developed for scaling residual stresses in machined surfaces with respect to operating conditions. a unit amplitude shape function representing change in curvature with respect to removal depth was proposed in this model. The proposed form was found to be a special form of a Gauss Distribution. It is the sum of two Gaussian peaks, with the same amplitude and pulse width but opposite center location. The form could be represented by three constant coefficients. These coefficients depend on the released energy by a power function.

Sanchez et al. [16] presented a computer simulation model of the EDM process based on the numerical calculation of temperature fields within the workpiece, from which the amount of part material removed per discharge can be estimated. The objective was to theoretically predict material removal rate (MRR) and the final surface finish of the

machined part using as input variables the EDM process parameters and the properties of the work material. Validation was done by carrying out tests on an industrial EDM machine, predicting MRR and surface roughness with errors below 9%. Further results were compared with EDM tests carried out on an ONAH300 industrial EDM machine using work material AISI D2 tool steel. The model generated EDM-ed surfaces by calculating temperature fields inside the workpiece using a finite difference approach, and taking into account the effect of successive discharges. The model had been implemented on computer simulation software. OOP programming had been used. The influence of the parameters that govern the model, namelyR_p, T_{eq} and Q_w were analyzed using ANOVA. Results shown that material removal rate was mainly influenced by Q_w and T_{eq}, whereas the higher influence on surface finish was owing toR_p.

Salah et al. [17] presented results based on numerical model for predicting temperature distribution due to electric discharge machining process. Using temperature distribution the material removal rate and the total roughness were deduced and compared with experimental observations. It was found that taking into account the temperature variation of conductivity is of crucial importance and gives the better correlations with experimental data. Gaussian heat input model was used to approximate heat from the plasma. Fraction of heat applied to the workpiece was estimated using relation

$$Q_{(r)} = \frac{UIF_cT_d}{S_0} e^{\{-4.5\left(\frac{r}{R}\right)^2\}} \quad . \quad (2.8)$$

Where R is the radius of the plasma channel in mm, U is electric potential, I current density, T_d the time of discharge, F_c fraction of power to the cathode and S_0 the section of the initial plasma channel.

Panda [18] used close form solution of three-dimensional heat conduction transient as forcing function to obtain the mathematical expression of thermal stresses. The temperature distribution function was obtained considering electro-discharged machine surface infinite both axially and radially. While doing parametric study to characterize the thermal stress distribution spatial and chronological variation of the heat source was considered. Model provided simpler mathematical expressions to compute thermal stress components. It was investigated that after a spark, significant magnitude of stress is developed around the crater extending from the top surface to about more than twice the

crater depth, which is in excess of the ultimate stress. Further, could be inferred that the pulse duration, power, and plasma channel radius are factors influencing temperature developed under the spark and thermal stresses. Higher heat flux, and longer pulse duration were found to be the cause of relatively higher thermal damage in EDM. Both way experimentally and theoretically it was found that a network of crack initiates from the top edge of the crater and propagates towards the bottom of the crater surface.

Izquierdo et al. [19] gave a new contribution to the simulation and modeling of the EDM process. Temperature fields were numerically calculated using a finite difference schema within the workpiece generated by the superposition of multiple discharges, as it happens during an actual EDM operation. Energy transferred onto the workpiece, diameter of the discharge channel and material removal efficiency were estimated using inverse identification from the results of the numerical model. Then validation of model was done through industrial EDM tests, showing that it can efficiently predict material removal rate and surface roughness with errors below 6%.it has been shown that superposition of multiple discharges must be considered, since the amount of material removed per discharge increases (as much as 50%) as the operation progresses.

Philip and Xiaolin [20] presented process simulation and residual stress analysis for the micro-EDM machining on molybdenum. Material removal was analyzed using a thermo-numerical model by simulating a single spark discharge process. Using the numerical model, the effects of important EDM parameters such as the pulse duration on the crater dimension and the tool wear percentage were studied. Experimental single-spark crater sizes were investigated using scanning electron microscopy and optical evaluation methods and the results compared to the model. Results from a coupled thermal-structural finite element analysis were also presented to show how the thermal action of the micro-EDM process affected the surface integrity of machined workpiece.

Tan and Yeo [21] reported a heat conduction analysis using an expanding circular heat source with time varying heat flux for a single electrical discharge erosion model for micro-EDM. Approach for predicting the machining performance measures considering the effects of multiple discharges was also proposed. The heat conduction analysis allowed the plasma flushing efficiencies (PFEs) in micro-EDM to be determined. For discharge energies of 1.6μJ, 3.4μJ and 14.6μJ, the PFEs at the anode were 19%, 23% and 33%, respectively. The multiple discharge approach generated lower and upper bounds of R_{max} values for micro-EDM, which represents the range of R_{max} values that may exist on

the machined surface. A comparison with the measured R_{max} values was done of surfaces machined at different discharge energies validated the proposed multiple discharge approach.

The FEM simulation was done using ANSYS thermal analysis module for solving transient heat conduction problems. Thermal distribution for a particular load step considers the thermal distribution of the preceding load step as well as loading conditions in the current load step. Two-dimensional model representing half the area of electrode was created. Triangular elements with varying sizes were used. The FEM model was used to estimate the isothermal line corresponding to the melting temperature of the electrode material, for an initially flat surface that represents an unmachined surface. Since the FEM model represents the unmachined surface profile, the resulting melt isotherm can be used to estimate the PFE of an electrical discharge when a comparison is made with the actual crater profile obtained through single discharge experiments.

The FEM parameters specified prior to the analysis include the time dependent data of discharge voltage and current, the time dependent relations for radius of heat source and magnitude of heat flux as well as the total duration of the heat transfer process and the number of separate load steps within this duration. The heat source radius and heat flux at each load step estimated

$$R_n = 0.059.(n.\Delta t)^{0.79} \tag{2.9}$$

$$q_n = \frac{F.V_n.I_n}{\pi.R_n^2} \tag{2.10}$$

Where R_n represents the heat source radius, q_n heat flux, V_n discharge voltage and I_n discharge current at the *n*th load step. The discharge voltage and current data were taken from single discharge experiments conducted on an RC pulse generator circuit.

Kumar et al. [22] Investigated and compared the effect of material transfer from electrode bodies (copper, copper–chromium, and copper–tungsten) and tungsten powder suspended in the dielectric medium during die-sinking EDM of AISI H13 die steel. They concluded that 76 per cent increase in micro-hardness by machining with a copper–tungsten electrode and a 111 per cent increase by machining with tungsten powder mixed in the dielectric. The copper–chromium electrode gave the best surface roughness (Ra) value of 2.67μm. Alloying of parent material with tungsten and tungsten carbide was

shown by Scanning electron microscopy and X-ray diffraction analysis of the machined surfaces.

Soni and Chakraverti [23] investigated changes in chemical compositions of resolidified layers of tool and the workpiece as well as debris using Scanning Electron Microscopy (SEM). Variation in micro-hardness, depth of resolidified layers and heat affected zone were also investigated. They found that appreciable amount of elements migrate from tool to workpiece or vice versa and got alloyed in the resolidified layer. Chemical composition of debris was also changed due to pick up of elements from both the electrodes.

Soni [24] presented the scanning electron microscopy investigation on formation of debris during rotary electro-discharge machining of titanium alloy and high carbon high chromium die steel. Microanalysis of chemical composition of debris was carried out using qualitative energy-dispersive spectroscopy and electron probe microanalysis. Scanning electron micrographs indicated the various types of debris particles collected from the dielectric as well as the particles which remain attached on the workpiece surface. Many distinct types of spheroidal particles (globules) were also seen and the mechanism of their formation was discussed. The chemical composition of these particles was different from its parent material due to migration of material from the rotating tool electrode (copper-tungsten) and the dielectric fluid.

Nowicki et al. [25] dealt with a new method of investigating traces made by individual discharge using scanning profile-meter (SP) and scanning electron microscope. Surface microstructure was assessed using the SEM while dimensions and volumes of individual craters were determined based on scanning profilo-meter. They explained adopted research methodology and examples of the test results for discharges generated during electro-discharge machining (EDM) and electro-discharge alloying (EDA).

Tamura and Kobayashi [26] measured impulsive force transitions in an impulse discharge to clarify the mechanism of material removal. They also examined the mechanism by which the impulsive forces affect the crater formation by impulse discharge.

Singh Gurpreet [27] studied the effect of different input parameters current, workpiece material, electrode material, dielectric medium, pulse on time, pulse off time and powder and some their interactions on the MRR, TWR, micro hardness and surface roughness. Analysis of Variance (ANOVA) was used to analyze effect of input parameters on output response. Deposition of the powder material was also studied. XRD and microstructure

analysis was completed to understand the form and amount of deposition on the surface of the workpiece material.

Singh Gurmail [28] investigated the effect of EDM process on surface properties under different machining conditions. material trasfer to the workpiece surface from electrodes as well as suspended powders in the dielectric medium was also examined. Experimentation was done on different die steels using different electrode materials and different powder particles suspended into the dielectric.

Bhattacharya et al. [29] used Analytic hierarchy process (AHP) for the optimization of the PMEDM process using the experimentally obtained results of MRR, TWR and SR.

Batish et al. [30] explained material transfer mechanism in different die steels using PMEDM process. They shown that material transformation occurs from suspended powder, electrode material and dielectric in free form as well as in compound form.

2.3 GAP IN LITERATURE

A lot of work has been done on PMEDM process; few researchers have worked on the FEM simulation of PMEDM process. Still there is a large scope of work on FEM simulation of Powder Mixed EDM process. Sufficient work has not been done to predict temperature distribution generated in work material, volume removed by a single spark and cooling rate of work material. No work has been done to calculate stresses induced into the work material due to elevated temperatures while machining in process. Most of the authors have assumed that a fraction of total supplied heat is transferred to the workpiece during electric discharge machining. No exact value of that fraction is given by any of the author. Moreover no effort has been done to validate fraction of heat going into workpiece.

2.4 OBJECTIVE OF PRESENT WORK

Simulation work

1. To calculate temperature distribution generated into the workpiece during PMEDM process.
2. To calculate volume of single crater removed by a single spark.
3. To assess cooling rate of the workpiece.

4. To calculate stresses induced into the remaining work material while machining in process.

Experimental Validation

1. To validate simulation results of volume removed by single spark.
2. To predict the close value of fraction of total supplied heat going to workpiece by comparing simulation and experimental results.
3. To predict the machined surface behaviour as an effect of the calculated cooling rate.
4. To study the changes in microstructure of the material due to varying input parameters like current, pulse on, pulse off and powder type and concentration.
5. SEM and XRD observation of the machined surface.

CHAPTER 3
METHODOLOGY

3.1 SIMULATION METHODOLGY

Here in this chapter starting from the development of the thermal model along with the assumptions each step for carrying out simulation is explained. Size of the workpiece, material properties, domain discretization, boundary conditions applied on the simulation model and simulation procedure has been discussed here with an enhanced contrast.

3.1.1 Assumptions for modeling

1. A single spark study is being done in this model.
2. Temperature variable thermal properties have been considered.
3. Gaussian distribution of heat flux is taken in the heat source [31, 32].
4. Material composition is taken as homogeneous and Isotropic [12].
5. Transient temperature analysis has been considered [12, 33].
6. There is no pre stresses on the workpiece before PMEDM process.
7. Material flushing efficiency is assumed to be 100%.
8. Convective heat loss is assumed on the top surface beyond the spark radius R.

3.1.2 Thermal Model

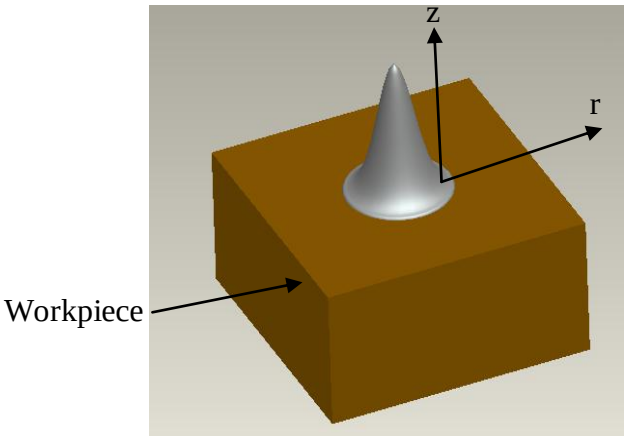

Figureure 3.1: Gaussian heat distribution

Most of the researchers in previous reported works have assumed heat source uniformly distributed within spark [31, 32, and 34]. Actually this assumption does not comply with the reality. In actual heat intensity is maximum at the center of the spark and goes on

decreasing in the radial direction while moving away from spark. In present work, workpiece is being subjected to a heat load with Gaussian distribution. If the maximum heat intensity is Q_0 at center of spark and spark radius R is known then heat intensity at any value of r (radial distance from spark center) is given by

$$Q_w(r) = Q_0 \exp\left\{-4.5\left(\frac{r}{R}\right)^2\right\} \quad [12] \tag{3.1}$$

3.1.3 Workpiece

For the simulation purpose a workpiece of the cube shape with dimensions 0.5x0.5x0.25 mm is studied. Material taken for the simulation is H11 hot die steel. Table 3.1 shows the chemical composition of the work material.

Major applications of H11 (hot die steel) are as follows:

- Pressure casting dies
- Metal extrusion tools for processing light metals
- Forging dies
- Moulds
- Screws and barrels for plastic processing
- Shrink rings
- Hot-shear blades

Table 3.1: Chemical composition of the workpiece material

C	Si	Mn	P	S	Cr	Mo	Co	Cu	V	Fe
0.39%	1%	0.50%	0.03%	0.02%	4.75%	1.1%	0.01%	0.01%	0.5%	Balance

Table 3.2 gives mechanical and thermal properties of the work material.

Table 3.2: Mechanical and thermal properties

Density	7750 kg/m^3	
Tensile yield strength	1.477E×10^9 Pa	
Compressive yield strength	1.477E×10^9 Pa	
Tensile ultimate strength	1.757E×10^9 Pa	
Young's modulus	2.07E×10^{11} Pa	
Poisson's ratio	0.29	
Specific Heat	461.5(J/kg-K)	
T_m (melting temperature)	1426 °C (for H11)	
T_{RC} (re-crystallization temperature)	950 °C	
T_U (unaffected zone temperature)	Below 950 °C	
T_B (boiling temperature)	2986 °C	
Coefficient of thermal expansion	Temperature (ºC)	CTE linear
	204	1.880×10^{-5} /ºC
	649	1.338×10^{-5} /ºC
	750	1.343×10^{-5} /ºC
Isotropic Thermal conductivity	Temperature (ºC)	Thermal conductivity (W/m-°C)
	0	40
	100	38
	200	36
	400	33
	600	29
	1000	29

3.1.4 Heat transferred to workpiece

Many of the previous reported works [34-37] have assumed that entire supplied heat on the surface is transferred to workpiece and there is no heat loss into dielectric medium and electrode. But this assumption is actually not realistic. Patel et al. [32] and DiBitonto et al. [31] assumed that a fraction of total supplied heat on the surface is transferred to the workpiece. They predicted that 8% of the total heat goes to anode and 18% to cathode and remaining heat is taken away by the dielectric medium.

In present work, four different studies have been undertaken wherein the fraction (C_w) heat input to workpiece has been assumed at 4 levels = 0.1, 0.15, 0.2 and 0.25.

3.1.5 Domain Discretization

As mentioned earlier, the size of workpiece is 0.5×0.5×0.25 mm. Heat distribution is assumed to be have Gaussian distribution on the workpiece surface. In the present work, spark radius is taken to be 0.1 mm and the region under spark on the top face has been discretized into 20 different segments. These segments have the radii ranging from 0.01 mm to 0.2 mm diameter with an increment of 0.01 mm.

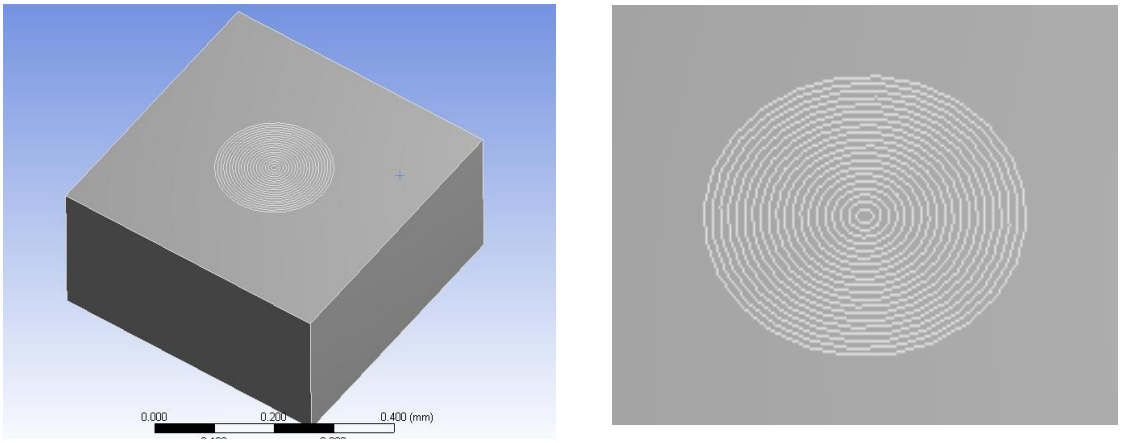

Figure 3.2: Work Domain

3.1.6 Heat flux

Hemispherical disc type heat source has been considered by many researchers in earlier time. As it doesn't comply with the real conditions, an equation for Gaussian distribution has been reported [12]. In present work same equation has been modified as below to consider the effect of powder mixed into dielectric fluid.

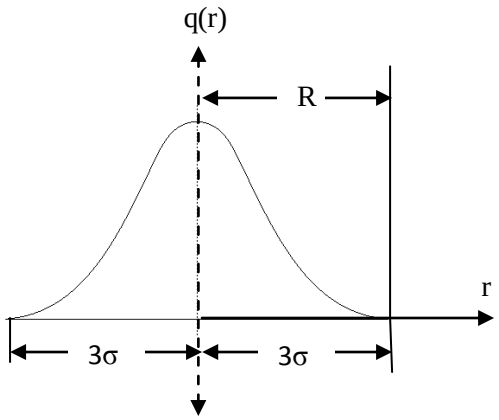

Figure 3.3 Gaussian distribution

Probability density function of Gaussian distribution for a random variable r is given in equation as below:

$$q(r) = \frac{1}{\sqrt{2\pi}\sigma} e^{-\frac{r^2}{2\sigma^2}} \tag{3.2}$$

$\frac{1}{\sqrt{2\pi}\sigma}$ is peak value of distribution and σ is standard deviation.

Mathematically Gaussian curve doesn't become zero until infinity and 99.75% of the data population lies in ±3σ limits for this distribution.

Now R = 3σ substituting the value of σ in equation (3.2)

$$q(r) = \frac{3}{\sqrt{2\pi}R} e^{-4.5\frac{r^2}{R^2}} \tag{3.3}$$

In present work q(r) is the intensity of heat flux on to workpiece denoted by Q_w and is a function of r.

At r = 0, q(r) = Q_0; (Q_0 is maximum intensity of heat at spark center).

So $$Q_w(r) = Q_0 e^{-4.5\frac{r^2}{R^2}} \tag{3.4}$$

Thus energy incident on workpiece is

$$\oint Q_w(r)dA = \int_0^R Q_w(r)2\pi r dr$$

$$= \int_0^R Q_0 e^{-4.5\frac{r^2}{R^2}} 2\pi r dr \rightarrow 0.2191\pi Q_0 R^2$$

Considering the conservation of energy, rate of energy incident on workpiece is equal to rate of energy supplied so

$$0.2191\pi Q_0 R^2 = C_w V_b I K_n \tag{3.5}$$

Where C_w is fraction of heat going to workpiece,

V_b is breakdown voltage (72% of supplied voltage)

I is current in Amp and

K_n is a parameter to take into account the presence of powder mixed on spark frequency and breakdown voltage. The value of K_n depends upon powder particle size, concentration and type of powder.

Modifying equation 3.5

$$Q_0 = \frac{4.57\ K_n V_b I C_w}{\pi R^2} \tag{3.6}$$

Substituting into equation 3.4

$$Q_w(r) = \frac{4.57\ K_n V_b I C_w}{\pi R^2} e^{-4.5\left(\frac{r}{R}\right)^2} \tag{3.7}$$

3.1.7 Heat flux discretization and boundary conditions

3.1.7.1 *Heat flux discretization*

Heat flux is a continuous function of r (radial distance along spark radius). So to descretize the heat flux, there are three possible ways as shown in Figure 3.4(a), Figure

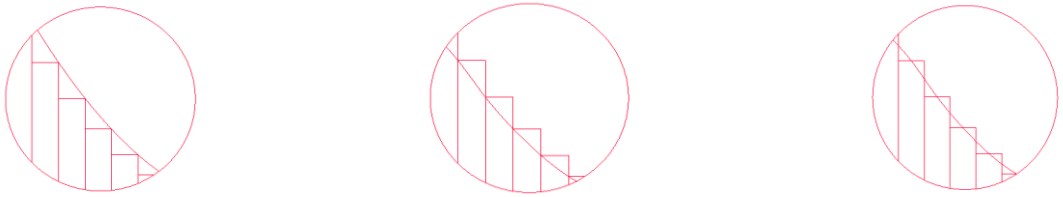

(a) (b) (c)

Figure 3.4 Different methods of descretization of a continuous function (a) conforming, (b) external, (c) central.

Conforming method shown in Figure 3.4(a) predict less than the actual continous function values. Due to its underprediction it is not well suitable for the present work.

External method shown in Figure 3.4(b) overpredict than the actual continous function values.

Mean value method shown in Figure 3.4(c) is the better method to descretize the heat flux as it averages the the other two appraoches. In this method descretization is much more closer to the continuous function, because it is carried out on the mid point. So in present work mean value descretization has been used.

3.1.7.2 *Boundary conditions*

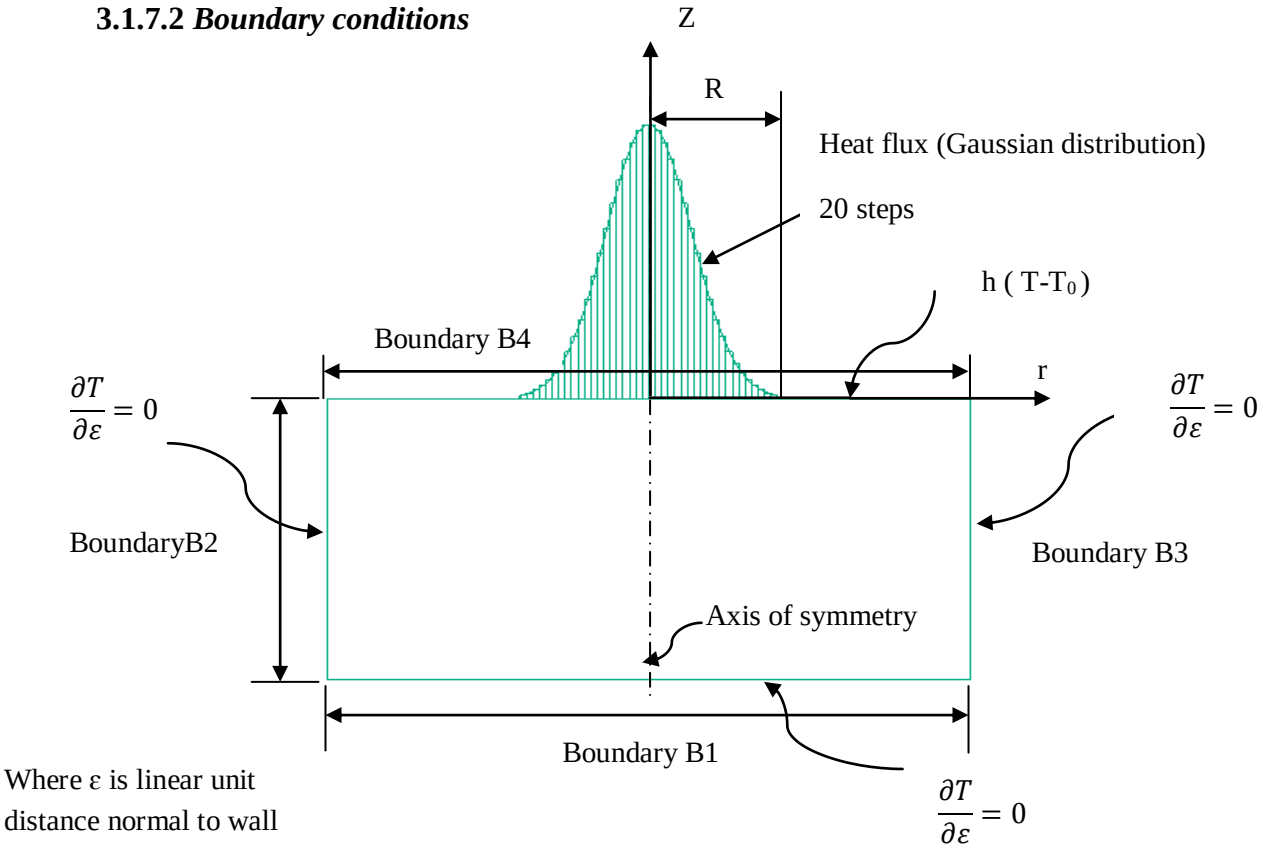

Figure 3.5: Boundary conditions

In present work shape of the heat source with Gaussian distribution is considered and it is symmetric about Z-axis. Intensity of heat at spark center is maximum and it goes on decreasing in radial direction in 20 discrete steps as discussed in 3.1.5.from center of spark. Figure 3.5 shows this distribution of the heat flux for a spark radius of 0.1 mm. the radii of the sub regions range from 0.005 to 0.1 mm with the increment of 0.005 mm. In this way, total area under spark region has been divided into 20 sub areas shown in Figure 3.5 This Heat flux is incident on workpiece on boundary B4 (i.e. top face), starting from the axis of symmetry and upto radius R. Beyond this boundary B4 is exposed to convection heat transfer due to heat loss in powder mixed dielectric fluid.

For boundary B4:

$$K\frac{\partial T}{\partial Z} = Q_w(r) \qquad \text{When } r \leq R \tag{3.8}$$

$$Q_w(r) = \frac{4.57 K_p V_b I C_w}{\pi R^2}\, e^{-4.5\left(\frac{r}{R}\right)^2} \text{ [6]} \tag{3.7}$$

Where

T - Temperature

T_0 - 22 °C

$Q_w(r)$ - Intensity of Heat imparted to workpiece

r - Radial distance from centre of spark

K_P - Powder particle size and concentration factor

V_b - Breakdown Voltage

I - Current

C_w - Fraction of Heat going to workpiece

R - Spark radius

$$K\frac{\partial T}{\partial Z} = h(T - T_0) \qquad \text{When r > R} \tag{3.9}$$

For boundary B1, B2, B3:

$$\frac{\partial T}{\partial \varepsilon} = 0 \tag{3.10}$$

3.1.8 Spark radius

As size of plasma channel is not a constant but grows with time [31]. Theoretical and experimental efforts have been made by some researchers to predict the spark radius [37]. In present work spark radius is taken as 0.1 mm.

3.2 SIMULATION

FEM simulation software, ANSYS version 12.0 (workbench mode) has been used to simulate the PMEDM process. Transient thermal analysis and Static structural analysis module have been used in present work. Transient thermal module in ANSYS has very good capabilities to simulate temperature distribution, directional heat flux, and total heat flux generated into the workpiece due to the applied thermal loading on work material (placed in the dielectric). Different types of thermal loadings like temperature, convection, radiation, heat flow, heat flux, perfectly insulated and internal heat generation can be applied on the workpiece in the transient thermal analysis module. In structural analysis module has the capability to simulate maximum equivalent stress, maximum shear stress, Mohar Coulumb stress, maximum tensile stress, total and directional deformation. In static structural analysis module loadings like pressure, force, bearing load, moment, fixed support, displacement, elastic support, cylindrical support, frictionless support, rotational velocity, acceleration and temperature load imported from the transient thermal analysis simulation etc. can be applied for the simulation purpose.

3.2.1 Geometric modeling

As shown in Figure 3.6, model has been created by simple extrude command. Size of the model is $0.5 \times 0.5 \times 0.25\ mm$. To apply different heat fluxes at different sub areas, 20 different faces have been created on the top face of the model by using extrude as imprint faces command. Diameters of these regions are 10, 20, 30, 40,……..., 200 µm with an increment of 10 µm. Material assigned to model is H11 hot die steel with properties as listed in table 3.2

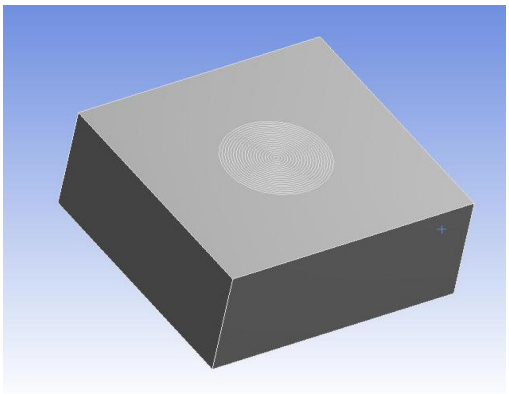

Figure 3.6: Geometric Model

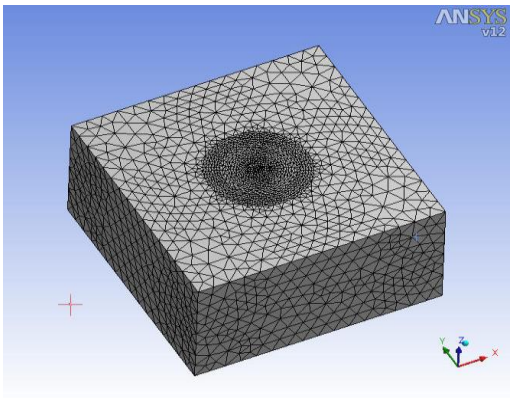

Figure 3.7: Mesh details

3.2.2 Meshing

Figure 3.7 shows that Meshing is fine in the region under spark and coarse at the outer areas which are not directly under the spark. Table 3.3 gives the mesh detail.

Table 3.3: Mesh Characteristics

Type of elements	Tetrahedral
Number of nodes	7830
Number of elements	38398
Element Size	5 µm (max)

Table 3.4 gives the variables used in simulations

Table 3.4: Parameters used in simulation

Current	2, 4, 6 and 8 Amp
Voltage	35 volt (breakdown voltage)
K_p	2.4 (powder particle size and concentration factor)[6]
C_w	0.1, 0.15, 0.2 and 0.25
Pulse On Time	50, 75 and 100 µs
Pulse Off Time	25, 50 and 75 µs
Spark radius	0.1 mm
Initial temperature	22 ℃
T_m (melting temperature)	1426 ºC
T_{RC} (re-crystalization temperature)	950 ºC
T_B (boiling temperature)	2986 ºC
Dielectric	Kerosene (convective heat transfer Coefficient 12000 W/m^2-K)

3.2.3 Heat fluxes applied on the work surface:

Using these variables in Table 3.4 and equation (3.7) heat flux values has been calculated for different sub regions at different settings. These calculated heat fluxes have been used in transient thermal analysis as a thermal loading as shown in Figure 3.8.

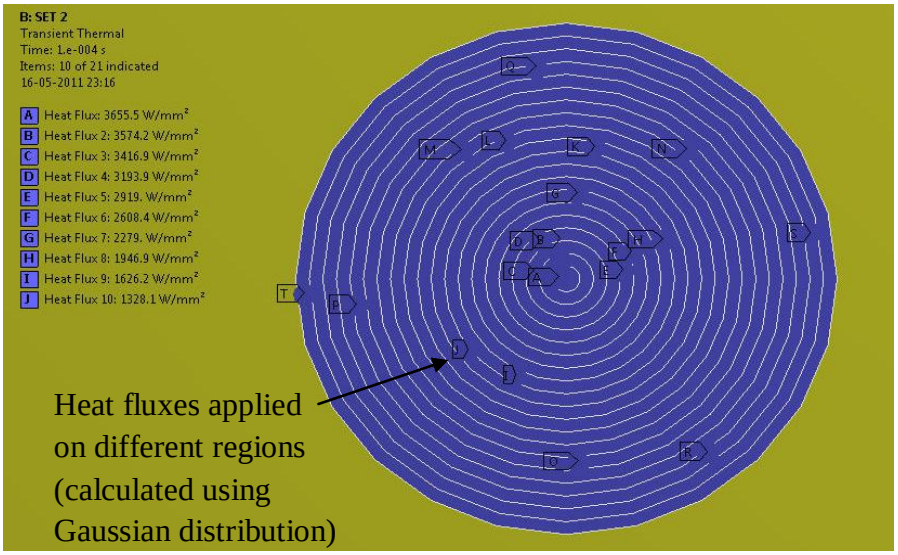

Figure 3.8: Different heat fluxes applied on different locations following Gaussian distribution.

3.2.4 Convection loading

In actual EDM process region under spark is directly affected by the heat flux of spark channel. Beyond the spark radius there is no heat flux active on the work surface. So Figure 3.9 shows that beyond spark radius whole surface is exposed to a convection heat loss due to dielectric medium. Convection used in present work is 12000W/m^2-°C (for kerosene) [12].

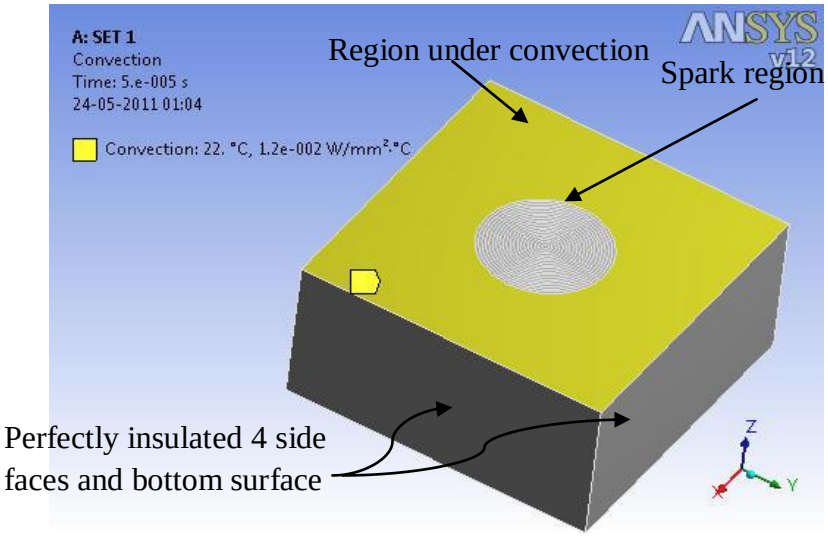

Figure 3.9: Convection applied on workpiece beyond spark region

3.2.5 Static structural analysis:

Here in sample simulation input parameters T_{on} 50 µs, Current 2 Amp, C_w 0.1 and V_d 35 have been used. Temperature distribution shown in Figure 3.10 given by transient thermal analysis has been exported into static structural analysis as a pre thermal loading.. To find out stresses into the workpiece displacement constraints have been applied on the boundaries as shown in Figure 3.11, and Figure 3.12.

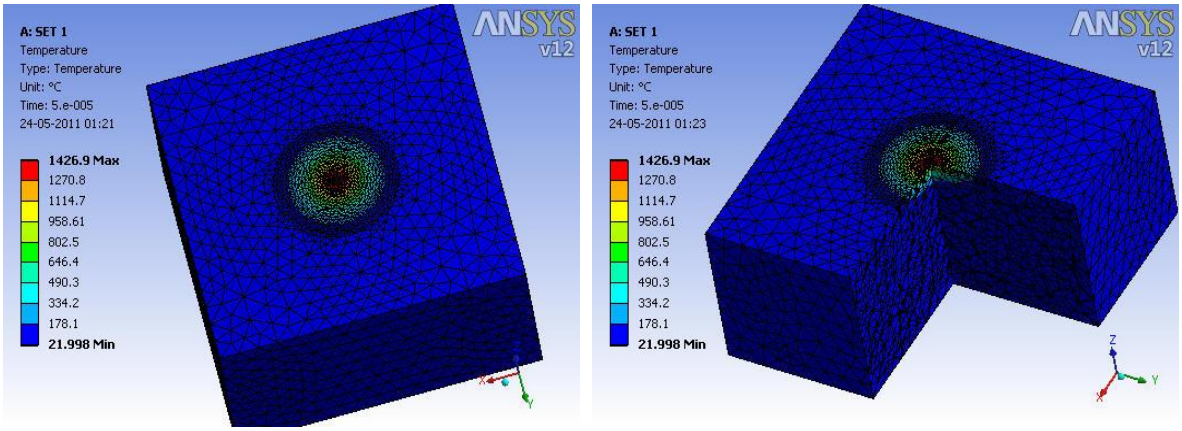

a) General view b) Sectional view

Figure 3.10 Transient thermal analysis Temperature distribution ºC

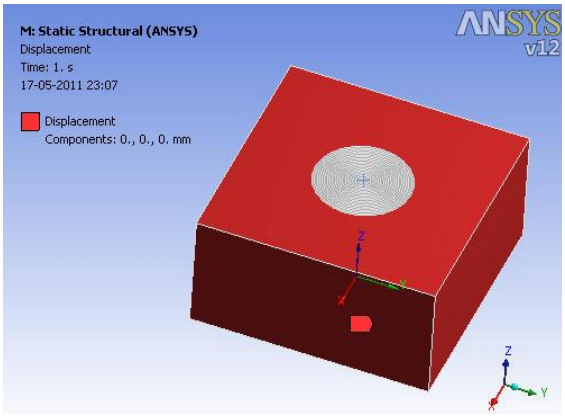

Figure 3.11displacement constraint

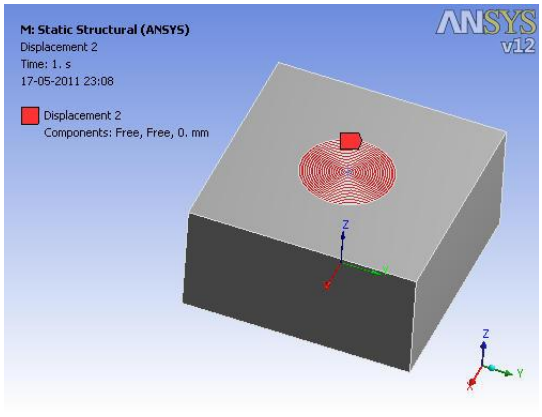

Figure 3.12 displacement constraint

In this case there is no effect of heat on all side faces, bottom face and top face except region under spark channel. As there is no significant temperature gradient on these areas, no thermal expansion will occur. So displacement of theses surface areas is considered 0 in x, y and z directions. Region under spark is heat affected zone so thermal expansion will occur in this region accordingly movement in x, y direction is free but in z direction displacement is 0 for this portion.

3.3 EXPERIMENTAL METHODOLOGY

The experiments are conducted on the Electrical Discharge Machine (Model T-3822) utilizing a special tank (of 9 liter capacity) with a motorized stirrer arrangement shown in Figure 3.13 for proper blending (spatial distribution)of the suspended powder particles in the dielectric medium. The experimental set up with tank mounted is shown in Figure 3.13 and Figure 3.14. Hot die steels H11 workpiece material cut to a size of 100 mm × 70 mm × 10 mm is machined in kerosene. Workpiece is ground on both faces to maintain parallelism. Electrodes of Cu (with 99.9% Cu, 0.045% Ni, and 0.029% Ti) finished to a diameter of 20 mm have been used for the experimentation. Experiments have been conducted in two sets for T_{on} 50 µs and 100 µs.

Figure 3.13 EDM machine

Figure 3.14 Machining in process

3.3.1 Variables used in Experimentation

Table 3.5 gives variables considered in experimental validation

Table 3.5 Variables used in experimentation

Polarity	Workpiece – anode, tool - cathode
Powder type and size	Graphite 300 mesh size
Powder concentration	2 gm/litre
Dielectric	Kerosene
Flushing	On (motorized stirrer)
Work Material	H11
Electrode Material	Cu
Electrode diameter	20 mm
Current Levels	2, 4, 6 and 8 Amp
Pulse on Levels	50 and 100 µs
Pulse off	50 µs

3.3.2 Design for Experimentation

Table 3.6 gives settings for different experiments

Table 3.6 Design of Experiments

SET No.	Current (Amp)	Pulse On (µs)	Pulse Off (µs)
1	2	50	50
2		100	
3	4	50	
4		100	
5	6	50	
6		100	
7	8	50	
8		100	

3.3.3 Crater Diameter and Depth measurements

Diameter of crater is measured using Profile Projector. Nikon Profile projector shown in Figure 3.15 has capability to measure linear distance with an accuracy of 1 µm. Measurement of crater diameter has been carried out for at least 10 different craters locations for single set to minimize the error and take the mean value of the crater diameter. Diameter of each crater was measured six times and averaged to minimize the error in the measurement. A dial indicator shown in Figure 3.17 with dial of least count 0.001 mm is used to measure the depth of the crater. To measure the depth, workpiece is placed on two properly ground V-blocks on the surface plate. A special type needle having a very sharp tip is brazed on the dial plunger. Crater which need to be examined is made just below the needle tip by sliding either work or dial indicator stand. Now pressure on dial indicator is noted down on the un-machined surface near to crater. After that

needle is slightly moved upward and placed exactly into the center of the crater by sliding either dial indicator or workpiece. For proper focusing of center of crater a high magnifying glass is used to focus the needle tip and crater center. Reading at the center of the crater is noted down and difference between this and un-machined surface reading gives the crater depth.

Figure 3.15 Profile projector

Figure 3.16 Electronic panel

Figure 3.17 Inspection setup

CHAPTER 4
RESULTS AND DISCUSSIONS

4.1 SIMULATION RESULTS

In present work following the simulation methodology and utilizing the boundary conditions as mentioned in detail in Chapter 3, simulations were completed to obtain the following sets of results:

1. Temperature distribution generated while transient thermal analysis.
2. Crater volume (volume removed by a single spark).
3. Cooling rate of work material.
4. Stresses induced into the workpiece due to elevated temperatures.

4.1.1 Temperature Distribution

In present work considering the thermal aspects of PMEDM process, spark channel (heat source) is discretized in 20 different sub-regions using Gaussian distribution. To apply the heat on the work surface region under spark channel, spark region was discretized into 20 different sub areas. Heat flux was applied on these discretized areas for the different pulse on time, with corresponding heat flux intensity using Gaussian distribution. Due to heat fluxes applied on the spark region non uniform temperature distribution is generated into the domain. To observe temperature distribution in radial as well as in depth direction temperature plots have been made. Temperature distribution given by transient thermal analysis is exported (in excel file) to plot in radial as well as depth direction. Information in this file is related to each node of the model mesh. It extracts complete information regarding each node i.e. node number, nodal coordinates and temperature generated at each node. A program was developed in Visual C++ 6.0 to sort this excel file containing non uniform distribution and finally make a list of sorted nodes in radial direction and depth direction along with its corresponding temperature. Figure 4.1 shows the complete algorithm for this purpose.

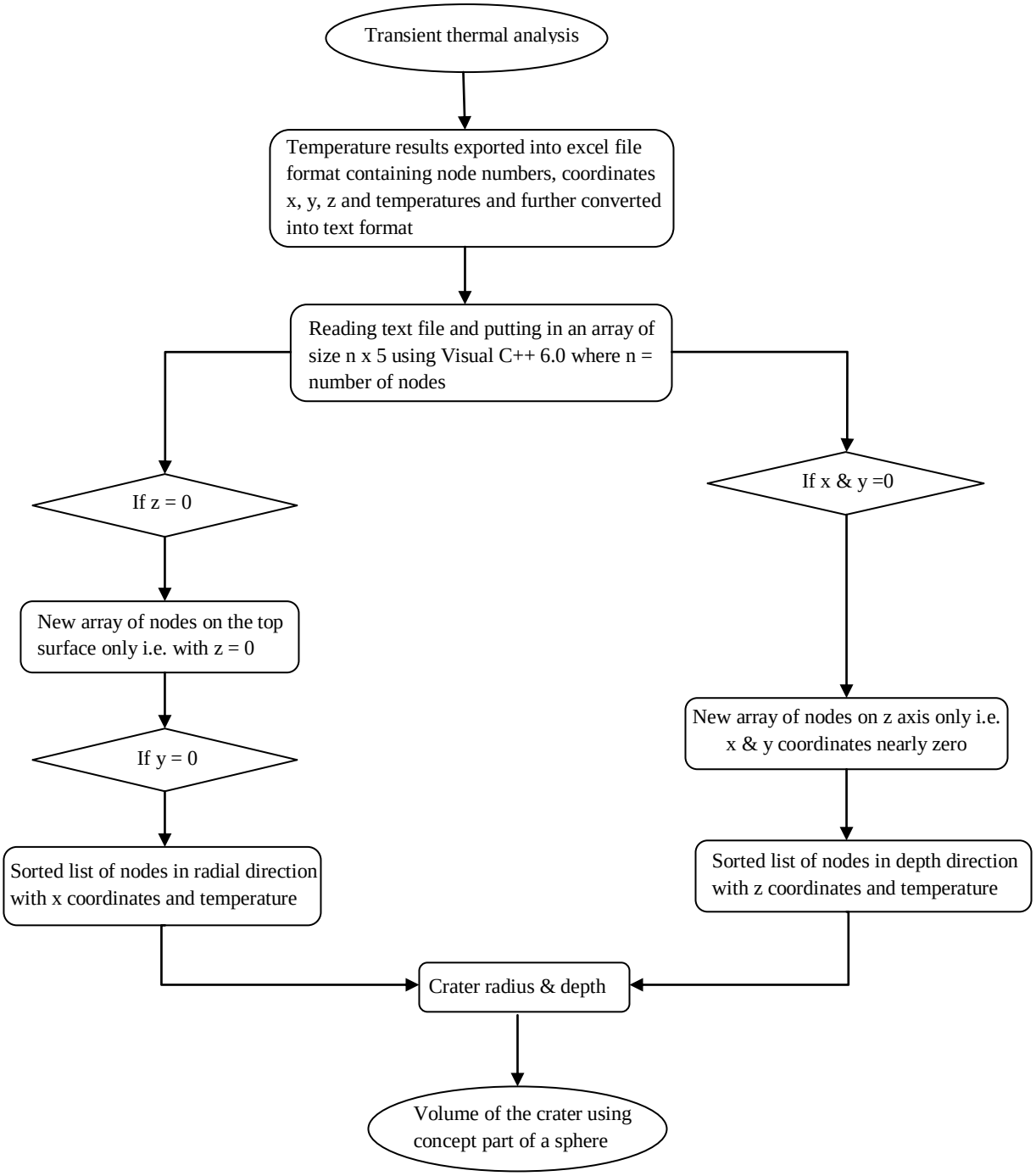

Figure 4.1: Algorithm to illustrate the extraction of nodal coordinates and temperatures above melting temperature to evaluate volume removal for crater

To study the effect of pulse on time, discharge current and C_w on temperature distribution these three parameters have been varied in different combination to execute different set of simulations. Four different levels of currents i.e. 2, 4, 6 and 8 Amp have been used to take into effect of discharge current (I). Pulse on (T_{on}) has been used in three different levels i.e. 50, 75 and 100 µs. C_w (fraction of total supplied heat transferred to workpiece) is taken in four levels i.e. C_w = 0.1, 0.15, 0.2 and 0.25. As shown in Figure 4.2 temperature distribution has been predicted for the pulse on time 50 µs using powder concentration factor K_p = 2.4, discharge Voltage V_d = 35 V, for different values of C_w and

I. From the Figure 4.2 (a) to (d) it is clearly visible that temperature distribution follows Gaussian distribution as it is supposed to. Temperature at the center of spark is maximum and starts decreasing while moving away from center of spark. It is noticed that temperature rises by increasing current and C_w factor. In the Figure 4.2 (a) to (d) temperature distribution is predicted up to spark radius (R) in radial direction. It is inferred from the plots that significant temperature drop is there for different C_w factor near to center of spark and it starts decreasing while moving away from spark center. There is a significant increase in peak temperature developed with increase in current and increase in temperature due to increase in current is more significant as compared to C_w.

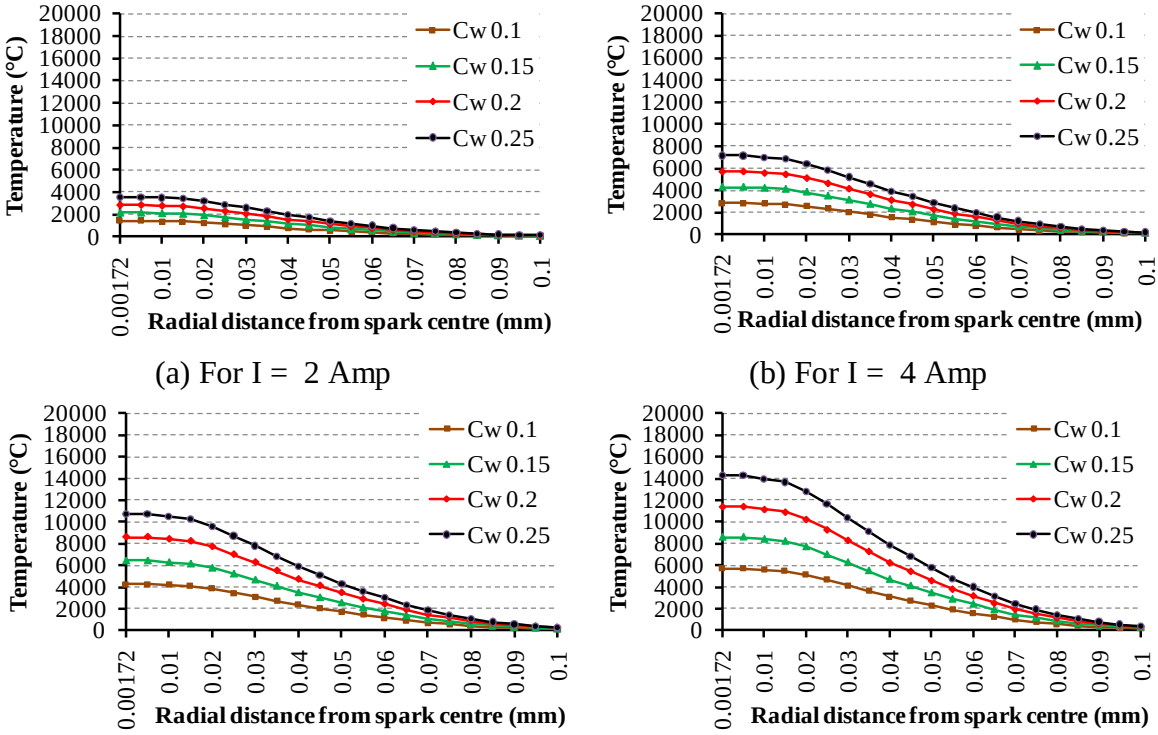

(a) For I = 2 Amp (b) For I = 4 Amp

(c) For I = 6 Amp (d) For I = 8 Amp

Figure 4.2: Temperature distribution in radial direction generated during simulation using K_p = 2.4, V_d = 35 Volt, T_{on} 50 µs for different C_w at different current settings (a) 2 Amp, (b) 4Amp, (c) 6Amp and (d) 8 Amp

To represent results of temperature distribution in the form of 3-D colored contour plots images have been taken for each individual simulation and few of them as sample representation are shown in Figure 4.3. In these particular cases constant T_{on} = 50 µs, C_w = 0.25, K_p = 2.4, V_d = 35 V is taken as input parameter. Four different levels of current, I = 2, 4, 6 and 8 Amp has been used for four different simulations. Red region in the contour plots represent material above melting temperature of H11 (1426^0 C). From the Figure 4.3 (a) to (d) it is clearly visible that red region is the predicted volume to be removed while

actual machining and increases significantly with increase in current. It is also noticed that diameter of crater is much larger than the depth.

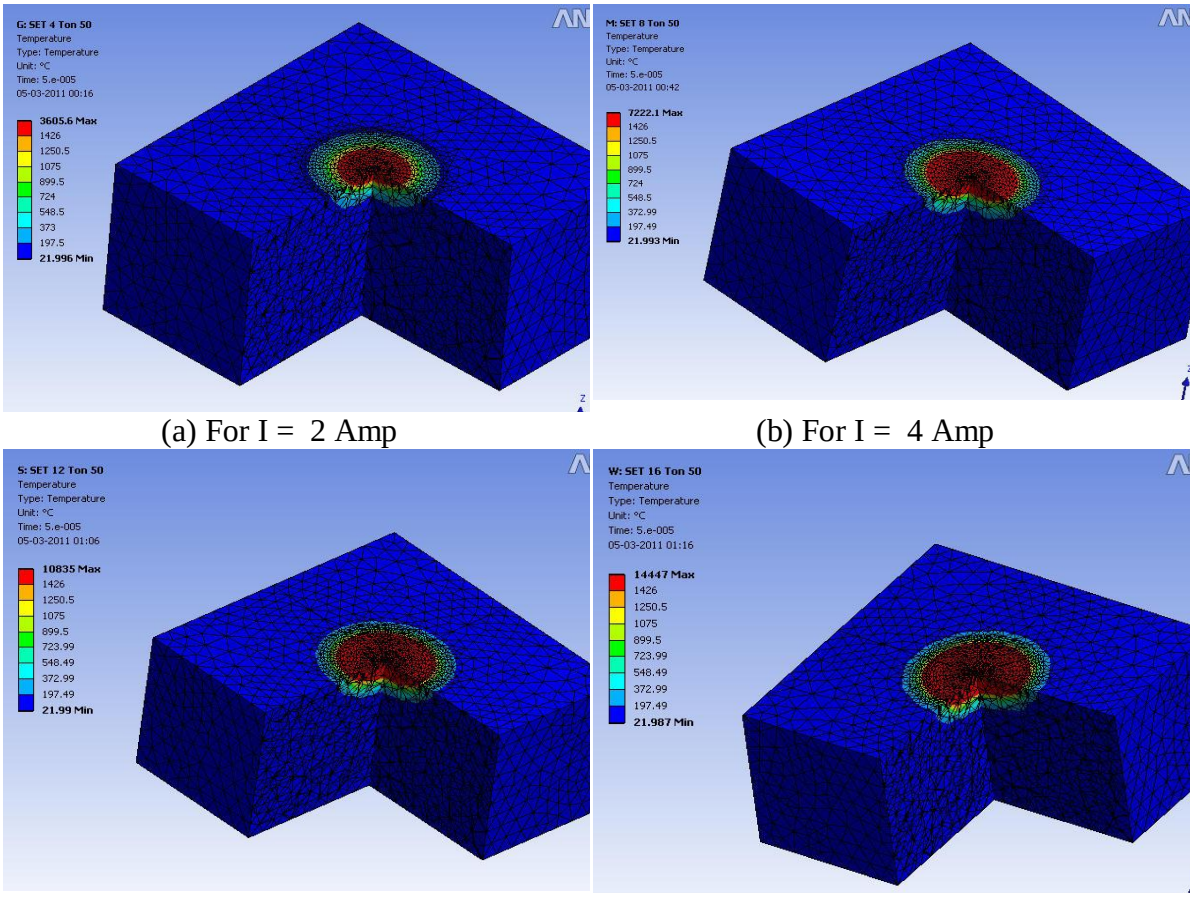

(a) For I = 2 Amp (b) For I = 4 Amp

(c) For I = 6 Amp (d) For I = 8 Amp

Figure 4.3: Temperature distribution with K_p = 2.4, V_d = 35 Volt, T_{on} = 50 µs, C_w = 0.25 and I = 2, 4, 6, 8 respectively

To analyze the PMEDM process with T_{on} = 75 µs another set of simulations is done. As shown in Figure 4.4 (a) to (d) input parameters for these simulations are K_p = 2.4, V_d = 35 Volt, T_{on} = 75 µs, using C_w = 0.1, 0.15, 0.2, 0.25, and I = 2, 4, 6 and 8 Amp. Comparing Figure 4.2 and 4.4 it is confirmed that increasing pulse on time result in significant increase in peak temperature. For the same input current of 8 Amp but different pulse on timings, in Figure 4.4 (d) peak temperature is 16583 °C which is larger than peak temperature in Figure 4.2 (d) i.e. 14291 °C. From the Figure 4.4 (a) to (d) it is confirmed that here also, as of previous case, temperature distribution follows the Gaussian distribution. Peak temperature increases with increase in discharge current.

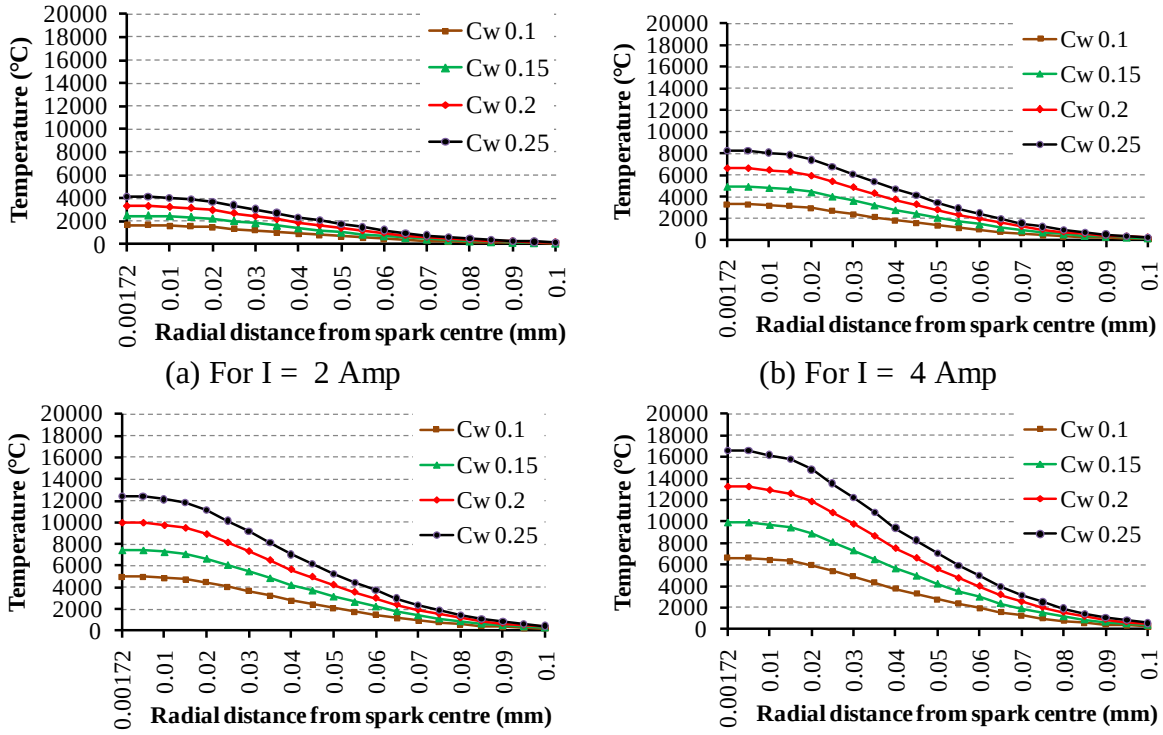

(a) For I = 2 Amp (b) For I = 4 Amp

(c) For I = 6 Amp (d) For I = 8 Amp

Figure 4.4: Temperature distribution in radial direction generated during simulation using K_p = 2.4, V_d = 35 Volt, T_{on} =75 µs for different C_w at different current settings (a) 2 Amp, (b) 4Amp, (c) 6Amp and (d) 8 Amp

Further again to analyze the results of temperature distribution in 3-D colored contour plots images have been taken for each individual simulation. Four different cases as shown in Figure 4.5 (a), (b), (c) and (d) are presented here for observation of 3-D contour plots. In these particular cases constant pulse on time 75 µs, C_w = 0.2, K_p = 2.4, V_d = 35 Volt is taken as input parameter. Four different levels of current had been used for four different simulations. In Figure 4.5 (a) to (d) red region represent material above 1426 °C i.e. melting point of H11 which is supposed to remove to form the crater during dielectric flushing. Volume of the red region increases significantly with increase in current which implies the increase of volume removal with increase in applied current. Comparing Figure 4.3 and 4.5 it is visible that though the C_w factor used in simulation represented in Figure 4.5 is 0.2 which is less than simulation shown in Figure 4.3, still diameter of the predicted melting zone (red region) is larger with pulse on 75 µs than the pulse on 50 µs for same discharge current. So it shows that pulse timing has significant effect on the melting zone in turn the diameter of formed crater.

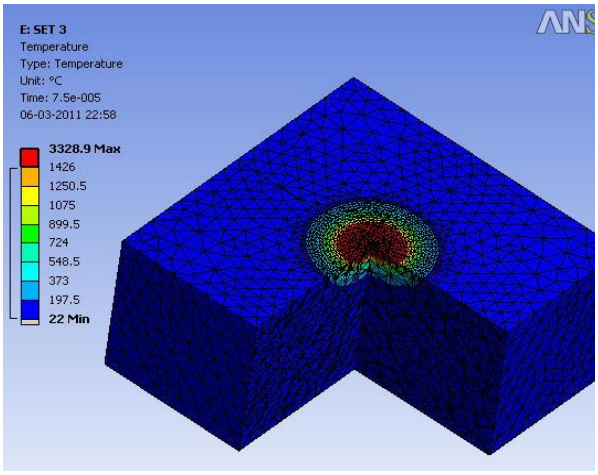

(a) For I = 2 Amp

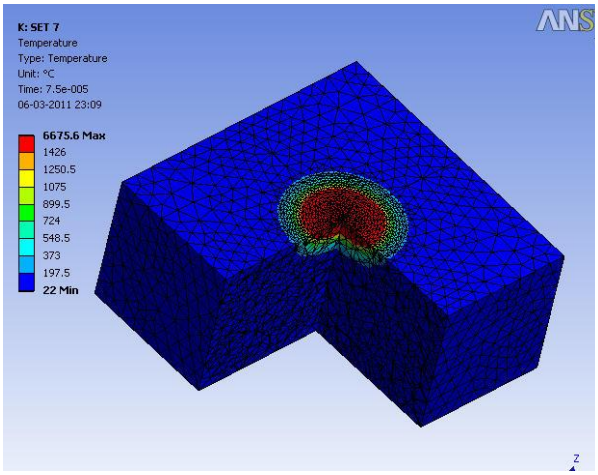

(b) For I = 4 Amp

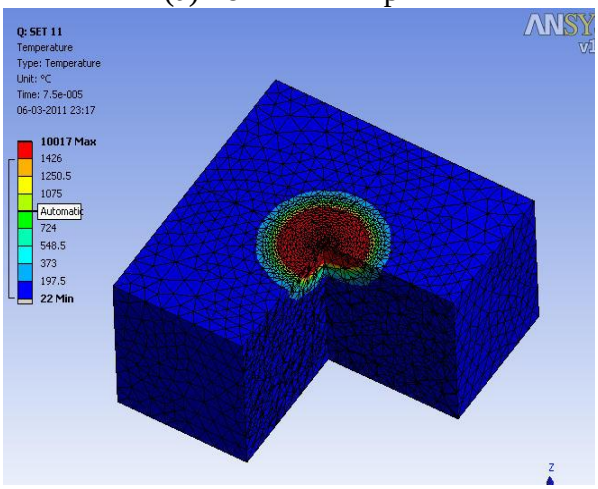

(c) For I = 6 Amp

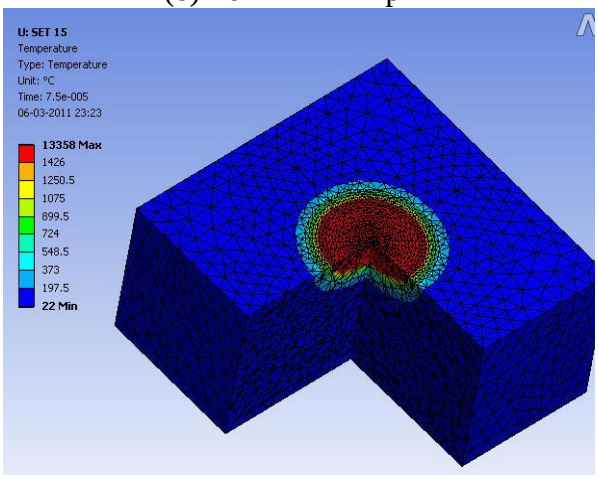

(d) For I = 8 Amp

Figure 4.5: Temperature distribution with K_p = 2.4, V_d = 35 Volt, T_{on} = 75 µs, C_w = 0.2 and I = 2, 4, 6, 8 respectively

Simulation results for pulse on 100 µs are shown in Figure 4.6 (a), (b), (c) and (d) with input parameters K_p = 2.4, V_d = 35 Volt, pulse on 100 µs, C_w = 0.1, 0.15, 0.2, 0.25, and current = 2, 4, 6 and 8 Amp. Comparing Figure 4.2, 4.4 and 4.6 it is confirmed that peak temperature increases considerably by increasing pulse on time. For the same input current = 6 Amp but different pulse on timings, in Figure 4.6 (c) peak temperature is 13636 °C which is larger than peak temperature in Figure 4.4 (c) i.e. 12437 °C. From the Figure 4.6 (a) to (d) it is confirmed that temperature distribution follows the Gaussian distribution and peak temperature increases with increase in discharge current.

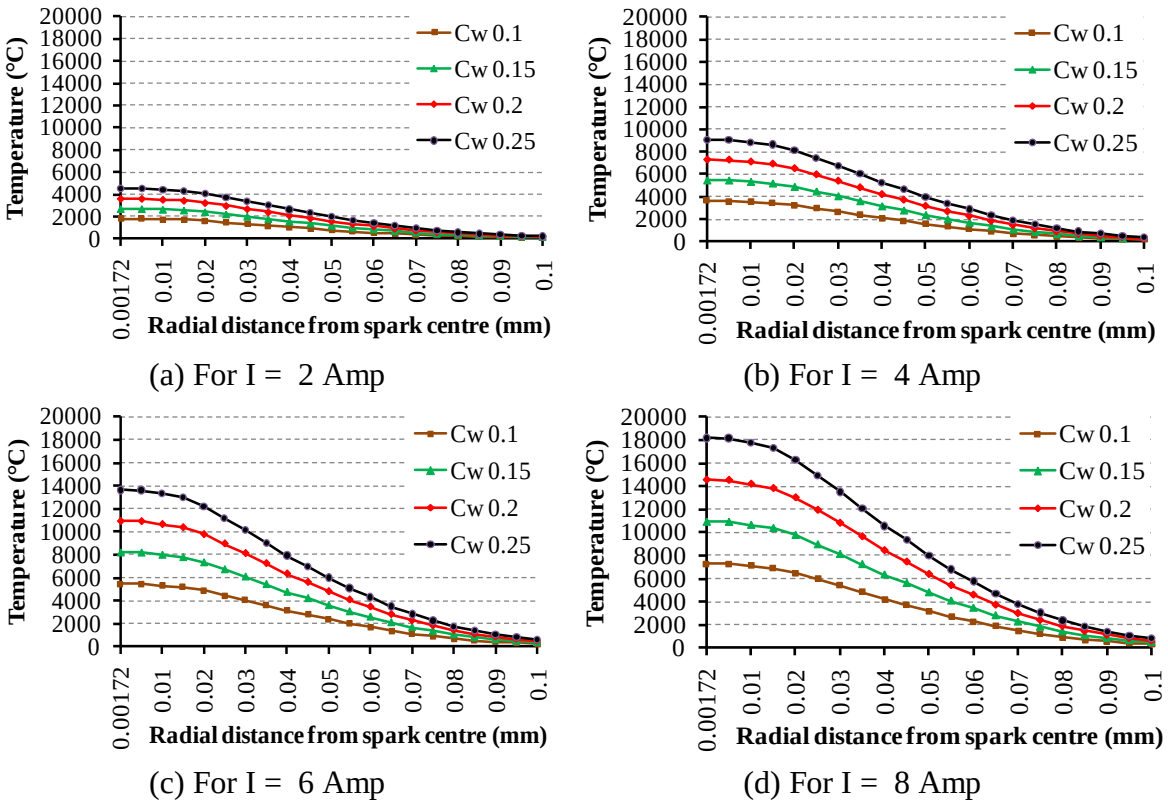

Figure 4.6: Temperature distribution in radial direction generated during simulation using K_p = 2.4, V_d = 35 Volt, T_{on} 100 µs for different C_w at different current settings (a) 2 Amp, (b) 4 Amp, (c) 6 Amp and (d) 8 Amp

3-D colored contour plots images have been taken for few cases of pulse on time 100 µs as shown in Figure 4.7 (a), (b), (c) and (d). Input parameters for these particular cases are pulse on time 100 µs, C_w 0.2, K_p 2.4, V_d 35 Volt and current = 2, 4, 6 and 8 Amp respectively for four different simulations. Red region shown in Figure 4.7 (a) to (d) represent material above 1426 °C i.e. melting point of H11 and this region is the predicted volume to be removed while actual machining. Comparing Figure 4.3, 4.5 and 4.7, it is clarified that diameter of the predicted melting zone (red region) increases by increasing pulse on time and discharge current. So it shows that pulse timing and discharge current have considerable effect on the diameter of the melting zone.

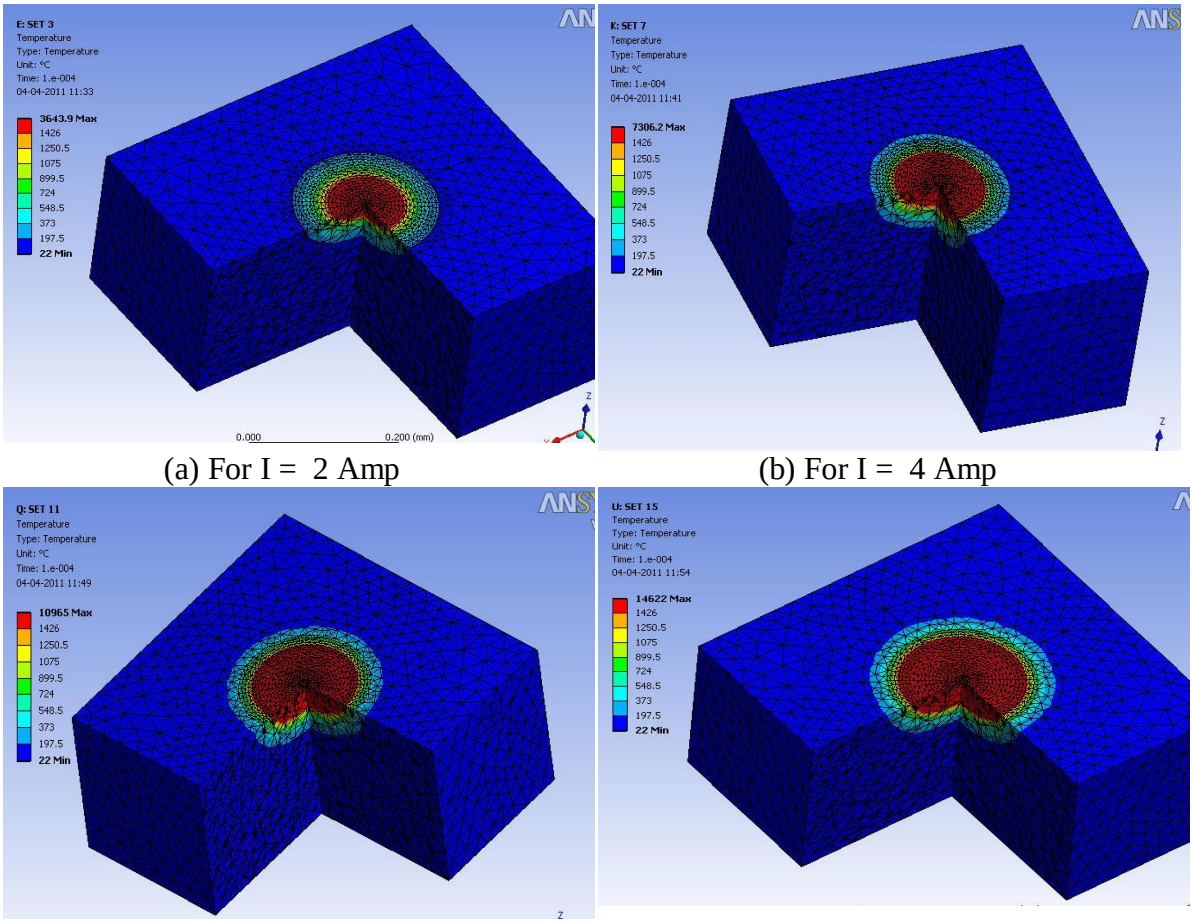

(a) For I = 2 Amp (b) For I = 4 Amp

(c) For I = 6 Amp (d) For I = 8 Amp

Figure 4.7: Temperature distribution with K_p = 2.4, V_d = 35 Volt, pulse on 100 µs, C_w = 0.2 and current = 2, 4, 6, 8 Amp respectively

Figure 4.2, 4.4 and 4.6 describe the effect of varying discharge current on the temperature distribution for different pulse on time that is 50, 75 and 100 µs.

To observe temperature distribution into work material in depth direction simulation results have been plotted as shown in Figure 4.8. Input parameters for these particular cases are pulse on time 100 µs, C_w 0.2, K_p 2.4, V_d 35 Volt and current = 2, 4, 6 and 8 Amp and pulse on time 50 µs , 75 µs, 100 µs respectively for three different simulations. From Figure 4.8 a), b) and c) it is clearly visible that temperature falls suddenly in depth direction and melting zone (i.e. temperature >= 1426 ºC) lies between z = 0 to 0.040 mm for all set of simulations.

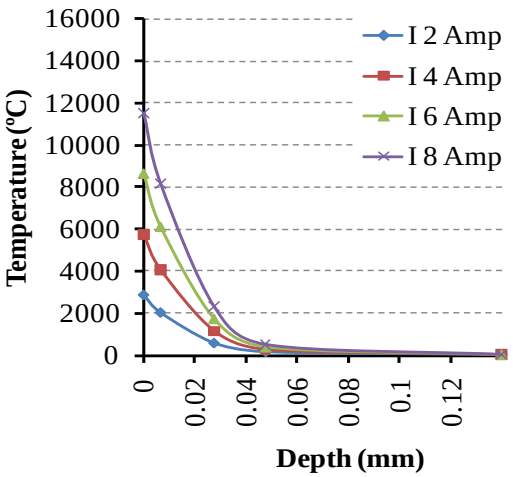

a) T_{on} 50 µs

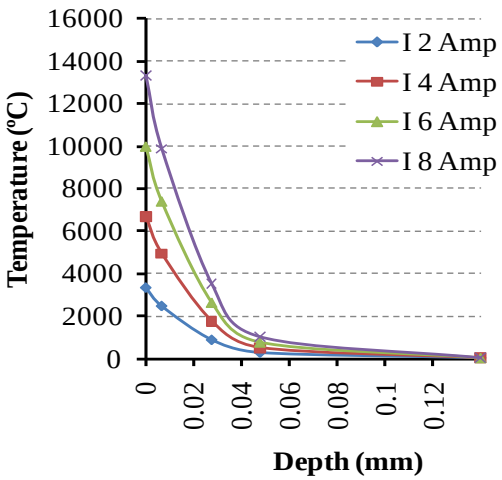

b) T_{on} 75 µs

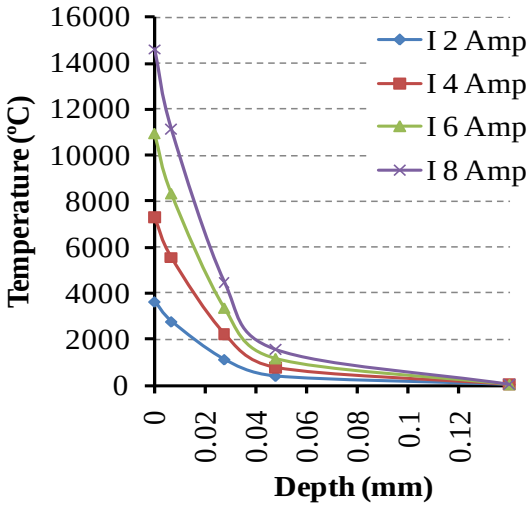

c) T_{on} 100 µs

Figure 4.8: Temperature distribution in depth direction generated during simulation using K_p = 2.4, V_d = 35 Volt, T_{on} 100 µs for different current and C_w at different T_{on} settings (a) 50 µs, (b) 75 µs, (c) 100 µs.

Comparing Figure 4.6 and 4.8 it is observed that rate of decreasing temperature is large in depth direction compared to the radial direction. From above discussion it is clear that depth of the crater is predicted to be less compared to radius of crater. It is also inferred that peak temperature increases with increase in current and pulse on time.

To observe the effect of C_w on the temperature distribution simulations have been made with four different values of C_w as shown in Figure 4.9 (a), (b), (c) and (d). In present work constant pulse on time 50 µs, current = 2, 4, 6, 8 Amp, V_d 35 Volt, K_p 2.4 is taken for each simulation. Only C_w is used with four different values for different simulations to observe its effect on temperature distribution. It is clearly visible from the Figure 4.9 (a),

(b), (c) and (d) that peak temperature increases with increase in C_w factor. Temperature distribution at the center of spark is maximum and decreases in radial direction following Gaussian distribution.

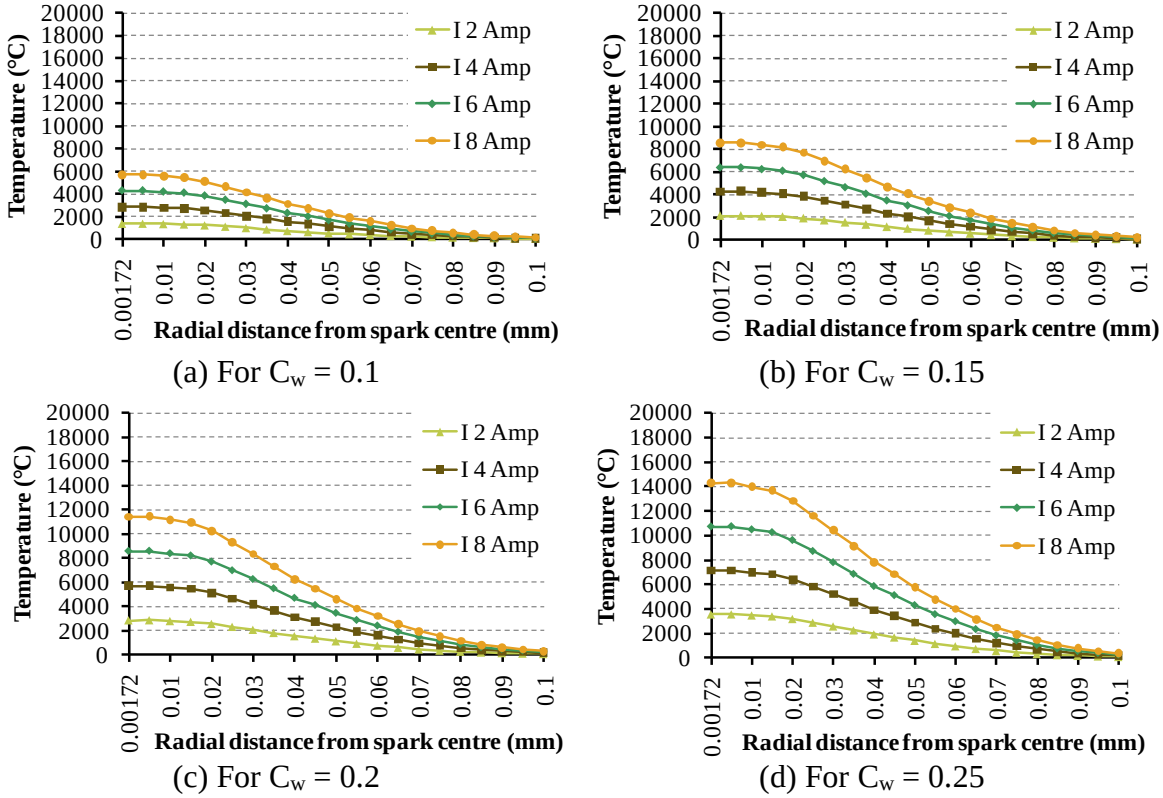

(a) For C_w = 0.1

(b) For C_w = 0.15

(c) For C_w = 0.2

(d) For C_w = 0.25

Figure 4.9: Temperature distribution in radial direction generated during simulation using K_p = 2.4, V_d = 35 Volt, T_{on} = 50 µs for different current at different C_w settings (a) 0.1, (b) 0.15, (c) 0.2 and (d) 0.25

Further again to study the effect of C_w on temperature distribution for the pulse on time 75 µs, simulation results have been presented in Figure 4.10 (a), (b), (c) and (d). Input parameters for the present case are constant pulse on time 75 µs, current = 2, 4, 6, 8 Amp, V_d 35 Volt, K_p 2.4 for each simulation and four different values of C_w = 0.1, 0.15, 0.2 and 0.25 respectively for four different simulations. It is clearly visible from the Figure 4.10 (a), (b), (c) and (d) that peak temperature increases with increase in C_w factor. Temperature distribution at the center of spark is maximum and decreases in radial direction following Gaussian distribution. From the Figure 4.10 (a) and 4.10 (b) it is observed that peak temperature attained with C_w 0.2 is nearly double than the temperature attained with C_w 0.1. Comparing Figure 4.9 (d) and 4.10 (c) it is observed that peak temperature attained for each value of current are nearly same for the setting pulse on 50 µs, C_w 0.25 and pulse on 75 µs, C_w 0.2.

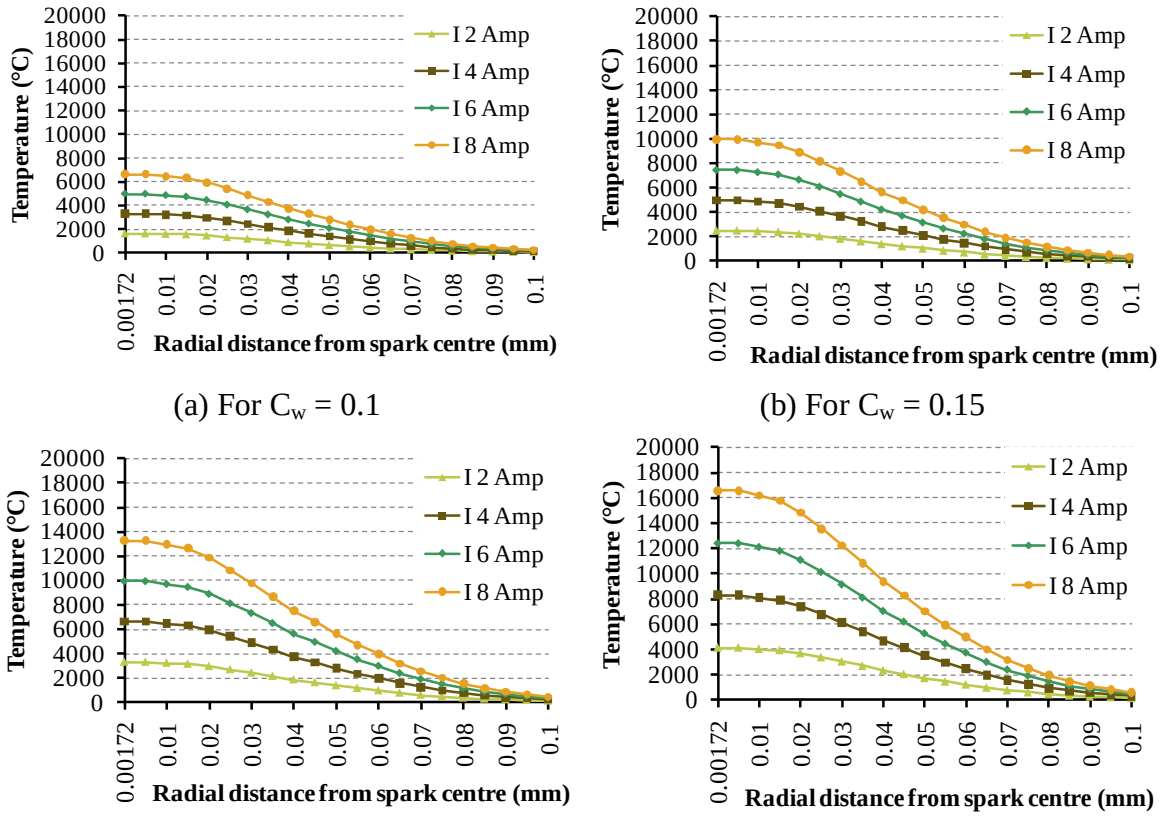

(a) For C_w = 0.1

(b) For C_w = 0.15

(c) For C_w = 0.2

(d) For C_w = 0.25

Figure 4.10: Temperature distribution in radial direction generated during simulation using K_p = 2.4, V_d = 35 Volt, T_{on} = 75 µs for different current at different C_w settings (a) 0.1, (b) 0.15, (c) 0.2 and (d) 0.25

To study the effect of C_w during pulse on 100 µs analysis results have been plotted as shown in Figure 4.11 (a), (b), (c) and (d). Pulse on time 100 µs, current = 2, 4, 6, 8 Amp, V_d 35 Volt, K_p 2.4 for each simulation and four different values of C_w = 0.1, 0.15, 0.2 and 0.25 respectively for four different simulations are used as input parameters. From the Figure 4.11 (a) to (d) it is observed that peak temperature increases with increase in C_w factor and temperature distribution at the center of spark is maximum and decreases in radial direction following Gaussian distribution. It is inferred from the Figure 4.11 (a) and 4.11 (c) that peak temperature attained with C_w 0.2 is nearly double than the temperature attained with C_w 0.1. Comparing Figure 4.9 (d) and 4.11 (c) it is observed that peak temperature attained for each value of current are exactly same for the setting pulse on 50 µs, C_w 0.25 and pulse on 100 µs, C_w 0.2.

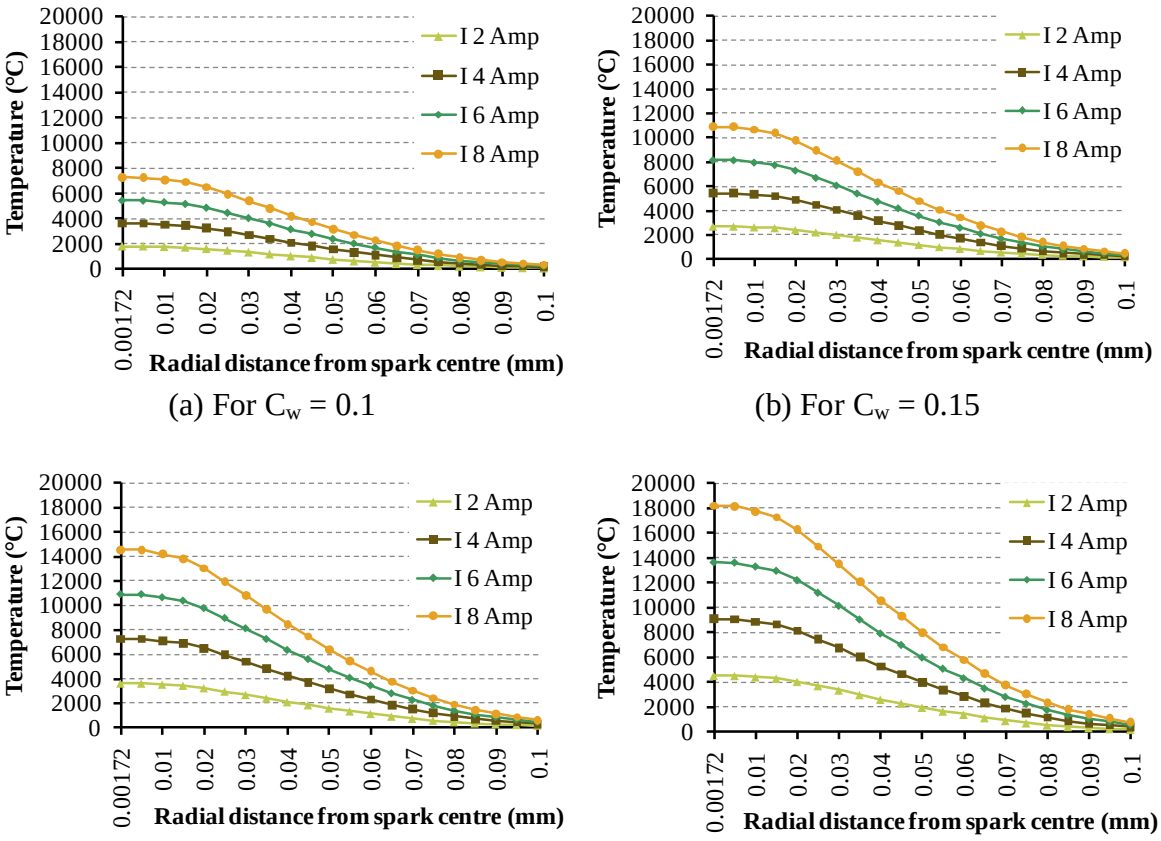

(a) For C_w = 0.1 (b) For C_w = 0.15

(c) For C_w = 0.2 (d) For C_w = 0.25

Figure 4.11: Temperature distribution in radial direction generated during simulation using K_p = 2.4, V_d = 35 Volt, T_{on} = 100 µs for different current at different C_w settings (a) 0.1, (b) 0.15, (c) 0.2 and (d) 0.25

4.1.2 Volume removed

Based on the results given by the transient thermal analysis in temperature distribution form crater volume to be removed has been predicted. For this purpose temperature distribution results has been exported into the excel file and sorted there. Radius of the crater is noted down by sorting the nodes on the top surface of the workpiece and making y = zero. Coordinate where the temperature falls below the 1426 °C (melting temperature of H11) is the radius of the crater. Similarly depth of the crater has been estimated while moving in depth direction and making x and y both nearly zero. So assuming the crater is a part of a sphere and using radius and depth of the crater calculation is done for volume removed by a single spark as follows:

$$V_c = \frac{\pi}{6} h_c (3a^2 + h_c^2) \qquad \text{Equation (4.1)}$$

Where

a = crater radius, V_c = crater volume and h_c = crater depth.

Images for the volume removed in the 3-D contour form are captured for each simulation. Three sample cases for pulse on time 50, 75 and 100 µs has been shown in Figures 4.12, 4.13 and 4.14. As shown in Figure 4.12 (a) crater surface and its shape to be produced is predicted and in Figure 4.12 (b) removed volume in the form of crater is shown separated from the work material. Input parameters used in simulation shown in Figure 4.12 are pulse on 50 µs, K_p 2.4, V_d 35 Volt, current 6 Amp and C_w 0.25. Crater radius in this simulation is 0.075 mm, depth 0.03058 mm and volume removed is 0.000285 mm^3. Similarly volume removed during pulse on 75 µs using input parameters K_p 2.4, V_d 35 Volt, current 4 Amp and C_w 0.2 has been shown in Figure 4.13. Crater radius in this simulation is 0.067 mm, depth 0.0275 mm and volume removed is 0.000205 mm^3. Another simulation done using input parameters pulse on 100 µs, K_p 2.4, V_d 35 Volt, current 6 Amp and C_w 0.2 is shown in Figure 4.14. Crater radius in this simulation is 0.0842 mm, depth 0.04768 mm and volume removed is 0.000431 mm^3. Comparing Figure 4.12 and 4.14 it is clearly understood that volume removed increases with increase in pulse on time and diameter and depth of the crater produced during pulse on 100 µs pulse on time is significantly larger than produced during pulse on 50 µs.

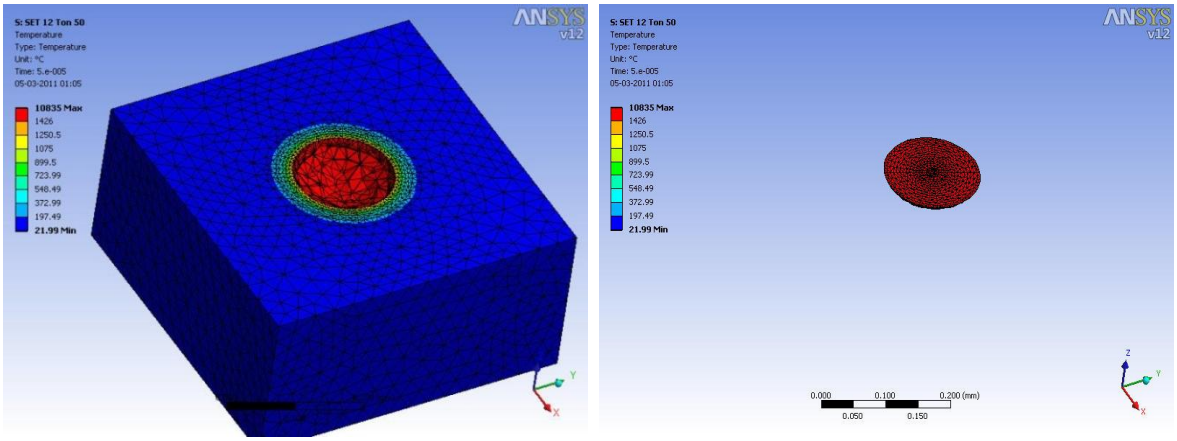

(a) crater shape (b) removed crater volume

Figure 4.12: Predicted crater shape and removed volume separated from the work material during simulation using K_p = 2.4, I = 6 Amp, V_d = 35 Volt and C_w = 0.25, pulse on 50 µs

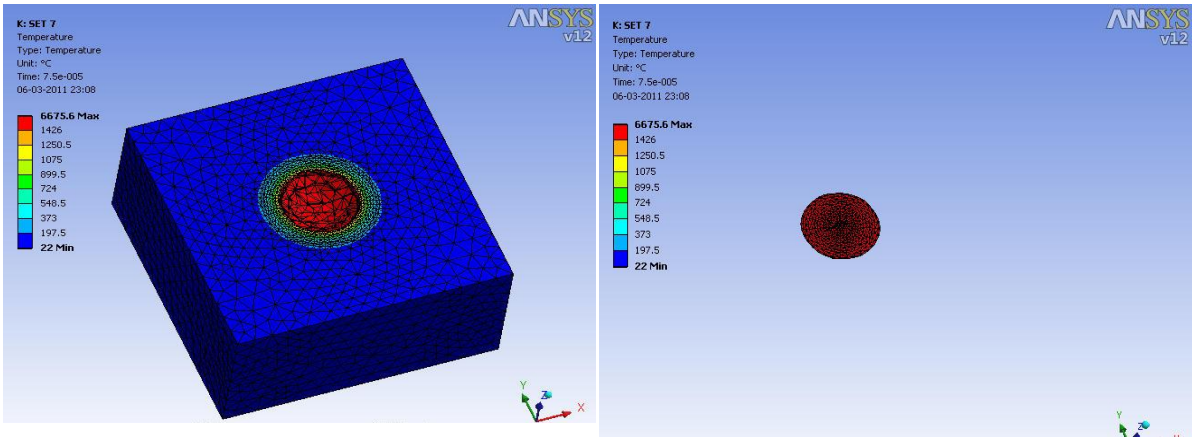

(a) crater shape (b) removed crater volume

Figure 4.13 Predicted crater shape and removed volume separated from the work material during simulation using K_p = 2.4, Current = 4 Amp, V_d = 35 Volt and C_w = 0.2, pulse on 75 µs

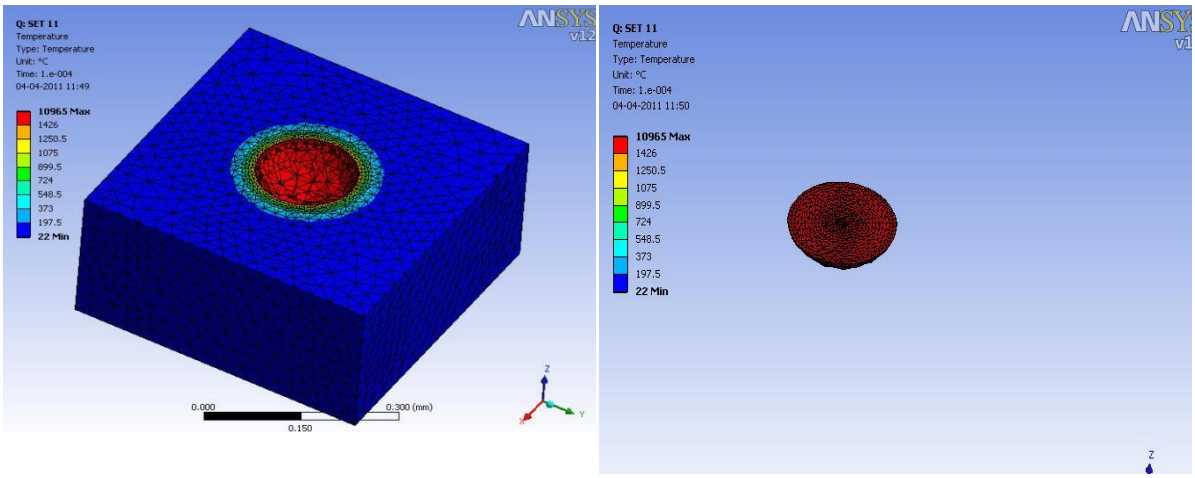

(a) crater shape (b) removed crater volume

Figure 4.14: Predicted crater shape and removed volume separated from the work material during simulation using K_p = 2.4, Current = 6 Amp, V_d = 35 Volt and C_w = 0.2, pulse on 100 µs

Results for volume removed calculated using equation 4.1 for different simulations have been plotted as shown in Figure 4.15 (a), (b) and (c). Figure 4.15 (a) gives the volume removed with respect to varying current and C_w factor. Input parameters for simulations presented in Figure 4.15 (a) are pulse on 50 µs, K_p 2.4, V_d 35 Volt, current = 2, 4, 6, 8 Amp and C_w = 0.1, 0.15, 0.2, 0.25. It is visible from the Figure 4.15 (a) that volume removed increases with increasing current and C_w factor which will result in high material removal rate (MRR) and lower surface finish. To study the volume removed during pulse on time 75 µs different simulations have been done using constant pulse on time 75 µs and varying current and C_w factors. Figure 4.15 (b) gives the volume removed with input parameters pulse on 75 µs, K_p 2.4, V_d 35 Volt, current = 2, 4, 6, 8 Amp and C_w = 0.1,

0.15, 0.2, 0.25. Again to observe volume removal during pulse on 100 µs different simulations have been executed. Variable varied in these simulations are current and C_w factor. Figure 4.15 (c) shows the result of simulation executed using input parameters pulse on 100 µs, K_p 2.4, V_d 35 Volt, current = 2, 4, 6, 8 Amp and C_w = 0.1, 0.15, 0.2, 0.25.

Comparing Figure 4.15 (a), (b) and (c), it is clearly visible that increasing pulse on time increase removed crater volume which will result in high MRR (material removal rate). At the same time due to large size of craters formed on the surface, surface finish will be less for high pulse on timings. From the Figure 4.15 (a) and 4.15 (c), it is inferred that volume removed during pulse on time 100 µs is nearly double than volume removed during pulse on 50 µs.

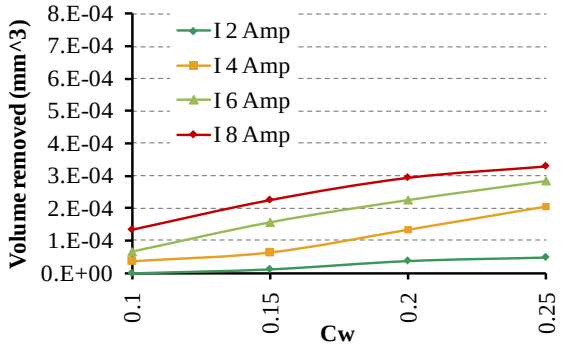

(a) For T_{on} = 50 µs

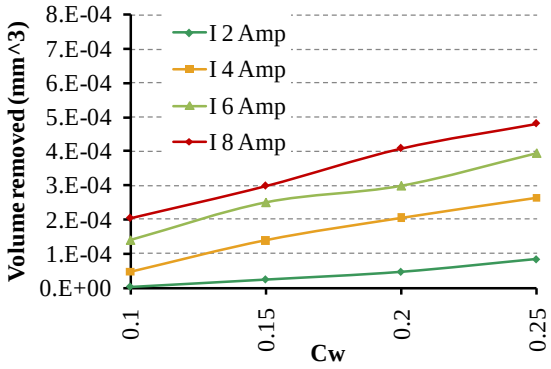

(b) For T_{on} = 75 µs

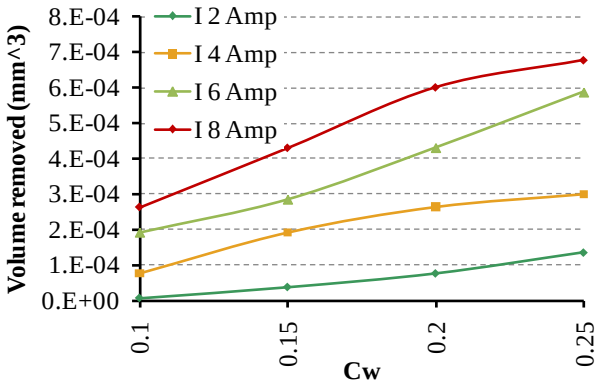

(c) For T_{on} = 100 µs

Figure 4.15: Volume removed in mm^3 during simulation using K_p = 2.4, V_d = 35 Volt, for different current and C_w at different pulse on setting (a) T_{on} = 50, (b) T_{on} = 75, (c) T_{on} = 100 µs respectively.

4.1.3 Different Temperature Zones of heated workpiece

During PMEDM process machining of the material occurs due to melting as well as evaporation. So it is important to study the material above melting temperature of H11 that is 1426 °C. The region under spark has been divided in four different temperature ranges which are as follows:

1. Unaffected zone : simulated temperature ≤ 958 °C
2. Heat affected zone : 958 °C ≤ simulated temperature ≤ 1426 °C
3. Melting zone : 1426°C ≤ simulated temperature ≤ 2986 °C
4. Boiling and Evaporation zone : simulated temperature > 2986 °C

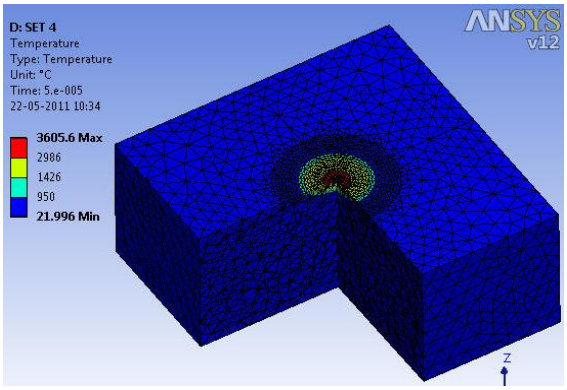

(a) For current = 2 Amp and C_w = 0.25

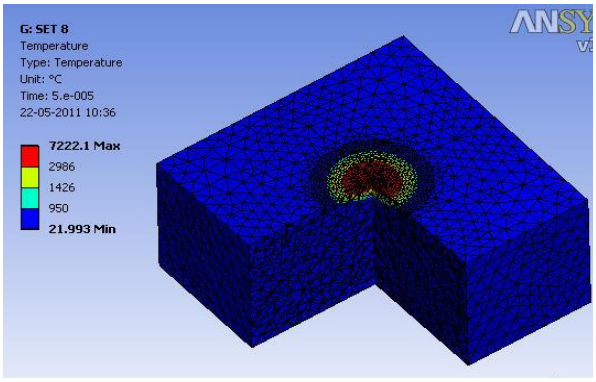

(b) For current = 4 Amp and C_w = 0.25

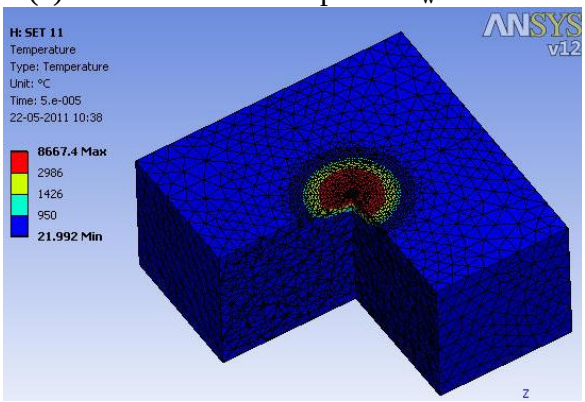

(c) For current = 6 Amp and C_w = 0.2

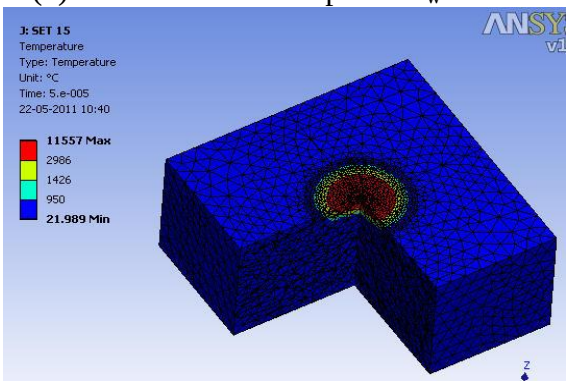

(d) For current = 8 Amp and C_w = 0.2

Figure 4.16: Heated work material at different temperature zones with input parameters pulse on 50 µs, K_p = 2.4, V_d = 35 Volt, at different current and C_w settings.

Figure 4.16 (a), (b), (c) and (d) shows heated work material at different temperature zones with constant input parameters pulse on 50 µs, K_p = 2.4, V_d = 35 Volt, varying C_w and discharge current = 2, 4, 6 and 8 respectively for four different simulations. Figure 4.16 (a) gives information of different temperature zones generated during simulation using

discharge current 2 Amp and C_w 0.25. Discharge current = 4 Amp and C_w 0.25 is used in simulation presented in Figure 4.16 (b). It is observed that evaporation zone proportionate to melting zone is quite larger in Figure 4.16 (b) than in Figure 4.16 (a). While actual machining some of the material in melting zone just after pulse off starts, cool down and deposit on to the crater surface. But the material in the evaporation zone can't solidify and deposit again on to crater surface. So MRR (material removal rate) will be high in the large evaporation zones. Comparing Figure 4.16 (a), (b), (c) and (d) it is clear that at high discharge current evaporation proportionate to melting is quite large which will increase material removal rate and material flushing efficiency.

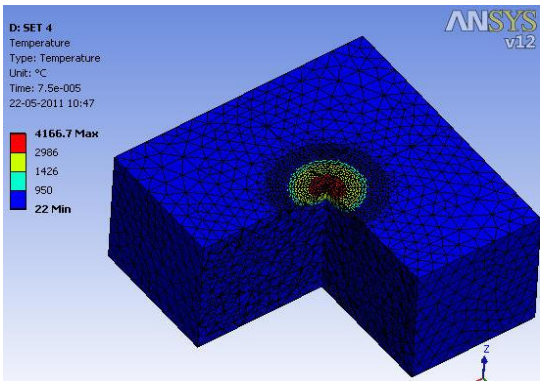

(a) For current = 2 Amp and C_w = 0.25

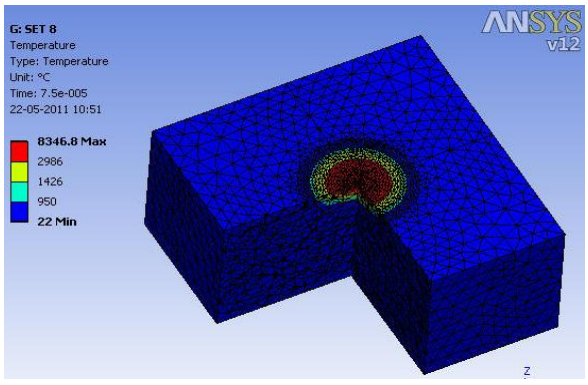

(b) For current = 4 Amp and C_w = 0.25

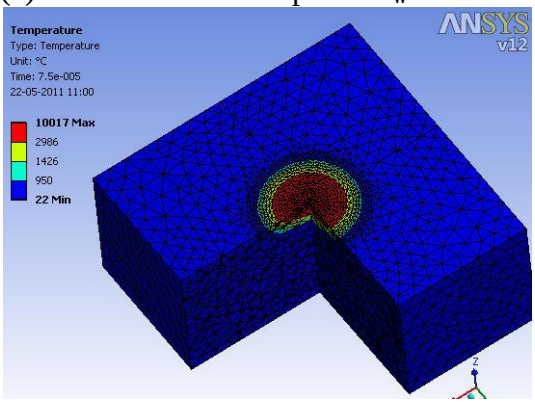

(c) For current = 6 Amp and C_w = 0.2

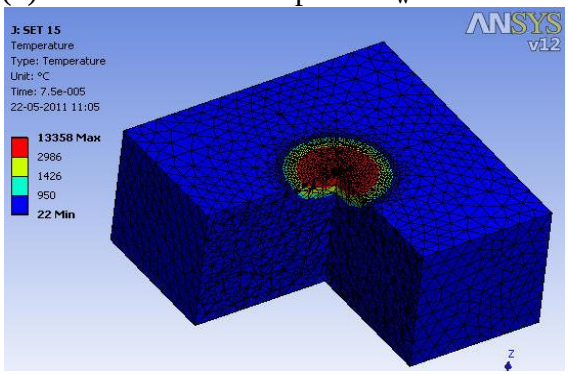

(d) For current = 8 Amp and C_w = 0.2

Figure 4.17: Heated work material at different temperature zones with input parameters pulse on 75 µs, K_p = 2.4, V_d = 35 Volt, at different current and C_w settings.

To analyze the material at different temperature zone during pulse on 75 µs, simulation have been done using constant input parameters pulse on 75 µs, K_p = 2.4, V_d = 35 Volt, varying C_w and discharge current = 2, 4, 6 and 8 respectively for four different simulations shown in Figure 4.17. It is observed that in Figure 4.17 (b) evaporation zone is quite larger proportionate to melting zone than in Figure 4.17 (a). Material in evaporative zone can't deposit on the crater surface again which is possible in melting zone. So it is

concludes that removal of material will be larger in case of high discharge currents due to better material flushing efficiency. Comparing Figure 4.17 (a) to (d) it is also observed that there is no considerable effect of discharge current on the recrystalization zone. Still a small variation in recrystalization zone can be seen comparing Figure 4.17 (a) and Figure 4.17 (d).

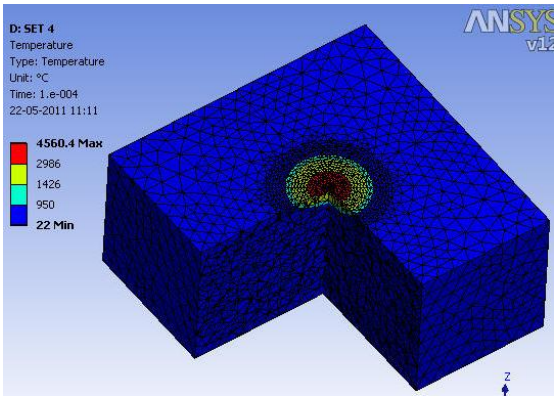

(a) For current = 2 Amp and C_w = 0.25

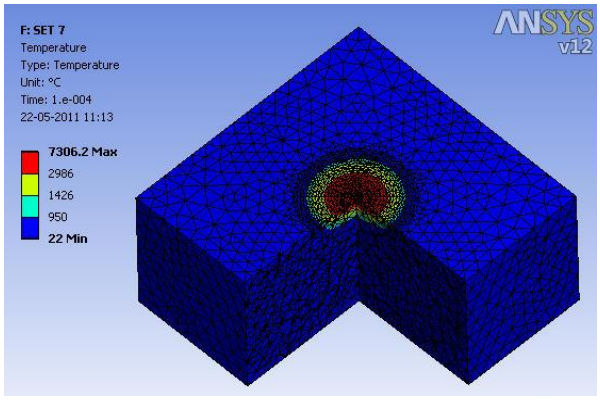

(b) For current = 4 Amp and C_w = 0.2

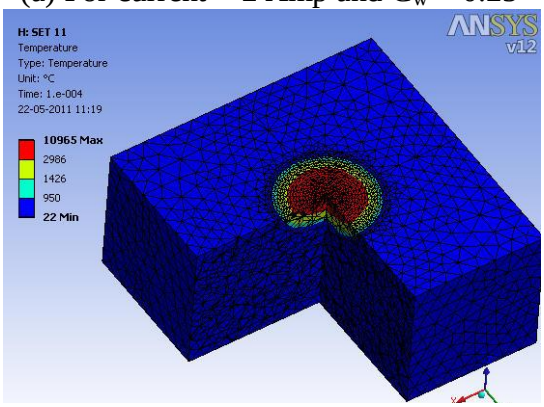

(c) For current = 6 Amp and C_w = 0.2

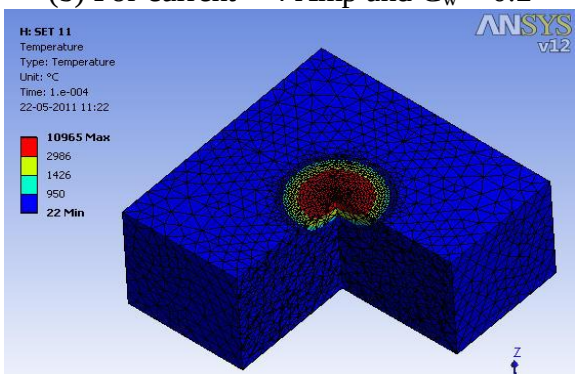

(d) For current = 8 Amp and C_w = 0.15

Figure 4.18: Heated work material at different temperature zones with input parameters pulse on 100 µs, K_p = 2.4, V_d = 35 Volt, at different current and C_w settings.

Different temperature zone of the heated work domain during pulse on 100 µs are shown in Figure 4.18 (a), (b), (c) and (d). Simulations presented in Figure 4.18 (a) to (d) use constant input parameters pulse on 100 µs, K_p = 2.4, V_d = 35 Volt, varying C_w and discharge current = 2, 4, 6 and 8 respectively for four different simulations. It is observed that in Figure 4.18 (b) evaporation zone is quite larger proportionate to melting zone than in Figure 4.18 (a). Comparing Figure 4.18 (a), (b), (c) and (d) it is concluded that material flushing efficiency and MRR increase with increasing discharge current.

4.1.4 Cooling Rate of the Work Material

In PMEDM process one complete machining cycle time is pulse on + pulse off. During the pulse on time discharge current increases upto peak current and heat flux is active on the spark region during this period; after this pulse off occurs. During pulse off spark channel collapse and debris are flushed out with the help of dielectric flushing. Temperature of the work material declines because there is no heat flux active on spark region during pulse off. At the same time cooling of the work material occurs beyond the spark region during pulse on and pulse off because of convection between work material and dielectric fluid. Surface properties and microstructure of the material also varies with respect to cooling rate of the work material. So it is very important to predict the cooling rate of the work material. Cooling rate of work material has been predicted for various input parameters; i.e. current, pulse on, pulse off and C_w as shown in Figure 4.19, 4.20 and 4.21.

To study the effect of pulse on time, pulse off time, discharge current and C_w on cooling rate these four parameters have been varied in different combination to execute different set of simulations. Four different levels of currents i.e. 2, 4, 6 and 8 Amp have been used to take into effect of discharge current. Pulse on has been used in three different levels i.e. 50, 75 and 100 µs. Pulse off has been used in three different values i.e. 25, 50 and 75 µs. C_w (fraction of total supplied heat transferred to workpiece) is taken in four levels i.e. C_w = 0.1, 0.15, 0.2 and 0.25. As shown in Figure 4.19 cooling rate has been predicted for the pulse on time 50 µs, K_p 2.4, V_d 35 Volt, C_w = 0.1, 0.15, 0.2, 0.25, pulse off = 25, 50, 75 µs, current = 2, 4, 6 and 8 Amp respectively for four different cases. From Figure 4.19 (a), (b), (c) and (d) it is observed that cooling rate increase for the short pulse off timings. It is also observed that increasing discharge current and C_w factor also increase the cooling rate. Microstructure and surface properties are significantly affected by cooling rate. For higher cooling rates surface quality will be poor and material will be more prone to crack generation. Large cooling rate will also affect the material in the melting zone to resolidify and deposit on the crater surface by extracting heat from the melting zone. Due to this deposition of material MRR will reduce.

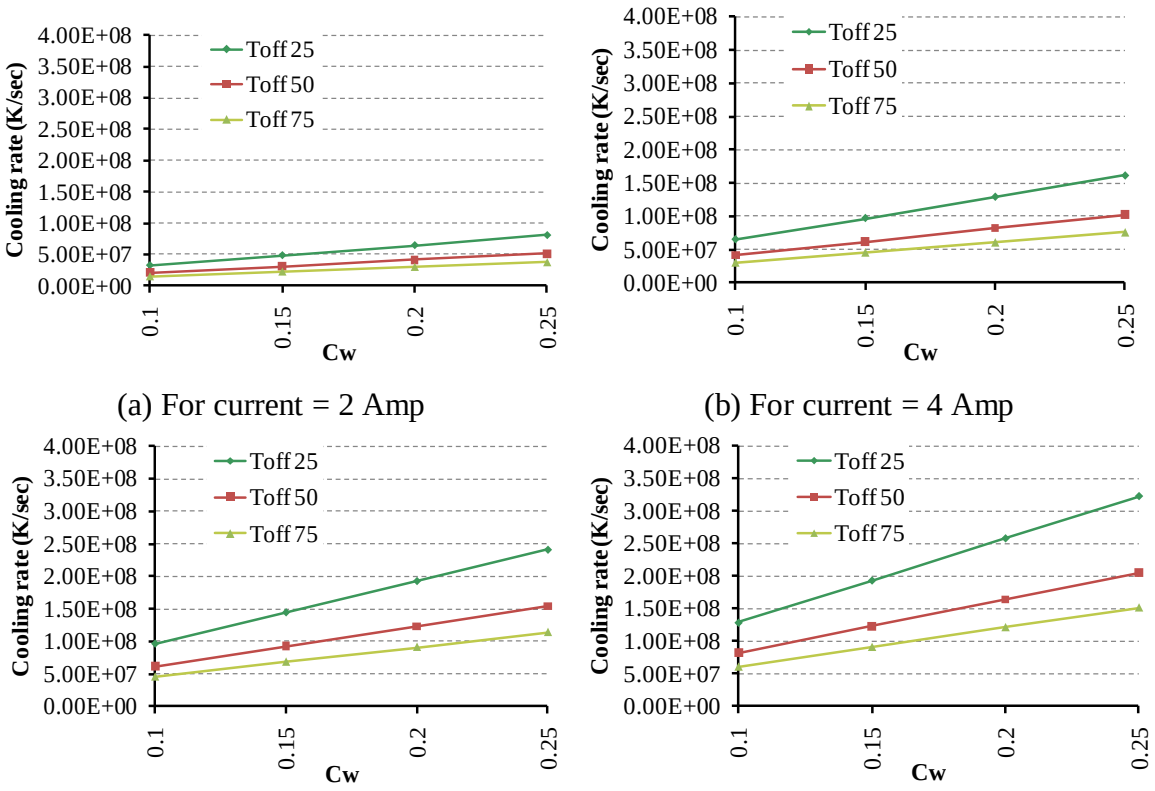

(a) For current = 2 Amp

(b) For current = 4 Amp

(c) For current = 6 Amp

(d) For current = 8 Amp

Figure 4.19: Predicted cooling rate of work material during simulation using T_{on} 50 µs, for different pulse off and C_w at different current settings (a) 2 Amp, (b) 4 Amp, (c) 6 Amp and (d) 8 Amp

Further to assess the cooling rate of the work material during pulse on time 75 µs different simulation have been done using constant pulse on time 75 µs and varying current, C_w, and pulse off timings. Figure 4.20 (a), (b), (c) and (d) gives the results of predicted cooling rate during simulation with input parameters pulse on 75 µs, K_p 2.4, V_d 35 Volt, pulse off = 25, 50, 75 µs, C_w = 0.1, 0.15, 0.2, 0.25 and current = 2, 4, 6, 8 Amp respectively for four different cases. Again it is confirmed that cooling rate increases with short pulse off timings and increasing current and C_w factor. Comparing Figure 4.19 and 4.20 it is understood that there is no effect of pulse on time ranging from 50 to 75 µs, on the cooling rate. So for pulse on time 50 to 75 µs, it is concluded that cooling rate of the material is not affected by the peak temperature generated into the work material at the end of the pulse on.

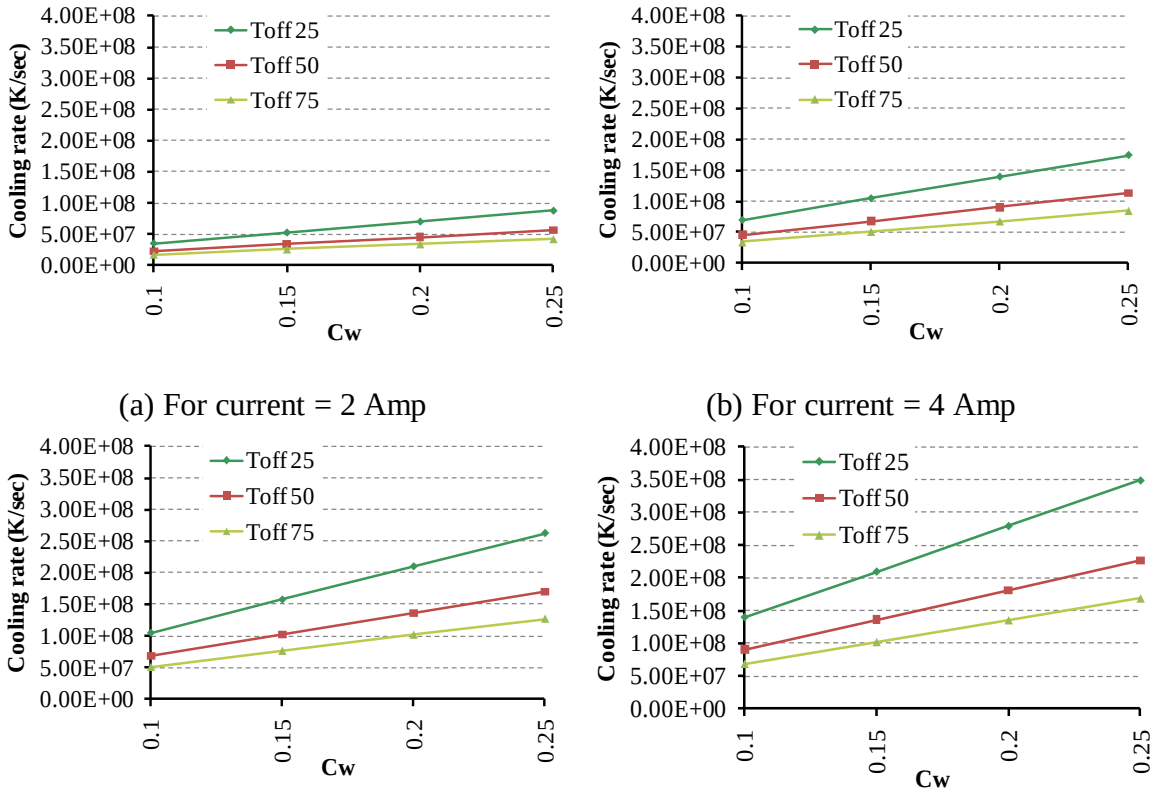

(a) For current = 2 Amp

(b) For current = 4 Amp

(c) For current = 6 Amp

(d) For current = 8 Amp

Figure 4.20: Predicted cooling rate of work material after simulation using T_{on} 75 µs, for different pulse off at different current settings (a) 2 Amp, (b) 4 Amp, (c) 6 Amp and (d) 8 Amp

Predicted cooling rate of the work material during pulse on time 100 µs is shown in Figure 4.21. input parameters used in the simulation presented in Figure 4.21 are pulse on 100 µs, K_p 2.4, V_d 35 Volt, pulse off = 25, 50, 75 µs, C_w = 0.1, 0.15, 0.2, 0.25 and current = 2, 4, 6, 8 Amp respectively for four different cases. It is confirmed that cooling rate increases with short pulse off timings and increasing current and C_w factor. Comparing Figure 4.19, 4.20 and 4.21 it is observed that there is very less effect of pulse on timing on cooling rate while focusing on results of simulations with pulse on 50and 75 µs. But at the same time it is observed that there is considerable variation in the cooling rate when results of simulations with pulse on time 50 and 100 µs are compared.

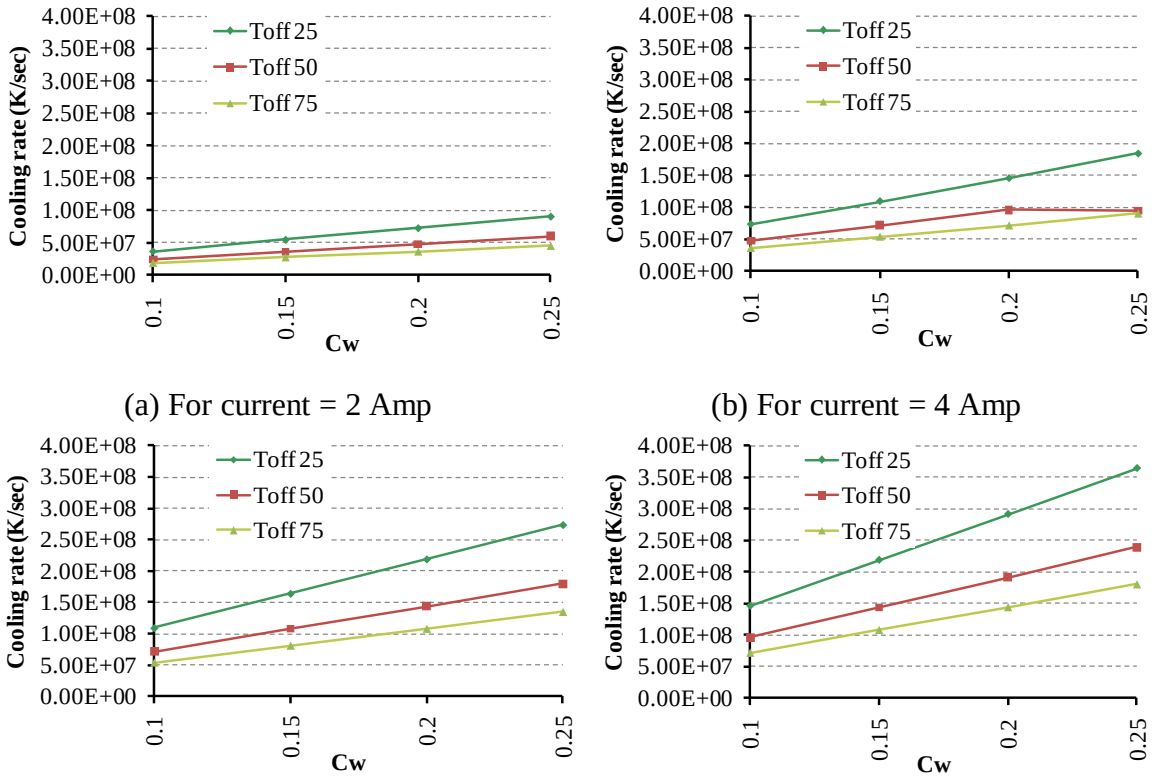

(a) For current = 2 Amp

(b) For current = 4 Amp

(c) For current = 6 Amp

(d) For current = 8 Amp

Figure 4.21: Predicted cooling rate of work material during simulation using T_{on} 100 µs, for different pulse off and C_w at different current settings (a) 2 Amp, (b) 4 Amp, (c) 6 Amp and (d) 8 Amp

4.1.5 Stresses Induced into Work Material

In PMEDM process while machining very high temperatures are generated at the spark location. Due to these elevated temperatures; material evaporates in that particular region or melt and flushed out in the form of debris by the dielectric flushing. At the same time material below the spark region tries to expand because of high temperatures but restricted by the surrounding material. Because of this sufficient amount of stresses setup there in remaining work material near to crater surface which may result in generation of the cracks in work material.

To predict stresses setup into work material different simulations are done for constant pulse on time 75 µs and 100 µs. Figure 4.22 (a) gives the Equivalent von-Mises stresses near to crater surface generated through the simulations using input parameters pulse on 75 µs, K_p 2.4, V_d 35 Volt, current 6 and 8 Amp, C_w = 0.1, 0.15, 0.2 and 0.25. Maximum stress setup during pulse on 75 µs are 6911 MPa and 4841 MPa with 8 and 6 Amp current respectively which are quite larger than the ultimate tensile strength of the material i.e.

1757 MPa. So it is predicted that chances of crack formation are there on the workpiece near the machined surface. It is observed that increasing current increases the stress values setup into the work material. Also for higher values of C_w stresses are high. High stresses near to crater surface leads to tendency of the material to fail. So from Figure 4.22 (a) it is concluded that for higher values of current and C_w strength of the material will be less near to the machined surface of the work material.

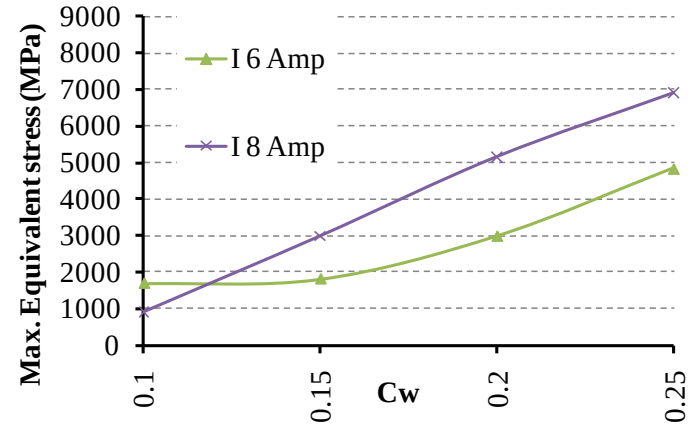

(a) For T_{on} = 75 µs

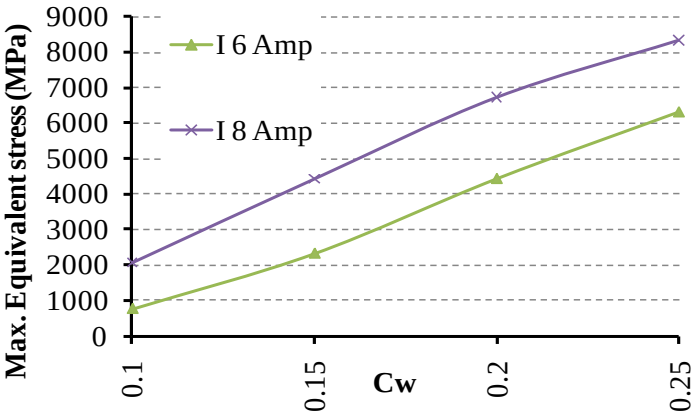

(b) For T_{on} = 100 µs

Figure 4.22: Equivalent von-Mises stresses generated near to crater surface during simulation with K_p = 2.4, V_d = 35 Volt, for different current and C_w at different T_{on} setting (a) 75 µs and (b) 100 µs

To estimate stresses setup into the work material during pulse on 100 µs another set of different simulations is done using input parameters pulse on 100 µs, K_p 2.4, V_d 35 Volt, current 6 and 8 Amp, C_w = 0.1, 0.15, 0.2 and 0.25. Results obtained from simulations using pulse on 100 µs are presented in the Figure 4.22 (b). Maximum stress setup during pulse on 100 µs are 8350 MPa and 6317 MPa with 8 and 6 Amp current respectively which are quite larger than the ultimate tensile strength of the material i.e. 1757 MPa. So

it is predicted that crack formation will be there on the workpiece near the machined surface. It is observed that increasing current increases the stress values setup into the work material. Also for higher values of C_w stresses are high. Comparing Figure 4.22 (a) and 4.22 (b) it is confirmed that increasing pulse on timings increase the stresses setup into the work material. Therefore it is predicted that materials machined with high pulse on timings will be more prone to failure near to surface.

Further to represent stresses setup near crater surface into the work material in form of 3-D colored contour plots images have been captured for each simulation. Few cases are shown in the Figure 4.23 and Figure 4.24. Figure 4.23 (a) to (d) represents the simulation results executed with pulse on time 75 µs, current 6 and 8 Amp, C_w 0.2 and 0.25, K_p 2.4, V_d 35 Volt. Peak stresses generated in simulations shown in Figure 4.23 (a), (b), (c) and (d) are 2988, 4841, 5159 and 6911 MPa respectively. Comparing Figure 4.23 (a) and Figure 4.23 (c) it is clear that stresses setup in the work material near crater surface increases with increase in the discharge current. From the Figure 4.23 (a) to (d) it is observed that increasing the discharge current and C_w stresses setup into the work material increases significantly. Stresses setup in simulation with current 8 Amp and C_w 0.25 are quite large than developed in simulation using current 2 Amp and C_w 0.2. So surface produced with larger current and high values of C_w are predicted to have less strength and more prone to failures.

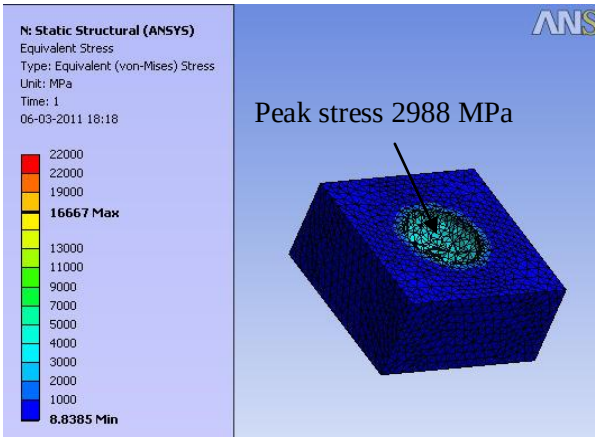

(a) For I = 6 Amp and C_w = 0.2

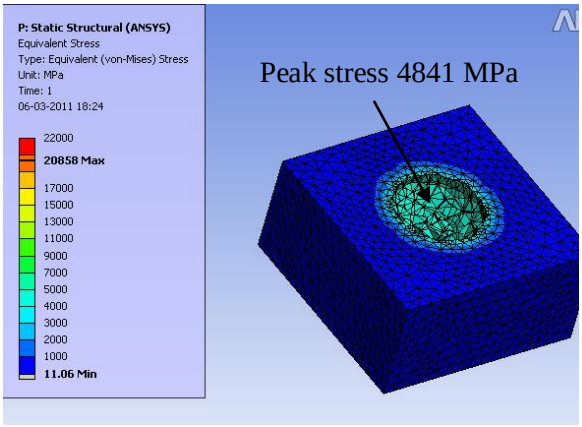

(b) For I = 6 Amp and C_w = 0.25

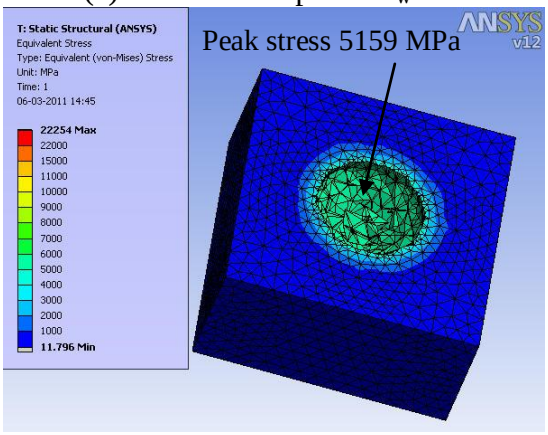

(c) For I = 8 Amp and C_w = 0.2

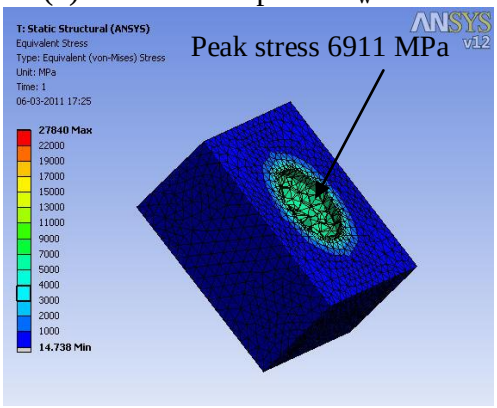

(d) For I = 8 Amp and C_w = 0.25

Figure 4.23: Maximum equivalent von-Mises stresses set up on the crater surface during simulation using input pulse on 75 µs, K_p = 2.4, V_d = 35 Volt for different current and C_w.

To observe the stresses setup during pulse on 100 µs simulations done with pulse on time 100 µs are represented in Figure 4.24 (a), (b), (c) and (d). Input parameters used in this simulation are pulse on time 100 µs, current 6 and 8 Amp, C_w 0.2 and 0.25, K_p 2.4, V_d 35 Volt. Peak stresses generated in simulations shown in Figure 4.24 (a) to (d) are 4431, 6317, 6734 and 8350 MPa respectively. Comparing Figure 4.24 (a), (b), (c) and (d) it is inferred that increase in the current and the C_w results in high value of stresses generated into the work material near to crater surface. Comparing Figure 4.23 and 4.24 it is predicted that with increase in pulse on time stresses setup into the work material will increase and material will more prone to failure near the surface due to low strength caused by high stresses setup into the material near surface.

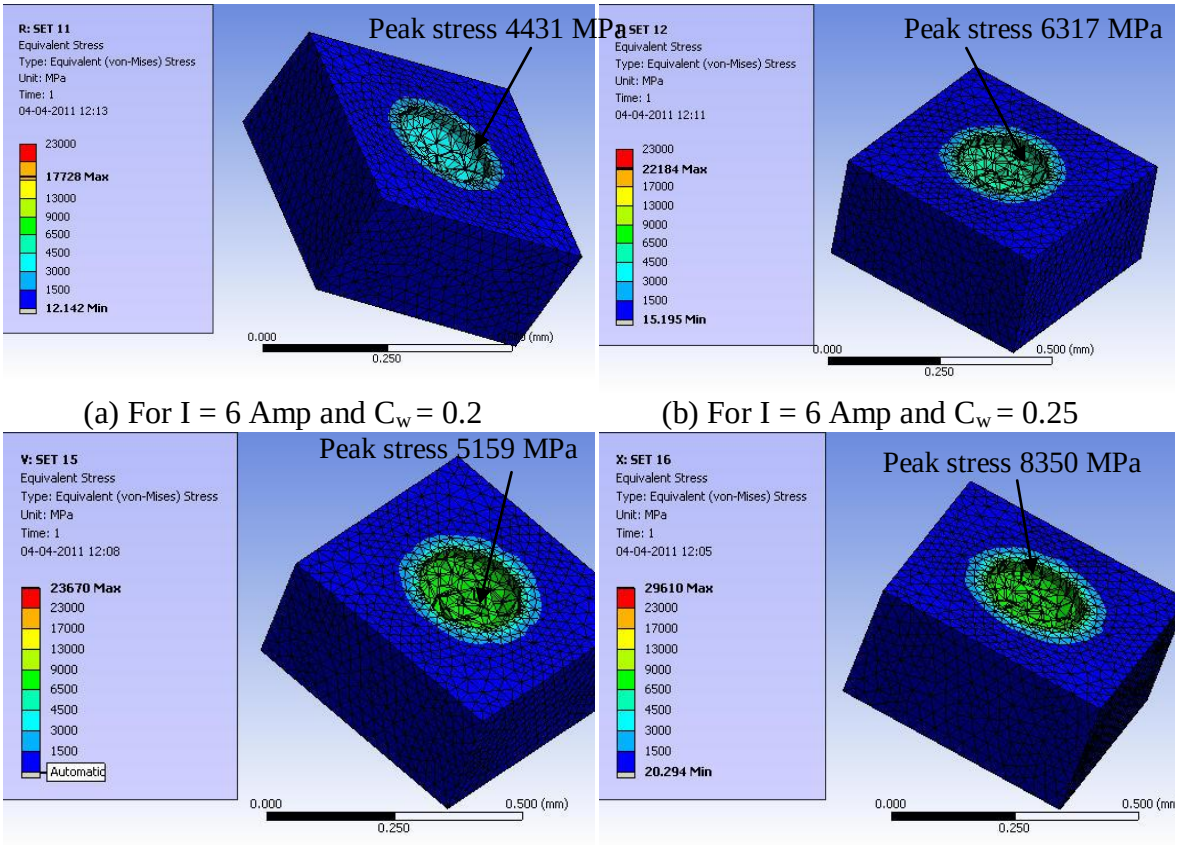

(a) For I = 6 Amp and $C_w = 0.2$ (b) For I = 6 Amp and $C_w = 0.25$

(c) For I = 8 Amp and $C_w = 0.2$ (d) For I = 8 Amp and $C_w = 0.25$

Figure 4.24: Maximum equivalent von-Mises stresses set up on the crater surface during simulation using input pulse on 100 µs, $K_p = 2.4$, $V_d = 35$ Volt for different current and C_w.

4.2 EXPERIMENTAL VALIDATION

4.2.1 Volume Removed

For the validation of the simulation results given for the volume removed experiments have been conducted on H11 material workpiece using copper electrode (20mm diameter), graphite powder (325 mesh size) mixed in kerosene dielectric at a concentration of 2gm/l.. Input parameters like current, pulse on, pulse off have been varied for different set of experiments.

Design of experiments has been given in Table 3.6. Diameter of craters has been measured using profile projector with accuracy of 1µm. The diameters of at least 10 different craters were measured and each crater was measured at least 5 times. The average of those was taken as the diameter of crater for volume calculation. Figures 4.25 and 4.26 show the view of craters on profile projector, formed in different set of experiments. Depth of craters has been measured using dial indicator with pointed tip and least count 1µm. Depth also measured on at least 10 different craters, and each depth

measured 5 times. Average of those values was taken as final depth of each crater to calculate volume using Equation 4.1.

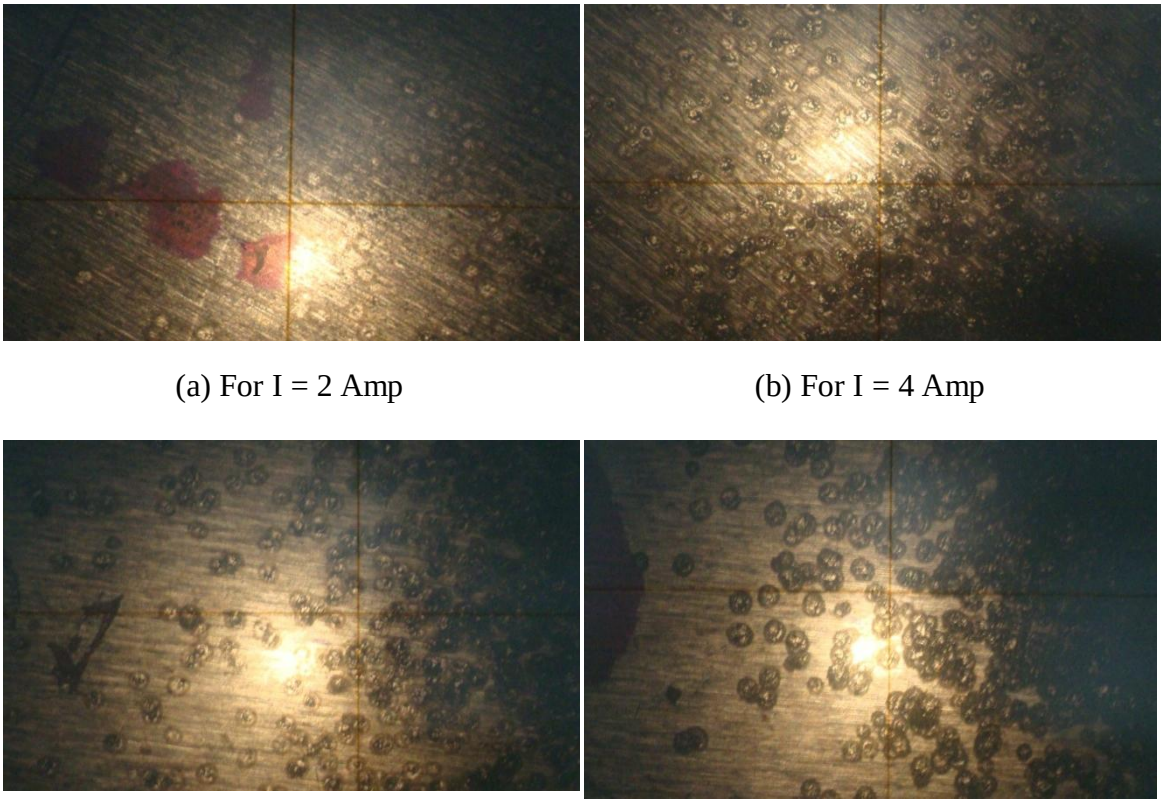

(a) For I = 2 Amp (b) For I = 4 Amp

(c) For I = 6 Amp (d) For I = 8 Amp

Figure 4.25 Craters formed during experiment using T_{on} 50 µs and T_{off} 50 µs at different current settings (a) 2 Amp, (b) 4 Amp, (c) 6 Amp and (d) 8 Amp

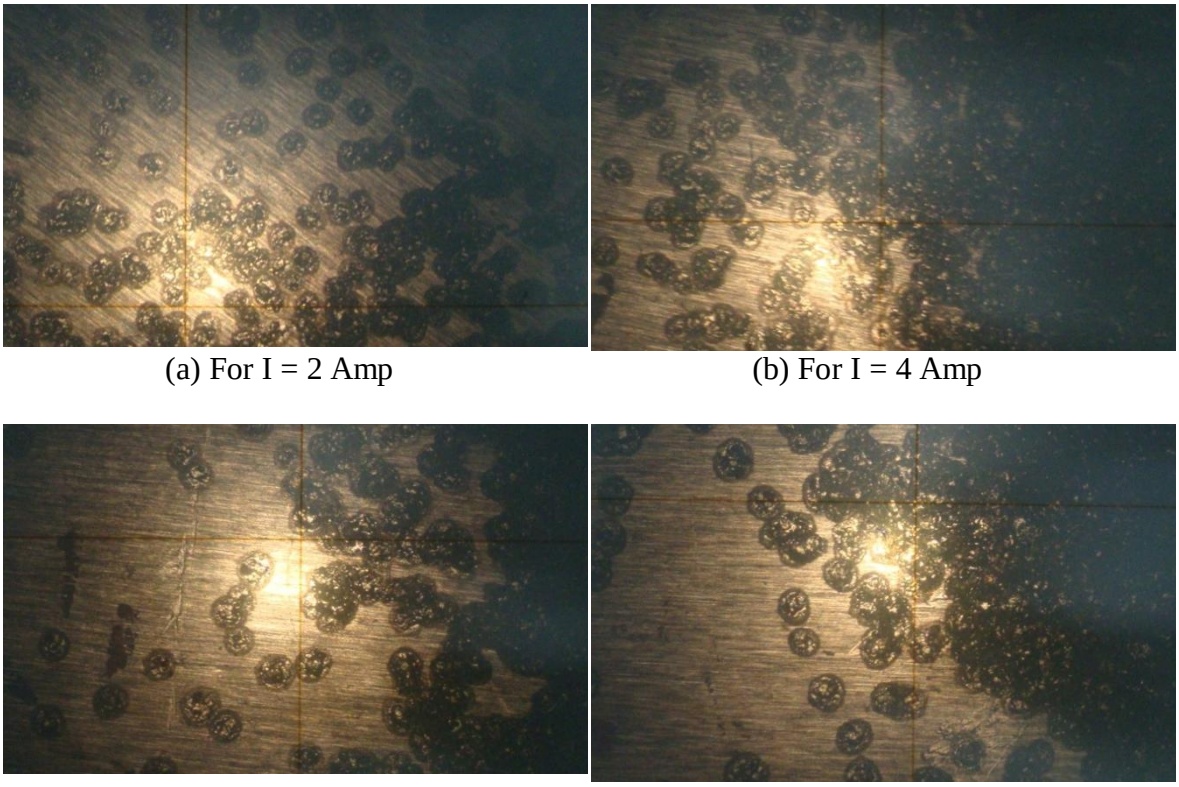

(a) For I = 2 Amp (b) For I = 4 Amp

(c) For I = 6 Amp (d)For I = 8 Amp

Figure 4.26 Craters formed during experiment using T_{on} 100 µs and T_{off} 50 µs at different current settings (a) 2 Amp, (b) 4 Amp, (c) 6 Amp and (d) 8 Amp

Figure 4.27 gives the results of volume removed in different experiment conditions.

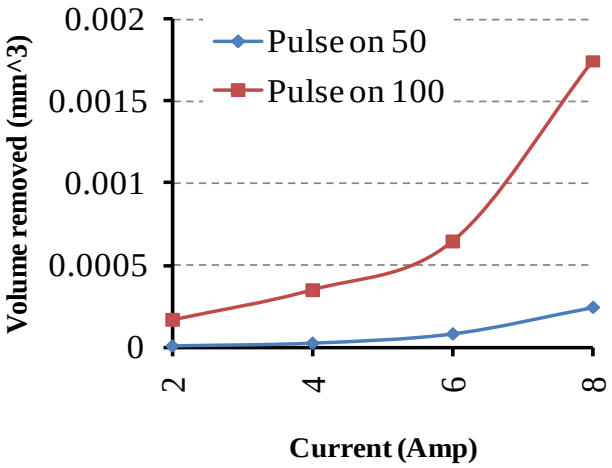

Figure 4.27: Volume removed during experiment

From Figure 4.27 it is predicted that volume removed increases by increasing discharge current and pulse on time. It is also observed that effect of pulse on time increases drastically while using discharge current more than 6 Amp.

4.2.2 Comparison of Experimental and Simulation results for volume removed

Validation of the simulation results of volume removed with the experimental one has been shown in Figure 4.28, 4.29 and 4.30. Figure 4.28 compares the results for pulse on 50 µs. From Figure 4.28 it is observed that experimental results of volume removed nearly match with the volume removed in simulation at C_w 0.2. So it is concluded that 20 % of total supplied heat goes into workpiece when 50 µs pulse on time was used.

Figure 4.29 shows comparison of simulation and experimental results for volume removed with pulse on time 100 µs. From Figure 4.29 it is observed that 25 % of the total supplied heat goes into workpiece using pulse on 100 µs. Figure 4.30 shows the trend of the experimental results of volume removed with simulated ones.

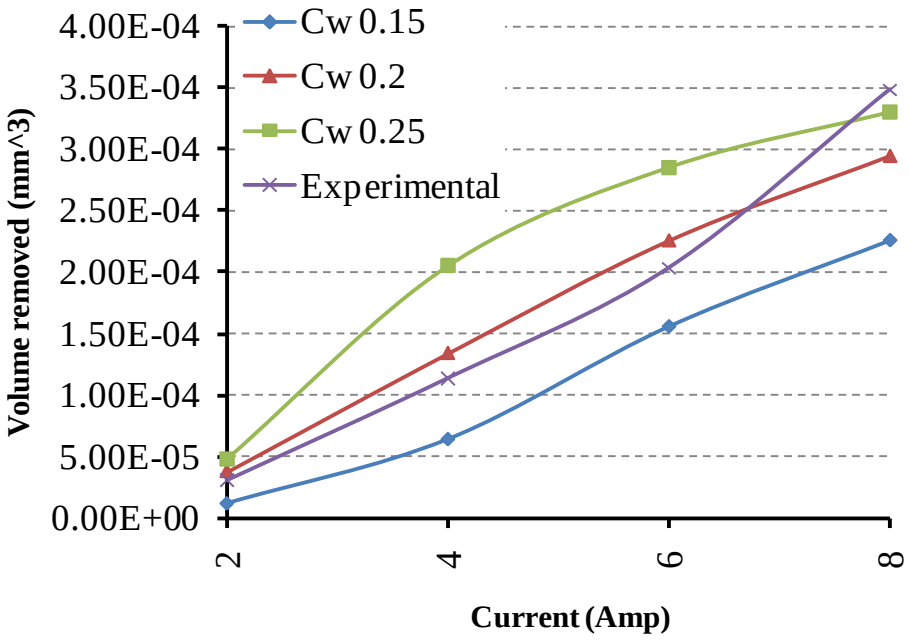

Figure 4.28: Comparison of simulation and experimental volume removed in mm^3 using T_{on} 50 µs

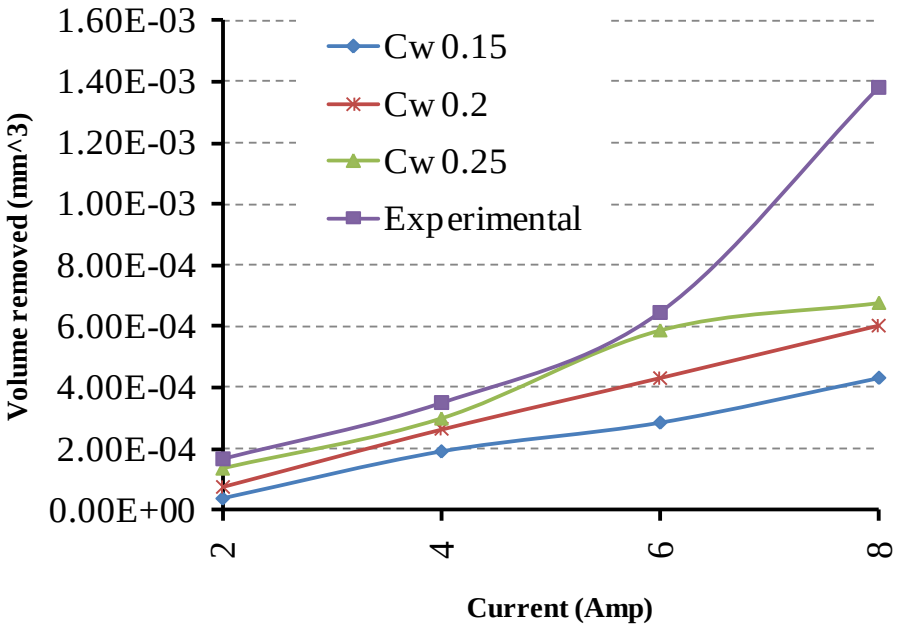

Figure 4.29: Comparison of simulation and experimental volume removed in mm^3 using T_{on} 100 µs

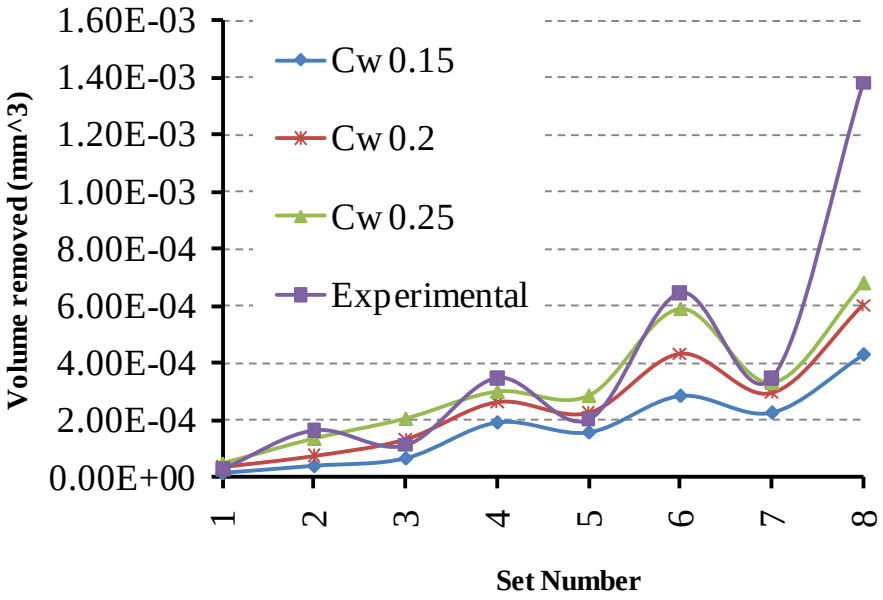

Figure 4.30: Comparison of volume removed between simulated and experimental at different current and pulse on time setting shown in table 3.6

4.2.3 Detailed Study of Craters

To study the shape and size of the crater in more details, snapshot of four different craters have been taken for each set of experiment with two magnifications of 100X and 200X using Lieca Microscope.

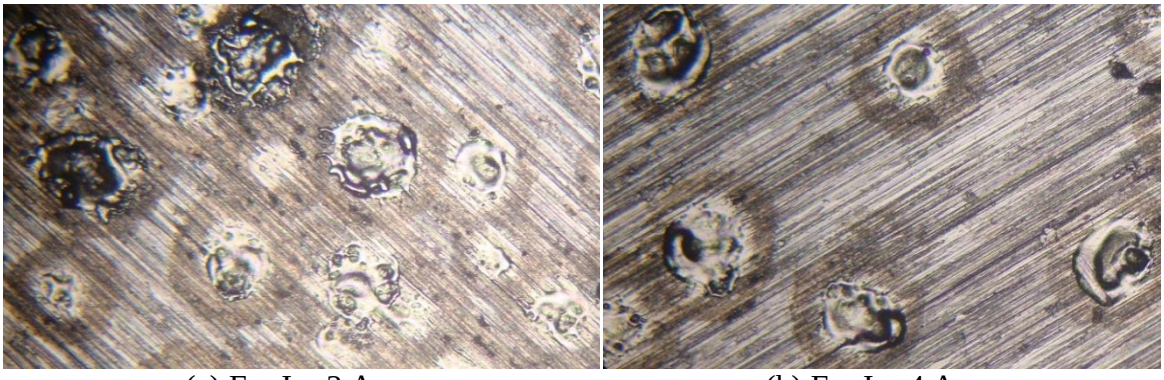

(a) For I = 2 Amp (b) For I = 4 Amp

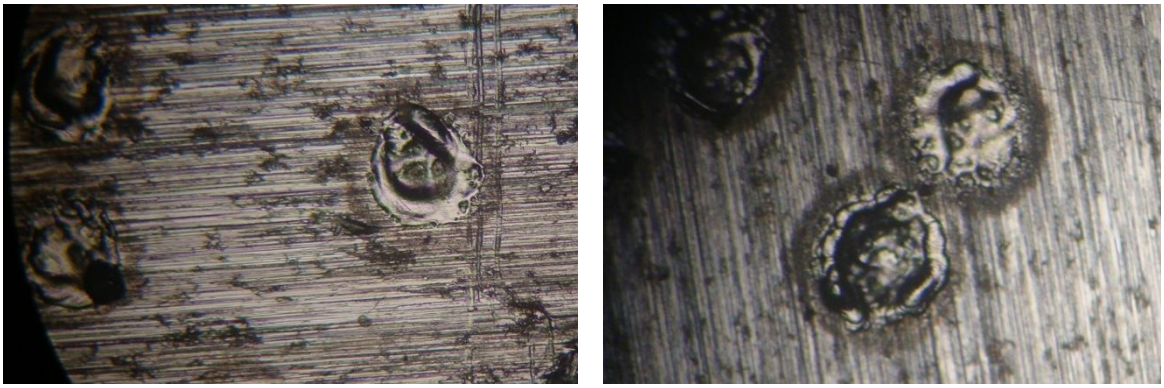

(c) For I= 6 Amp (d) For I = 8 Amp

Figure 4.31: craters formed during experiment with parameteres T_{on} 50 µs and T_{off} 50 µs

Here reported images of the craters in Figure 4.31 and 4.32 are having 100X magnification. Input parameters used in experiment shown in Figure 4.31 (a), (b), (c) and (d) are pulse on 50 µs, pulse off 50 µs and current of 2, 4, 6 and 8 Amp respectively for four different set of experiments. Studying Figure 4.31 (a) to (d) it is observed that size of the crater increases with increase in the current. It is also visible that effect on the diameter is larger compared to the depth of the crater. Hence crater is having shape as part of a sphere. Considerable amount of material resolidify and deposit on the crater itself during pulse off time. As the craters formed with higher value of currents are larger so the surface finish using higher level of currents will be less. Comparing Figure 4.31 (a), (b), (c) and (d) it is confirmed that surface finish of the machined surface decreases with increase in the discharge current. From the shape of the craters it is observed that effect of the electrostatic force acting on the spark region is also significant as splashed materials can be seen on the boundaries of the craters formed. Resolidified material can be seen especially on the boundary of the crater which have been removed to form the crater, but resolidified after they splash out due to the existence of the impulse force.

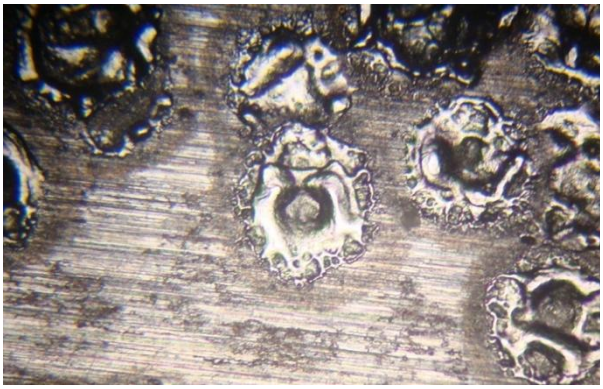

(a) For I = 2 Amp

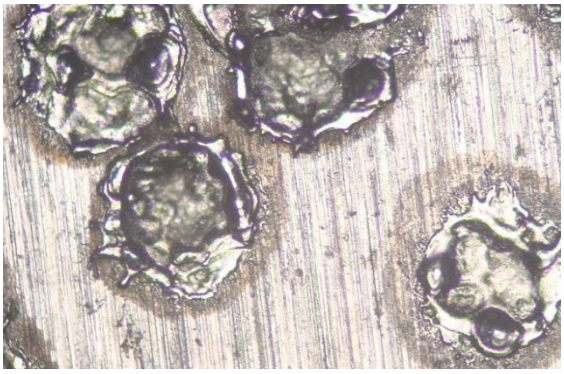

(b) For I = 4 Amp

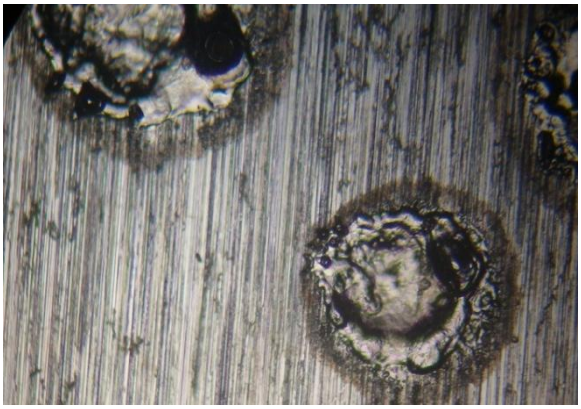

(c) For I= 6 Amp

(d) For I = 8 Amp

Figure 4.32: craters formed during experiment with parameteres T_{on} 100 µs and T_{off} 50 µs

Input parameters used in experiment shown in Figure 4.32 (a), (b), (c) and (d) are pulse on 100 µs, pulse off 50 µs and current = 2, 4, 6 and 8 Amp respectively for four different set of experiments. Comparing Figure 4.31 and 4.32 it is inferred that size of the crater increases significantly with increase in the pulse on time for the same input discharge currents. From the Figure 4.32 (a) to (d) it is visible that black circle shown near the periphery of the crater is the heat affected zone. No effect of the heat is visible on the surface beyond this zone. Again Figure 4.32 (a) shows that considerable amount of material resolidify and deposit on the crater surface during PMEDM.

4.2.4 Microstructure of the Machined Surface

To assess microstructure of the machined surface two experimental set have been performed with pulse off 50 µs, discharge current 2, 6 Amp, pulse on 100, 50 µs respectively for two different experiments. Machining time is 10 minutes for each experimental set. Observations are taken on Lieca Microscope with two different magnifications i.e. 100X, 200X and 500X. Figure 4.33 (a) and (b); showing microstructure of the machined work material are captured at magnifications 100X and

200X respectively. Input parameters for the experiment shown in Figure 4.33 (a) and (b) are current = 2 Amp, pulse on 100 µs, pulse off 50 µs. large cracks can be seen on the work material surface in Figure 4.33 (b) which validate the high stresses and cooling rate predicted into the work material during simulation part.

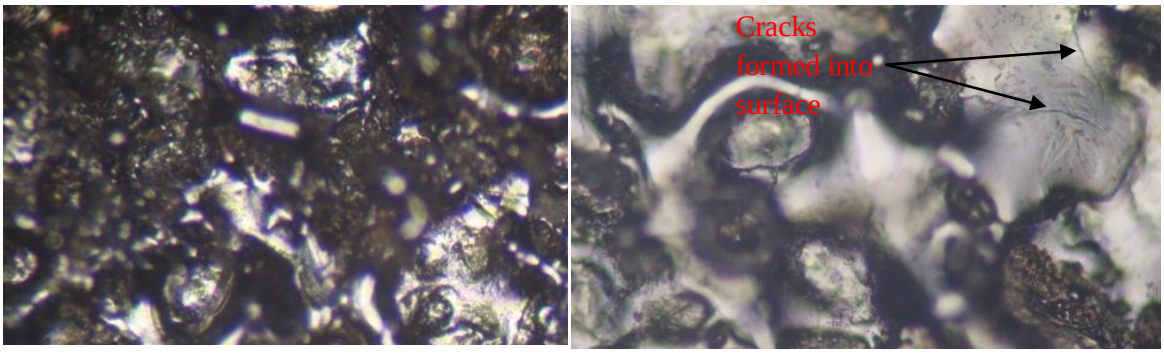

(a) view at 100X magnification (b) view at 200X magnification

Figure 4.33: machined surface using I = 2 Amp, T_{on} 100 µs and T_{off} 50 µs

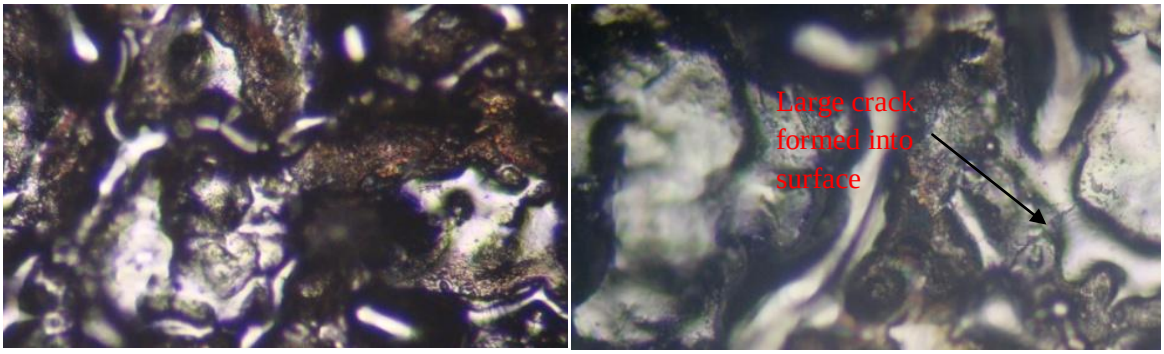

(a) view at 100X (b) view at 200X

Figure 4.34: machined surface using I = 6 Amp, T_{on} 50 µs and T_{off} 50 µs

Discharge current 6 Amp, pulse on 50 µs and pulse off 50 µs are set during experiment represented in Figure 4.34 (a) and 4.34 (b). Comparing Figure 4.33 and Figure 4.34 it is observed that there is less difference in depth of the irregular valleys formed on the surface during pulse on time 100 and 50 µs than the area covered by it. Again, a large crack shown in the Figure 4.34 (b) validates high stresses and cooling rate predicted into the work material during simulation part. Further, as it was observed from the cooling rate curves that cooling rate is more with lower pulse off duration, the amount of cooling and thereby subsequent formation of white layers on the machined surface is more when 50 µs pulse off is used as compared to case of 100 µs pulse off time (comparing Figure 4.33 (b) and 4.34 (b)).

CHAPTER 5
CONCLUSION AND FUTURE SCOPE

5.1 CONCLUSION

Present work is done to study the thermal aspects of Powder Mixed EDM process. ANSYS Workbench 12.0 transient thermal analysis module has been used to simulate temperature distribution into work material due to incident heat on the workpiece following a Gaussian distribution. Different sets of simulations are done by varying process parameters like discharge current, supplied voltage and C_w (percentage of heat being transferred to workpiece) at different levels. To investigate the stresses induced into the work material coupled thermal structural analysis was done. Also cooling rate of the work material has been estimated for different pulse durations. For the validation experiments are conducted on H11 material for different current and pulse on settings.

Based on the results of the present work, following conclusions were drawn:

1. **Temperature Distribution:** It is observed that temperature distribution into work material is maximum at the center of the region under spark and decrease in radial direction following Gaussian distribution. Peak temperature is found to increase with increase in discharge current, pulse on time and C_w factor. From the temperature distribution in the work material it is visible that diameter of the crater is much larger than depth which predict that craters formed into work materials are shallow and have shape as a part of a sphere. It is also determined that peak temperature is more affected by pulse on durations compared to C_w.

2. **Volume Removed:** Volume removed by the single crater increases with increase in pulse on time resulting increased MRR. Diameter and depth of the crater produced during pulse on 100 µs pulse on time is significantly larger than produced during pulse on 50 µs. Increasing current and C_w factor increase volume removed resulting in high material removal rate (MRR). Due to large size of craters formed on the surface, surface finish will be less for high pulse on timings. It is predicted that volume removed during pulse on time 100 µs is nearly double than volume removed during pulse on 50 µs. Behavior of work material has been studied at different temperature zones i.e. unaffected zone, heat affected zone, melting zone and evaporation zone. It is

clarified that at high discharge current evaporation proportionate to melting is quite large which will increase material removal rate and material flushing efficiency.

3. **Cooling Rate:** Cooling rate is higher for the short pulse off timings. It is also observed that increasing discharge current and C_w factor also increase the cooling rate. For higher cooling rates surface quality will be poor and material will be more prone to crack generation. Large cooling rate will also affect the material in the melting zone to resolidify and higher white layer formation on the machined surface as observed from the microstructure analysis.

4. **Stresses Induced in Work Material:** Due to the elevated temperatures in PMEDM; material melts or evaporates and flushed out in the form of debris by the dielectric flushing. At the same time material below the spark region tries to expand because of high temperatures but restricted by the surrounding material. Because of this sufficient amount of stresses setup there in remaining work material near to crater surface which may result in generation of the cracks in work material. Maximum stresses setup into work material during simulation using parameters pulse on 75 µs, K_p 2.4, V_d 35 Volt are 6911 MPa and 4841 MP respectively for current 6 and 8 Amp, which are quite larger than the ultimate tensile strength of the work material. So it is predicted that chances of crack formation are there on the workpiece near the machined surface. It is observed that increasing current increases the stress values setup into the work material. Also for higher values of C_w stresses are high. High stresses near to crater surface leads to tendency of the material to fail. So it is concluded that for higher values of current and C_w strength of the material will be less near to the machined surface of the work material. It is also predicted that with increase in pulse on time stresses setup into the work material will increase and material will more prone to failure near the surface due to low strength caused by high stresses setup into the material near surface.

5. **Experimental Validation:** To validate the simulation results of volume removed, cooling rate and induced stresses experiments have been performed with varying process parameters like discharge current, pulse on time. For pulse on 50 µs experimental volume removed nearly match with the volume removed in simulation at C_w 0.2. So it is concluded that 20 % of total supplied heat goes into workpiece. At the

same time it is also predicted that for pulse on duration 100 µs 25 % of total supplied heat goes into workpiece i.e. C_w is 0.25.

From the microscopic observation of the craters, it was found that craters are mostly part of sphere and the sized increases with increase in current and pulse on time. Also some of the material after getting removed to form the crater re-solidified around the periphery of the formed crater. Microstructure of the machined surface showed formation of cracks due to higher cooling rate and stresses.

5.2 FUTURE SCOPE

1) Further analysis can be done using varying spark radius for different current and pulse on time settings.

2) Effect of electrostatic forces or the impulse force can be included in further studies for simulation of PMEDM process.

3) In present work meshing of the region under spark is not emphasized as much. To increase number of nodes in the spark region and obtain more precise solution it is required to mesh the region under spark with a very small size of elements compared to the region beyond the spark which is not affected too much by the heat flux.

4) In actual machining during pulse off period crater moves to another location and after a certain period of time it again comes near to previous location overlapping previous craters formed. So overlapping of craters need to be simulated and a logic is required to develop which will explain that after how much time spark will come back near to previous location for a defined size of electrode and surface roughness of electrode and work material.

5) In PMEDM process continuous pulse on and pulse off occurs during all of the machining time. Heat flux incident on the work material is intermittent all the time. At the same time cooling of the work material takes place. Fatigue analysis of the work material during PMEDM process to estimate the life of the machined surface.

REFERENCES

[1] Izquierdo B., Sanchez J.A., Plaza S., Pombo I., Ortega N., (2009) "A numerical model of the EDM process considering the effect of multiple discharges", *International Journal of Machine Tools & Manufacture* Vol. 49, pp 220–229

[2] McGeough J.A. (1988), "Advanced Methods of Machining", Chapman and Hall, USA, ISBN 0-412-31970-5.

[3] Mishra P.K. (2005), "Nonconventional Machining", Narosa Publishing house, New Delhi, India, ISBN 81-7319-192-19.

[4] Jain V. K. (2004) "Advanced Machining Processes", Allied Publishers, New Delhi, India, ISBN 81-7764-294-4.

[5] Schumacher B.M. (2004), "After 60 years of EDM the discharge process remains still disputed", *Journal of Material Processing Technology*, Vol. 149, pp 376-381.

[6] Kansal H.K., Singh S., Kumar P., (2008) "Numerical simulation of powder mixed electric discharge machining (PMEDM) using finite element method", *Mathematical and Computer Modelling* Vol. 47, pp 1217–1237

[7] Marafona J., Chousal J.A.G., (2006) "A finite element model of EDM based on the Joule effect", *International Journal of Machine Tools & Manufacture* Vol. 46, pp 595–602

[8] Das S., Klotz M., Klocke F., (2003) "EDM simulation: finite element-based calculation of deformation, microstructure and residual stresses", *Journal of Materials Processing Technology* Vol. 142, pp 434–451

[9] Joshi S.N., Pande S.S., (2010) "Thermo-physical modeling of die-sinking EDM process", *Journal of Manufacturing Processes* Vol. 12, pp 45-56

[10] Singh A., Ghosh A., (1999) "A thermo-electric model of material removal during electric discharge machining", *International Journal of Machine Tools & Manufacture* Vol. 39, pp 669–682

[11] Ekmekci B., Elkoca O., Tekkaya A., Erden A., "Residualstress state and hardness depth in electric discharge machining: de-ionized water as dielectric liquid", *Machine Science and Technology*, Vol. 9, pp 39–61

[12] Yadav V., Jain V. K., Dixit P. M., (2002) "Thermal stresses due to electrical discharge machining", *International Journal of Machine Tools & Manufacture* Vol. 42, pp 877–888

[13] Schulze H.P., Herms R., Juhr H., Schaetzing W., Wollenberg G., (2004) "Comparison of measured and simulated crater morphology for EDM", *Journal of Materials Processing Technology* Vol. 149, pp 316–322

[14] Panda D.K., Bhoi R.K., "Analysis of spark eroded crater formed under growing plasma channel in electro-discharge machining", *Machining Science and Technology*, Vol. 9, pp 239–261

[15] Ekmekci B., Tekkaya A., Erden A., (2006)" A semi-empirical approach for residual stresses in electric discharge machining (EDM)", *International Journal of Machine Tools & Manufacture* Vol. 46, pp 858–868

[16] Sanchez J. A., Izquierdo B., Ortega N., Pombo I., Plaza S. and Cabanes I.(2009) "Computer simulation of performance of electrical discharge machining operations", *International Journal of Computer Integrated Manufacturing*, 22: 8, 799 — 811

[17] Salah N.B., Ghanem F., Atig K.B., (2006) "Numerical study of thermal aspects of electric discharge machining process", *International Journal of Machine Tools & Manufacture* Vol. 46, pp 908–911

[18] Panda D. K., (2008) "Study of thermal stresses induced surface damage under growing plasma channel in electro-discharge machining", *Journal of Materials Processing Technology* Vol. 202, pp 86–95

[19] Izquierdo B., Sanchez J.A., Plaza S., Pombo I., Ortega N., (2009) "A numerical model of the EDM process considering the effect of multiple discharges", *International Journal of Machine Tools & Manufacture* Vol. 49, pp 220–229

[20] Philip A., Xiaolin C., (2007) "Process simulation of micro electro-discharge machining on molybdenum", *Journal of Materials Processing Technology* Vol. 186, pp 346–355

[21] Tan P. C., Yeo S.H., (2008) "Modelling of overlapping craters in micro-electrical discharge machining", *J. Phys. D: Appl. Phys.* Vol. 41, Page No. 205302 (12pp)

[22] Kumar S., Singh R., Singh T.P., Sethi B.L., "Comparison of material transfer in electrical discharge machining of AISI H13 die steel", *DOI: 10.1243/09544062JMES1227* (2008).

[23] Soni J.S., Chakraverti G., (1996) "Experimental investigation on migration of material during EDM of die steel (T215 Cr12)",*Journal of Material Processing and Technology* Vol. 56, pp 439-451.

[24] Soni J.S., (1994) "Microanalysis of debris formed during rotary EDM of titanium alloy (Ti 6Al 4V) and die steel (T 215 Cr12)", *Wear* Vol. 177, pp 71-79.

[25] Nowicki B., Dmowska A., Podolak-Lejtas A., (2010) "A new method of investigating crater and flash made by individual discharge using scanning profilometers", *Wear* Vol. 270 (3-4), pp 121-126

[26] Tamura T., Kobayashi Y., (2004) "Measurement of impulsive forces and crater formation in impulse discharge", *Journal of Materials Processing Technology* Vol. 149, pp 212–216

[27] Singh Gurpreet, (2010) "Experimentation for improvement in surface properties and process optimization of die steels by using powder mixed dielectric in EDM process", *ME Thesis, Thapar University, Patiala.*

[28] Singh Gurmail, (2010) "Investigations on Improvement of Material Properties and parametric optimization of MRR, TWR and Roughness using Powder Mixed Dielectric in EDM Process", *ME Dissertation, submitted to Thapar University Patiala*.

[29] A. Bhattacharya, A. Batish, G. Singh, (2011) "Optimization of Powder Mixed Electric Discharge Machining using Dummy Treated Experimental Design with Analytic Hierarchy Process", Proc. Instn. Mech. Engrs, Part B: J. Engg. Manuf., accepted manuscript.

[30] Ajay Batish, Anirban Bhattacharya, V. K. Singla, Gurmail Singh, (2011) "Study of Material Transfer Mechanism in Die Steels using Powder Mixed EDM", *Materials and Manufacturing Processes*, accepted manuscript.

[31] DiBitonto D.D., Eubank P.T., Patel M.R., Barrufet M.A., (1989) " Theoretical models of electrical discharge machining process- I. A simple cathode erosion model", *Journal of Applied Physics* Vol. 66 (9), pp 4095-4103.

[32] Patel M.R., Barrufet A., Eubank P.T., DiBitonto D.D., (1989) "Theoretical models of electrical discharge machining process- II: The anode erosion model", *Journal of Applied Physics* Vol. 66 (9), pp 4104-4111.

[33] P. Shankar, V.K. Jain, T. Sundarajan, (1997) "Analysis of spark profiles during EDM process", *Machining Science Technology* Vol.1 (2), pp 195–217.

[34] Jilani S.T., Pandey P.C., (1982) "Analysis and modeling of EDM parameters", *Precision Engineering* Vol. 4 (4), pp 215-221.

[35] Erden A., Kaftanoglu B., (1980) " Heat transfer modeling of electric discharge machining", *in: 21st MTDR Coference, Swansea*, pp. 351-358.

[36] Marty C.C., (1977) "Investigations of surface temperature in electro discharge machining", *Transactions of ASME, Journal of Engineering for Industry* 682-684.

[37] Snoyes R., Van Dijck F., (1971) “Investigations of EDM operations by means of thermo mathematical models”, *Annals of CIRP* 20 (1) 35.